POLITECNICO DI TORINO

Master of Science in Mechanical Engineering

Master's Thesis

Simulating the Impact of Vortex Generators on the Catalytic Methanol Synthesis in a 2D Channel Using Computational Fluid Dynamics

Supervisors
Prof. Eliodoro Chiavazzo
Prof. Ville Vuorinen
D.Sc. Marko Korhonen

Candidate
Mohamed El Zein

A.Y. 2023-2024

Author Mohamed El Zein

Title of thesis Simulating the Impact of Vortex Generators on the Catalytic Methanol Synthesis in a 2D Channel Using Computational Fluid Dynamics

Programme Master of Science in Mechanical Engineering

Thesis supervisors Prof. Ville Vuorinen, Prof. Eliodoro Chiavazzo

Thesis advisor D.Sc. Marko Korhonen

Date 31/07/2023 **Number of pages** 77 **Language** English

Abstract

Catalytic methanol synthesis in a 2D rectangular microchannel reactor is modelled in OpenFOAM. This type of reactors offers several advantages from the fluid-dynamic viewpoint, such as enhanced mass and heat transfer, in addition to high single-pass efficiencies. However, the main drawback of these reactors is their limited methanol throughput as compared to their conventional fixed-bed counterparts. Therefore, the goal of this thesis is to analyse the impact of different thermo-fluid dynamic settings on methanol production, seeking an optimal methanol yield. In the present analysis, only surface reactions are accounted for. They are implemented over the catalytic walls of the channel according to the Langmuir-Hinshelwood-Hougen-Watson (LHHW) kinetics. Moreover, the diffusion phenomena between the involved chemical species in the reactor are addressed based on Fick's law, under the assumption of a unity Lewis number. Accordingly, the synthesis simulations are conducted. The reactor achieves its best performance when the temperature at the catalytic walls ranges between 210-220°C. As the temperature increases further, the methanol yield continues to diminish. Concerning the flow characteristics, the reaction residence time proves to be the dictating factor, as greater volumetric concentrations of methanol yield result from the reduction in the bulk Reynolds number. Furthermore, elongating the zone at which the catalyst coating is applied enhances the methanol yield. Finally, vortex generators are introduced in the channel and the effect of transport-mediated mixing is investigated. At each individual Reynolds number, inducing flow mixing led to achieving greater yields. However, even at such flow characteristics, the reactor records its highest yielded mass fractions at the lowest simulated bulk flow velocities (highest reaction residence time).

Table of contents

Preface and acknowledgements

I would like to express my sincere gratitude to my esteemed thesis supervisors, Profs. Ville Vuorinen and Eliodoro Chiavazzo, and advisor, D.Sc. Marko Korhonen, for their invaluable guidance, unwavering support and expert mentorship throughout the course of my master's thesis. Their profound knowledge, encouragement and constructive feedback have been instrumental in shaping the direction and quality of this research. I am truly grateful for their dedication and commitment to my academic and professional growth. Their mentorship has been a source of inspiration and I am fortunate to have had the opportunity to work under their guidance.

Moreover, I am deeply grateful to my family and close friends for their consistent support and encouragement throughout my academic journey. Their belief in me has been a constant motivation and I am indebted to them for their love, guidance and understanding.

31/07/2023 – Mohamed El Zein

Symbols and abbreviations

Physical quantities

Re	Reynolds number
ρ	density
t	time
$\boldsymbol{u}$	velocity field
p	pressure field
μ	dynamic viscosity
h	enthalpy
λ	thermal conductivity
c_p	specific heat capacity at constant pressure
$\dot{\omega}_h$	heat release rate
Y	mass fraction
D	diffusion coefficient
$\dot{\omega}_k$	reaction rate
MW	molecular weight
A	geometrical area
α	coefficient of stoichiometry
r	reaction rate
V	geometrical volume
Δh_f^0	formation enthalpy
m	mass
X	molar fraction
f	fugacity
Le	Lewis number
Φ_f	flux
n	number of moles
ν	kinematic viscosity
$\dot{m}$	mass flow rate

Chemical symbols

CH_3OH	Methanol
CO_2	Carbon dioxide
H_2	Hydrogen
CO	Carbon monoxide
H_2O	Water

Mathematical operators

$\frac{\partial}{\partial t}$	partial derivative with respect to variable t
$\nabla .$	Divergence
∇	Gradient
Σi	Sum over index i
I	Identity tensor

Abbreviations

GHG	Greenhouse gases
RES	Renewable energy systems
PTF	Power-to-fuel
CFD	Computational Fluid Dynamics
VG	Vortex generator
NS	Navier-Stokes
RWGS	Reverse Water-Gas Shift
LHHW	Langmuir-Hinshelwood-Hougen-Watson
FVM	Finite Volume Method
OpenFOAM	Open Source Field Operation and Manipulation
SIMPLE	semi-implicit method for pressure-linked equations
PISO	pressure-implicit split-operator
BC	Boundary condition

1 Introduction

The emission of greenhouse gases (GHGs) has been the most concerning environmental dilemma since the beginning of the 21st century. It is the driving factor towards global warming. The concentration of carbon dioxide (CO_2) in the atmosphere nowadays has massively risen as compared to the days of the pre-industrial era [1]. This is mainly attributed to the excessive burning of fossil fuels in transportation and power production applications [2]. Fossil fuels are still the primary resources for meeting the global energy demand; they almost contribute to 80% of the world's energy consumption [3]. At such profound energy consumption rates, these traditional, non-renewable resources will most likely get depleted in the near future due to their relatively slow replenishment [4, 5]. It is also inferred that the need for energy will only get higher with time [6]. Therefore, this rapid growth in the global energy demand and the detrimental emissions resulting from the combustion of fossil fuels have driven countries to impose strict environmental regulations to try and limit the GHG emissions [7] and seek for alternative renewable, eco-friendly resources and low-carbon footprint power production methods.

Renewable energy systems (RES), based on solar radiation, wind and hydro-power, are normally coupled with traditional power plants in order to ensure the energy demand fulfillment, at reduced emissions [8]. However, some notable challenges and limitations in the exploitation of the renewable energy resources for power production have risen over time. For instance, generating electric power from sunlight and wind energy is known for being highly intermittent and unpredictable. To elaborate further, the performances of such RES are dramatically dictated by the speed at which the wind is blowing and the intensity of solar radiation, which in turn, are relentlessly fluctuating in time [9]. Accordingly, slow wind speeds or cloudy weather conditions hinder the power outputs of such systems to a major extent. This causes some difficulties in the system (grid) balancing, which often translates into considerable economic losses [10]. Furthermore, at high demands, the inability to meet the energy requirements when the RES yields are low leads back to the use of traditional fossil-fuel burning methods to compensate for the power shortage. In addition to that, the periodic productivity of RES has proved to be quite detrimental to conventional power plants, especially in those combined plants where multiple production techniques are coupled. For instance, oscillations and deficiencies in RES outputs lead to suboptimal, low-efficiency operation of traditional power plants, in addition to recurring start-ups and shutdowns, which cause increased wear to the power plants' infrastructure [10].

Moreover, electricity storage from RES proves to be extremely challenging and to implement large-scale RES, optimizing this storage is vital [11, 12, 13]. Namely, in low-energy demand periods, having optimal energy storages significantly enhances the efficiency of RES, as a great amount of energy would be saved. This saved, stored energy can then be utilized during periods of high demand, more importantly, when electricity would be extremely expensive to produce [14]. As a result, considerable financial gains could potentially be attained from optimal energy storage. The above-mentioned reasons justify the significance of finding optimal solutions for overcoming the challenges and limitations of RES electricity storage.

In transportation terms, the electrification approach seems to be a very convenient, environment-friendly alternative that augments the transition towards carbon neutrality. Using electricity instead of fossil fuels as the driving power source greatly diminishes the concentration of CO_2 and other GHG emissions into the atmosphere

[15]. However, as of today, this technology still falls short in some particular fields, such as aerospace transport, heavy-load, massive vehicles (*e.g.* trucks), marine applications and long-haul trips, which typically require substantial amounts of energy [16, 17, 18]. Indeed, matching such energy demands with the current available battery technologies would not be feasible due to their limited volumetric energy densities [19], making electrification of extreme difficulty in such cases. Therefore, fossil fuels are still the number one option in these scenarios.

The previous discussion elaborates the low efficiency, complications and limitations involved in the storage of electricity generated using RES. It also tackles the inability of substituting fossil fuels by electricity in some of the most important transportation domains and applications. Thus, electric energy, in such cases, may have to be converted into other more useful low-carbon forms, which are easier to store and convey [20, 21]. Consequently, the so-called power-to-fuel (PTF) technology started gaining interest [15, 22]. The technology is concerned with transforming electric power produced by RES into synthetic fuels (also known as E-fuels or green fuels). Generally, these fuels are obtained through reactions between hydrogen and CO_2. In fact, hydrogen gas (H_2), being the key component for the formation of hydrogen-based low-emission fuels, is considered the core of this PTF methodology [23]. The traditional method used to produce hydrogen is steam reforming of methane. Therefore, the conventional, depletable natural gas is the main resource for hydrogen production [24]. However, in the PTF concept, hydrogen is produced by electrolysis of water, totally driven by renewable electricity, *i.e.* the process of separating water into hydrogen and oxygen is solely powered by green energy, which implies minimal GHG emissions into the atmosphere. Correspondingly, the term E-hydrogen comes into play.

Hence, hydrogen is considered as a green energy carrier and an eco-friendly fuel. It can be utilized in heating, transportation, energy production and some other noteworthy applications. It also plays a crucial role in the manufacturing of some fundamental chemical compounds, *e.g.* methanol and ammonia [25].

On the other hand, CO_2 is also attained in an ultimately environment-friendly way when adopting PTF techniques. It can directly be absorbed from the atmosphere or from different flue gas sites, which are ubiquitous in power plants, industries, factories and vehicle emissions, for instance [26]. Exploiting waste CO_2 as such remains classified as renewable as it does not feature additional release of CO_2 into the air. Other sustainable practices of generating CO_2 involves combustion of biomass and anaerobic digestion [27].

The storage of surplus electricity generated from RES in the form of green fuels (or chemicals) such as, hydrogen and methanol (CH_3OH), during periods of low demand, constitutes an exemplary storage solution, which is considerably more advantageous than direct electricity storage [22, 28]. Consequently, this serves as a decent solution to intermittency and grid balancing problems [29]. Hence, these green production methods of E-fuels greatly promote the mitigation of GHG emissions and foster the shift towards carbon neutrality.

One of the most important hydrogen-derived clean synthetic fuels is methanol (CH_3OH). In storage terms, methanol is preferred to hydrogen due to being liquid at standard temperature and pressure (STP), which makes its storage and transport safer and easier [30]. Also, as far as the chemical industry is concerned, methanol is considered as a crucial foundational element. It serves as a feedstock employed to produce chemicals like acetic acid, dimethyl ether, methyl tertbutyl ether (MTBE) and formaldehyde [31]. Moreover, methanol can be utilized in industrial boilers, transportation, sewage processing and generation of electricity. It can also be applied as a hydrogen carrier in fuel cells [32]. In the transportation field, methanol fuel possesses some very good combustion characteristics [33]. Thus, it can be used as an alternative fuel in internal combustion engine (ICE) vehicles or it could be blended with gasoline or diesel. Either way, adopting this high-octane fuel yields a great overall emission reduction [34]. This sustainable fuel is also gaining more traction in the shipping sector, *e.g.* in dual-fuel engines (Wärtsilä), particularly after the enforcement of the strict emission regulations [35, 36].

As it stands, fossil-based resources (natural gas, coal-based syngas) still represent the largest share in the methanol production industry [37]. However, in the aim of reducing harmful emissions, alternative carbon-neutral procedures, featuring the same chemical reactions and physical conditions as the non-renewable ones, can be adopted to produce green methanol. In fact, E-methanol is formed through a process named CO_2 hydrogenation, *i.e.* renewable hydrogen gas (H_2) and waste CO_2 are coupled in a catalytic reactor at a temperature ranging between 200°C and 300°C and a pressure between 50-100 bar in the presence of a catalyst, based on copper or zinc oxide. Moreover, the reaction of CO_2 with H_2 also leads to the formation of carbon monoxide (CO), which in turn, reacts with H_2 to produce CH_3OH [38]. This other reaction is referred to as CO hydrogenation. Compared to other chemicals, the production of methanol is said to be more efficient [39]. It is also starting to be viewed as a reasonable option from an economic standpoint [40].

Enhancing the rate at which methanol is produced requires reactors having optimal designs, allowing them to properly control and maintain ideal pressure and temperature media during the catalytic synthesis process [41]. Furthermore, to achieve decent yields, gases must be recirculated over several reactor passes [42]. The flow conditions inside the reactor greatly impact the heat transfer phenomena, in addition to the mass diffusion of the different species and their interaction with the catalyst material. This may significantly influence the outcomes of the reactions [43]. All of these aspects can be thoroughly investigated with the help of numerical modelling.

In an industrial context, the most common methanol reactor is currently the one having the fixed-bed configuration (Lurgi type). In fact, most of the research work has been carried out on reactors of such type. Usually, the 1D plug flow reactor model is applied. 1D models, as the one mentioned above, can be split into two categories: pseudo-homogeneous models and heterogeneous models [37]. The former assumes the whole system as a pseudo continuum, while the latter treats each of the fluid species and the solid region (reactor's walls) explicitly. Overall, Manenti *et al.* have deduced that the differences between the results obtained by both models are minimal in standard working conditions [37]. The majority of the studies have adopted steady-state and pseudo-homogenous models, neglecting any dynamic contributions. Extending the models from 1D to 2D has also been considered [44, 45]. By addressing the influence of different closures on the mass diffusion inside the reactor, Solsvik and Jakobsen have found out that the disparities are marginal [46]. Petera *et al.* have investigated the relation between catalyst size and formation of hot spots inside the reactor [45]. As per the findings of Arab *et al.*, at reduced space velocities, monolithic reactors and these traditional fixed-bed ones exhibit analogous performances, but the former overtakes at greater velocities [44].

On the other hand, Computational Fluid Dynamics (CFD), at an increased computational cost, offers a highly-accurate alternative technique for modelling methanol synthesis. In fact, coupling Navier-Stokes' equations with an appropriate chemical kinetic model permits 2D and 3D dynamic modelling of reacting flows. The two viable approaches for such cases are: the effective continuum approach, which is capable of simulating the entire length of a reactor, and the particle-resolved method, which provides a more rigorous analysis of the transport phenomena inside the reactor, but at smaller scales [47]. Although CFD simulations of reactive flows have evolved [48], their application in the field of methanol synthesis has been limited. Nevertheless, out of the few studies that have been conducted, the effect of the quality of the flow on the performance of a fixed-bed reactor has been analysed by Mirvakili *et al.* [49]. Moreover, Redondo *et al.* have compared different tube-cooled and tubular reactors [50]. It is also worth mentioning the research work accomplished by Izbassarov *et al.* [51], where methanol synthesis has been simulated in a catalytic fixed-bed reactor under both, isothermal and adiabatic conditions, at different pressures and temperatures, for different packing densities and bed configurations (random, inline, staggered) of the catalyst-coated tube banks. The findings of this study ensure that isothermal conditions are more favourable with respect to adiabatic ones. Additionally, staggered and random packings of the catalyst significantly enhance the interaction between the reactants and the catalyst. Hence, they substantially outperform the in-line configuration. The increase in the packing density also increases the methanol yield of the reactor. Moreover, the obtained methanol mass fraction increases at higher pressures inside the reactor, while it exhibits a non-monotonic trend with temperature.

In this thesis, the catalytic synthesis of methanol is studied in a 2D-channel, representative of a single channel in a microchannel reactor. In fact, microchannel reactors offer an exceptional single-pass efficiency and permit excellent thermal control due to their high surface area to volume ratio. This yields an optimal heat exchange within the reactor and reduces the risk of hot-spot formation that may lead to the sintering of the catalyst and failure of the synthesis [42]. Additionally, these reactors are characterized with rapid, efficient mass transfers [52]. However, the main caveat of adopting reactors as such is the small throughput compared to their traditional counterparts. The lack of studies carried out on microchannel reactors in the domain of methanol production does not permit validating the obtained outcomes against benchmark cases.

The goal is to utilize Computational Fluid Dynamics (CFD) for optimizing the methanol yield in a reactor segment comprised of a 2D channel. Reactions governing methanol synthesis take place at the walls, where a catalyst coating is applied. The influence of the channel's temperature conditions on the produced concentration of methanol is analyzed. Moreover, the synthesis is simulated at several Reynolds numbers (Re) in the laminar flow regime. Furthermore, the effect of extending the length over which the catalyst coating is applied is also addressed. Finally, the focus is shifted towards the impact of transport-mediated mixing. For this purpose, vortex generators (VGs) are installed in the channel. VGs are obstacles that generate vortices in the flow when a moving fluid impinges upon them [53]. They can be utilized to induce mixing and enhance heat transfer [54].

Hence, the objective is to comprehend the most dominant and influential factors affecting the catalytic synthesis of methanol. Determining the optimal thermo-fluid dynamic combination that maximizes the methanol yields of such microchannel reactors would, to the author’s best knowledge, provide a novel contribution so far lacking in the literature.

2 Research material and methods

This section presents the Navier-Stokes' (NS) equations that govern methanol synthesis, along with a concise explanation of the key terms involved. Subsequently, the modelled chemical reactions and their associated rate equations are discussed. Additionally, the software tools employed and the discretization schemes applied to the governing equations are introduced. Lastly, a comprehensive explanation is provided regarding the algorithm utilized to couple pressure and velocity fields.

2.1 Theory and governing equations

In a CFD context, methanol synthesis falls into the category of reacting flows. It is assumed that the present computational domain involves a low-Mach number, compressible flow. For analyzing the performance of a microchannel reactor in producing methanol, it is necessary to discretize the set of compressible NS-equations corresponding to reactive flows (Eqs. 1-4) [55].

$$\frac{\partial \rho}{\partial t} + \nabla.(\rho \boldsymbol{u}) = 0, \tag{1}$$

$$\frac{\partial \rho \boldsymbol{u}}{\partial t} + \nabla.(\rho \boldsymbol{u}\boldsymbol{u}) = -\nabla p + \nabla.\left[\mu(\nabla \boldsymbol{u} + \nabla \boldsymbol{u}^T) - \frac{2}{3}\mu\nabla.\boldsymbol{u}I\right], \tag{2}$$

$$\frac{\partial \rho h_t}{\partial t} + \nabla.(\rho \boldsymbol{u} h_t) = \frac{\partial p}{\partial t} + \nabla.\left(\frac{\lambda}{c_p}\nabla h_s\right) + \dot{\omega}_h, \tag{3}$$

$$\frac{\partial \rho Y_k}{\partial t} + \nabla.(\rho \boldsymbol{u} Y_k) = \nabla.(\rho D \nabla Y_k) + \dot{\omega}_k. \qquad k = 1, \dots, n_s \tag{4}$$

Eqs. (1-4) represent the continuity, momentum conservation, energy conservation and species' transport equation, respectively. In the present work, ρ is not computed iteratively. Instead, it is analytically determined using the ideal gas law.

Table 1. Summary of the symbols used in the governing equations

Symbol	Correspondence
ρ	density of the mixture of species
t	time
$\boldsymbol{u}$	velocity field
p	pressure field
μ	dynamic viscosity
I	identity tensor
h_t	total enthalpy
λ	thermal conductivity

c_p	specific heat capacity at constant pressure
h_s	sensible enthalpy
$\dot{\omega}_h$	heat release rate of the reaction
Y_k	mass fraction of species k
D	diffusion coefficient for all species
$\dot{\omega}_k$	reaction rate of species k
n_s	total number of species present in the reactor

The total and sensible enthalpies are correlated as $h_t = h_s + \frac{1}{2}|u^2|$. The reactions involved in the synthesis solely occur at the catalytic walls of the reactor, *i.e.* the sides at which the catalyst coating is applied. As a result, equations (5) and (6), describing the heat source and the rate of formation of species k, $\dot{\omega}_h$ and $\dot{\omega}_k$, respectively, are valid only at these regions. They can be expressed as

$$\dot{\omega}_h = \sum_{k=1}^{n_s} \Delta h_{f,k}^0 \dot{\omega}_k, \tag{5}$$

$$\dot{\omega}_k = \rho_{cat} MW_k \sum_{i=1}^{n_f} \sum_{j=1}^{n_r} \frac{A_i \alpha_{jk} r_{ij}}{V_i} . \tag{6}$$

Table 2. Correspondences of the symbols used in equations (5) and (6)

Symbol	**Correspondence**
ρ_{cat}	the density of the used catalyst
MW_k	molecular weight of species k
n_f	number of faces forming the catalytic wall
n_r	number of reactions
A_i	the area of face i of the catalytic wall
α_{jk}	coefficient of stoichiometry of species k
r_{ij}	rate of reaction j
V_i	the volume of cell i that is adjacent to face i
$\Delta h_{f,k}^0$	formation enthalpy of species k

The expression representing the density of the catalyst is $\rho_{cat} = \frac{m_{\text{cat}}}{A_{\text{geometric}}}$, where m_{cat} is the catalyst mass and $A_{geometric}$ is the geometric area of the reactor covered by the catalyst. In all the examined simulation cases, ρ_{cat} at the catalytic walls is maintained constant at 278.334 g/cm^3.

Generically, the diffusion velocities of species k (V_k) in the mixture are determined by solving the system of equations

$$\nabla X_p = \sum_{k=1}^{N} \frac{X_p X_k}{D_{pk}} (V_k - V_p) + (Y_p - X_p) \frac{\nabla P}{P} + \frac{\rho}{p} \sum_{k=1}^{N} Y_p Y_k (f_p - f_k) \quad \text{for} \quad p = 1, N \tag{7}$$

where $D_{kp}=D_{pk}$ is the binary mass diffusion coefficient of species k into species p, X represents the molar fraction of the particular species and f is the fugacity [Pa]. Note that mass diffusion driven by temperature differences, *i.e.* the Soret effect, is neglected. However, computing such a system for unsteady flows is demanding and involves a significant computational cost. In this regard, the Fick's law simplification is commonly implemented in the majority of the codes. This implies that the diffusion velocity ($V_{k,i}$) is calculated from the concentration gradient and the diffusion coefficient as

$$V_{k,i}Y_k = -D_k \frac{\partial Y_k}{\partial x_i} \,. \tag{8}$$

Furthermore, another important parameter used to describe the diffusion phenomena is the Lewis number of species k (Le_k). In a mixture, Le_k is a local parameter used to compare the rate of heat diffusion to that of the molecular diffusion of species. It is defined as

$$Le_k = \frac{\lambda}{\rho c_p D_k} = \frac{D_{th}}{D_k} \,, \tag{9}$$

where $D_{th} = \frac{\lambda}{\rho c_p}$ is the coefficient of heat diffusivity. Under the assumption of unity Lewis number, *i.e.* $Le_k=1$, the diffusion coefficient of species k (D_k) would be the same for all the mixture's species and can be represented in a unified way as $D = D_{th} = \frac{\lambda}{\rho c_p}$ [56]. In the literature, this assumption is ubiquitous in the context of reactive flows [57, 58, 59]. Accordingly, the modelling of the diffusion phenomena in the present thesis is based on the integration between Fick's law and $Le_k=1$.

2.2 Chemical aspects

Methanol (CH_3OH) can originate from both, carbon dioxide (CO_2) and carbon monoxide (CO) in the presence of a catalyst composed of Cu/Zn/Al/Zr. In the present study, CH_3OH is produced by the hydrogenation of CO and CO_2 in a 2D channel at an isobaric condition of P=5MPa. This pressure setting is adopted for all simulations. The catalytic synthesis of methanol will be analysed under stoichiometric conditions only. The three main chemical reactions

(A) $CO + 2H_2 \rightleftharpoons CH_3OH$, $\Delta H_{298K} = -90.2$ kJ/mol (10)

(B) $CO_2 + 3H_2 \rightleftharpoons CH_3OH + H_2O$, $\Delta H_{298K} = -48.8$ kJ/mol (11)

(C) $CO_2 + H_2 \rightleftharpoons CO + H_2O$, $\Delta H_{298K} = +41.3$ kJ/mol (12)

are modelled at the catalytic walls of the channel [51]. Reactions (A), (B) and (C) are known as CO hydrogenation, CO_2 hydrogenation and Reverse Water-Gas Shift (RWGS) reactions, respectively. In the present analysis, only surface reactions are taken into account. Correspondingly, reactions occurring between the fluid particles themselves are neglected. Moreover, catalyst deactivation and sintering have not been modelled. Concerning the diffusion of reactants into the catalyst, it is assumed to be instantaneous. No permeation of the reactants into the catalyst or any other delays are considered. Hence, once the reactive species come into contact with the catalytic walls, the reactions start. Furthermore, by-products formed in relatively low concentrations, *e.g.* dimethyl ether, have been omitted from the analysis [60].

However, coupling only the aforementioned reactions with the NS-equations (1-4) is insufficient. The reactions' rate equations must also be described for this purpose. As per the findings of Kiss *et. al* [61], the rate expression can be formulated as

$$r = \frac{AB}{C}, \tag{13}$$

$$A = aT^n \, exp\left(-\frac{E_a}{RT}\right), \tag{14}$$

$$B = B_1 \, (\prod f_i^{b_i}) - B_2(\prod f_j^{b^j}) \;, \tag{15}$$

$$C = \left(C_i \left[\prod f_j^{c_j}\right]\right)^m, \tag{16}$$

where A is the kinetic term, B is the driving force and C is the adoption term.

Using the chemical kinetic model based on Langmuir-Hinshelwood-Hougen-Watson (LHHW) kinetics, the rate equations corresponding to reactions (A), (B) and (C) are provided as [55]

$$r_A = \frac{k_1 K_{\mathrm{CO}} \left[f_{\mathrm{CO}} f_{\mathrm{H_2}}^{1.5} - \frac{f_{\mathrm{CH_3OH}}}{(f_{\mathrm{H_2}}^{0.5} K_{eq_1})} \right]}{\left(1 + K_{\mathrm{CO}} f_{\mathrm{CO}} + K_{\mathrm{CO_2}} f_{\mathrm{CO_2}}\right) \left[f_{\mathrm{H_2}}^{0.5} + \left(\frac{K_{\mathrm{H_2O}}}{K_{\mathrm{H_2}}^{0.5}} \right) f_{\mathrm{H_2O}} \right]}, \tag{17}$$

$$r_B = \frac{k_2 K_{\mathrm{CO_2}} \left[f_{\mathrm{CO_2}} f_{\mathrm{H_2}}^{1.5} - \frac{f_{\mathrm{CH_3OH}} f_{\mathrm{H_2O}}}{f_{\mathrm{H_2}}^{1.5} K_{eq_2}} \right]}{\left(1 + K_{\mathrm{CO}} f_{\mathrm{CO}} + K_{\mathrm{CO_2}} f_{\mathrm{CO_2}}\right) \left[f_{\mathrm{H_2}}^{0.5} + \left(\frac{K_{\mathrm{H_2O}}}{K_{\mathrm{H_2}}^{0.5}} \right) f_{\mathrm{H_2O}} \right]}, \tag{18}$$

$$r_c = \frac{k_3 K_{\mathrm{CO_2}} \left[f_{\mathrm{CO_2}} f_{\mathrm{H_2}} - \frac{f_{\mathrm{H_2O}} f_{\mathrm{CO}}}{K_{eq_3}} \right]}{\left(1 + K_{\mathrm{CO}} f_{\mathrm{CO}} + K_{\mathrm{CO_2}} f_{\mathrm{CO_2}}\right) \left[f_{\mathrm{H_2}}^{0.5} + \left(\frac{K_{\mathrm{H_2O}}}{K_{\mathrm{H_2}}^{0.5}} \right) f_{\mathrm{H_2O}} \right]}, \tag{19}$$

where r represents the rate [mol/(g_{cat} s)] of the specified reaction. These coefficients have the same form as Eq. (14), particularly when n=0. Assuming that the gaseous species involved in the synthesis belong to the category of ideal gases, fugacities are replaced with partial pressures. Based on the work of Lim *et al.* [62] and An *et al.* [63], the driving factors and chemical equilibrium constants corresponding to reactions (A), (B) and (C) are reported in Table 3.

Table 3. The used constants for reactions (A), (B) and (C).

Coefficient	Expression	Unit
k_1	$4.0638 \times 10^{-6}\, e^{-11695/RT}$	$kmol/kg_{cat}.s.Pa$
k_2	$1.5188 \times 10^{-33}\, e^{-266010/RT}$	$kmol/kg_{cat}.s.Pa$
k_3	$9.0421 \times 10^{8}\, e^{-112860/RT}$	$kmol/kg_{cat}.s.Pa^{0.5}$
K_{CO}	$8.3965 \times 10^{-11}\, e^{118270/RT}$	Pa^{-1}
K_{CO_2}	$1.7214 \times 10^{-10}\, e^{81287/RT}$	Pa^{-1}
K_{CO}/K_{eq1}	$3.5408 \times 10^{12}\, e^{19832/RT}$	Pa
K_{CO_2}/K_{eq2}	$2.5813 \times 10^{10}\, e^{26788/RT}$	Pa
K_{CO_2}/K_{eq3}	$6.1221 \times 10^{-13}\, e^{125226/RT}$	Pa^{-1}
$K_{H_2O}/K_{H_2}{}^{0.5}$	$4.3676 \times 10^{-12}\, e^{115080/RT}$	$Pa^{-0.5}$

2.3 Discretization schemes and software tools

In the present thesis, the schemes that have been adopted for spatial and temporal discretization are the standard in Direct Numerical Simulations (DNS), in which no explicit turbulence modelling is performed. First, the Euler implicit scheme has been selected for discretizing the time-dependent derivative terms. It is a first-order, bounded scheme. Moreover, for the discretization of gradient terms, the Gauss cubic scheme has been chosen. This scheme is third-order accurate. In fact, in Finite Volume Method (FVM) terms, it uses a 3rd order polynomial to interpolate the field values at the common face between two adjacent cell centers. Furthermore, Gauss cubic and Gauss limited cubic are the chosen divergence schemes. More specifically, these third-order accurate schemes are used to discretize the convective terms involved in the present system of equations. Typically, in a CFD problem, these terms are the most problematic in discretization due to their highly non-linear nature. Therefore, a careful selection of the numerical schemes is required when it comes to the discretization of convective terms. As a consequence, a high-order scheme is selected for such a task and flux limiters are used to preserve stability. On the other hand, from the point of view of Laplacian schemes, the Gauss cubic corrected scheme is used to discretize the terms in charge of the diffusion phenomena. Finally, cubic interpolation schemes and corrected surface normal gradient schemes are also employed.

The NS-equations governing the physics of the methanol synthesis in the reactor are implemented in Open Source Field Operation and Manipulation (OpenFOAM) software version 10. OpenFOAM is an open-source CFD code that utilizes the FVM to discretize NS-equations and solve them iteratively [64]. Being equipped with a number of different pre-defined utilities and solvers, OpenFOAM is capable of addressing a wide range of applications in fluid dynamics. In the present study, the required solver should be capable of accurately computing and monitoring the evolution of the fields in compressible flows featuring chemical reactions. For this purpose, the reactingFoam solver has been selected. This solver performs the iterative computation based on Fick's law and $Le_k=1$.

2.4 Pressure-velocity coupling

Coupling between pressure and velocity fields has been performed using the PIMPLE algorithm. This algorithm provides an iterative, transient solution to fluid flow problems by combining the two standard methodologies, semi-implicit method for pressure-linked equations (SIMPLE) and pressure-implicit split-operator (PISO) [65]. The SIMPLE algorithm is used for solving flows that achieve a steady-state. In alternative phrasing, the algorithm is used to address cases in which the computed flow fields become constant with time. It also offers decent estimates to unsteady-flow cases at a lower computational effort compared to methods that solve the transient problem. By assuming steady-state conditions, this algorithm nullifies all the time-derivative terms present in the governing equations of interest, *i.e.* $\frac{\partial}{\partial \mathrm{t}} = 0$. In short, the procedure adopted by the SIMPLE algorithm for combining the mass and momentum conservation equations and solving them iteratively is the following:

1) The energy matrix is formed and T is solved for by using under-relaxation.

2) Applying a state equation, the resultant T is used for computing the new value of the density $\rho(T,p)$.

3) The matrix that corresponds to the momentum equation is constructed, but without the ∇p term.

4) $\boldsymbol{u}$ is resolved by under-relaxing the previous momentum matrix equation and setting it equal to $-\nabla p$.

5) The obtained value of $\boldsymbol{u}$ is then implemented in the pressure equation to solve for p.

6) The calculated p is then plugged into the flux corrector equation to update the value of the flux (Φ_f) in a way to better fulfil the mass conservation.

7) Using the latest obtained flux, $\boldsymbol{u}$ is corrected and the loop repeats until the desired, set number of iterations is reached.

SIMPLE is only concerned with steady-states. Thus, the algorithm does not involve any time-stepping or consideration of time-dependent terms.

On the other hand, the PISO algorithm is used to attain transient fluid-flow solutions along subsequent timesteps (Δt) over a specified time interval $\left(\frac{\partial}{\partial \mathrm{t}} \neq 0\right)$. The smaller the timestep at which the iterative solution advances in time, the higher the accuracy, but the larger the computational cost; hence, this must be tuned based on the required level of precision. Using the PISO approach, the under-relaxation technique is not required. Due to its high computational cost, this algorithm solves the system of equations of the SIMPLE algorithm only once each timestep, with the addition of an iterative loop, called PISO, which plugs the $\boldsymbol{u}$ obtained by the momentum corrector back into the pressure equation to solve it once again during the same timestep. In other words, pressure and therefore, the momentum corrector equation are solved multiple times per timestep, which guarantees more accurate results of p, $\boldsymbol{u}$ and Φ_f.

Initializing the new iteration with this new corrected value of $\boldsymbol{u}$ decreases the level of error in the temporal derivatives. Briefly, the methodology is executed according to the sequence elaborated below:

1) The energy matrix is constructed to solve for T.

2) T is used to update ρ and construct the momentum matrix equation.

3) $\boldsymbol{u}$ is obtained by solving the matrix of the momentum equation.

4) This $\boldsymbol{u}$ is implemented in the pressure equation to solve for p.

5) The obtained p is inserted into the momentum corrector to achieve a new value of $\boldsymbol{u}$.

6) Due to the additional PISO loop, the recently calculated $\boldsymbol{u}$ put once again back into the pressure equation to update p.

7) This updated p is plugged into the momentum corrector to get a corrected value of $\boldsymbol{u}$.

8) Finally, this new velocity is set into the flux corrector for updating Φ_f. At this stage, the CFD quantities of interest at the current timestep, p, $\boldsymbol{u}$, Φ_f and T are calculated and the advancement onto a new timestep occurs. This sequence keeps on repeating itself until reaching the end of the simulation time.

Using PIMPLE blends the SIMPLE and PISO algorithms, especially in terms of the iterative approach and the under-relaxation concept. This yields an enhancement in accuracy as the variables are now updated throughout the timestep, thanks to the addition of the PIMPLE loop. This relatively improves the solution of the system of equations.

3 Simulation case set-up

In this section, an elaborate explanation is provided regarding the reactor's main geometry and the corresponding 2D model utilized in the simulations. Furthermore, an overview of the various simulation cases examined in the thesis is presented, along with the corresponding boundary conditions (BCs). Additionally, the different tested *Re* are addressed, including a computation of the required bulk flow velocities at the channel inlet and the simulation run-times. Finally, the mesh characteristics are described in each case, followed by a comprehensive study on mesh convergence.

3.1 Reactor geometrical characteristics and features

The original microchannel reactor segment under investigation has a relatively simple geometry, *i.e.* a standard rectangular duct (Figure 1). As described in the introductory section, such a reactor design offers several advantages from a fluid-dynamic standpoint, like enhanced heat and mass transfers, in addition to high single-pass efficiencies. However, the main downside remains the low absolute methanol throughput, which limits the use of such reactors to special applications.

The reactor is characterized by a 2mm×2mm cross-sectional area (Figure 2). Cross-sections of such a dimensional range are typical of microchannel reactors [66]. As depicted in Figure 1, the reactive fluid mixture flows from left (inlet) to right (outlet). The overall streamwise length of the channel is 37mm, divided into two main regions: the recycling zone and the reacting zone. Starting from the inlet section, the recycling zone covers the first 13mm. This zone isn't catalytically coated by any means, thus, it doesn't witness the occurrence of chemical reactions. Explicitly, the recycling zone is only responsible for stabilizing the fluid flowing from the reactor's inlet. This implies a fully-developed flow profile entering the reacting zone. On the other hand, the remaining 24mm, from the end of the recycling zone until the outlet section, are covered by the reacting zone. A catalytic material is applied over the solid walls of the duct in this region. The surface chemical reactions that govern the methanol synthesis commence at the catalytic walls, just upon the impingement of the fluid on them. As a result, reactants (H_2 and CO_2) begin converting to methanol (CH_3OH) and its corresponding by-products (CO and H_2O).

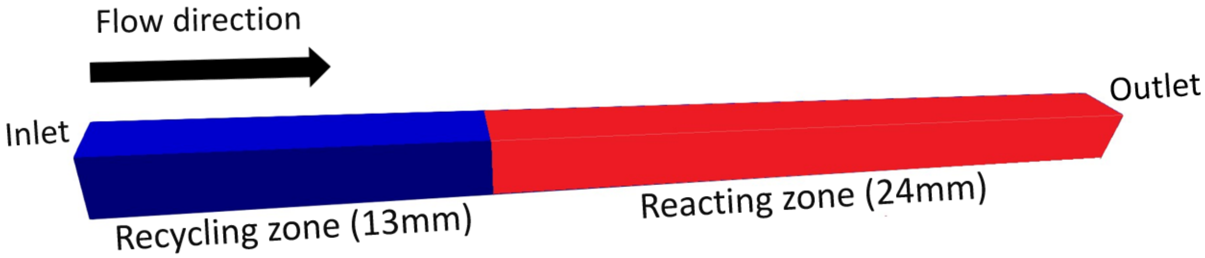

Figure 1. A schematic showing the rectangular microchannel reactor in 3D.

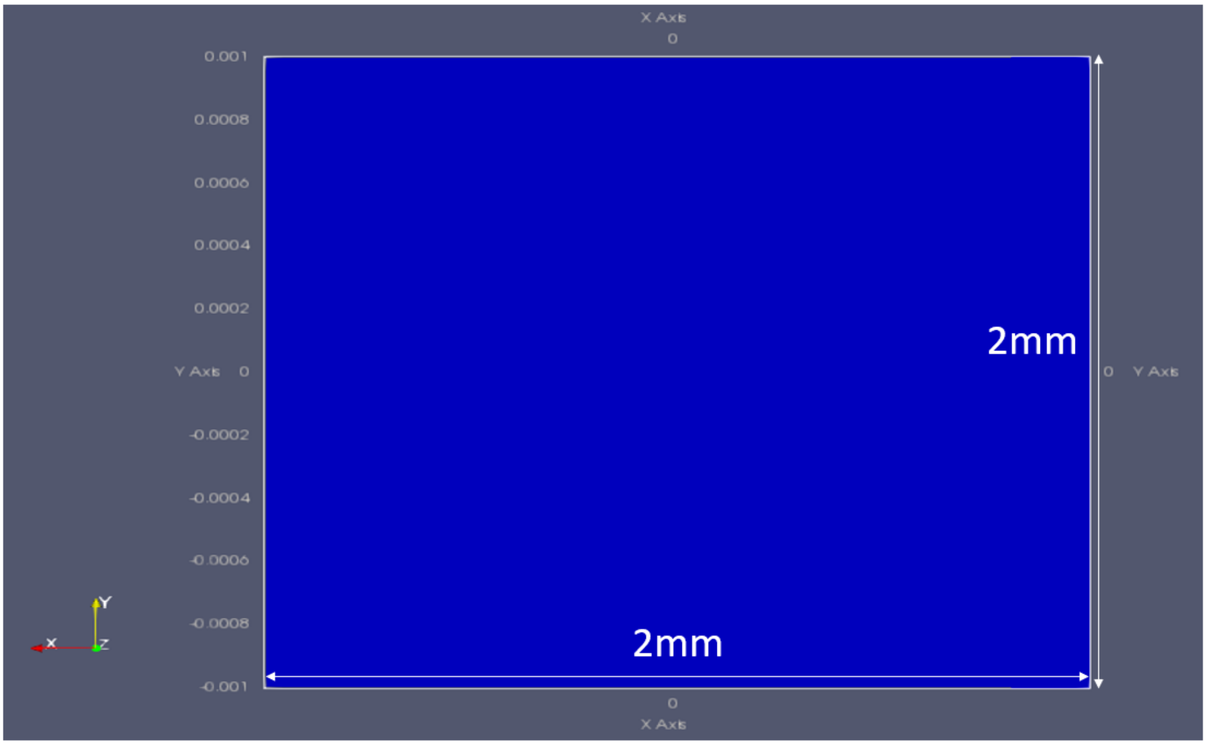

Figure 2. An OpenFOAM schematic representing the cross-section of the methanol reactor.

However, simulating the catalytic synthesis of methanol over a three-dimensional domain proves to be extremely expensive, as far as computational cost is concerned. This is primarily attributed to the extremely small chemical timesteps required to accurately capture the progress of the chemical reactions and preserve stability. Consequently, performing such simulations on standard academic computational resources might not be feasible. Therefore, the analysis is solely performed in the *x*-*z* plane, on the 2D slice of the original 3D segment, presented in Figure 3. The size of the adopted planar computational domain is 2mm along the vertical direction (*x*) and 37mm along the horizontal direction (*z*).

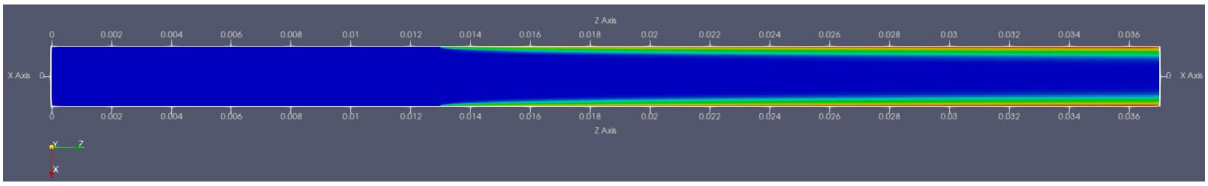

Figure 3. An OpenFOAM schematic showing the 2D slice of the rectangular duct-type methanol reactor, on which the simulations are performed.

3.2 Simulation cases and boundary conditions

The simulations conducted throughout the thesis can be categorized into three groups: (A), (B) and (C). Initially, the focus is on simulating the catalytic methanol synthesis in the 2D channel under perfectly laminar flow conditions. In these circumstances, two specific scenarios are addressed. First, the simulations are performed with the reactor featuring both, a recycling zone and a reacting zone. These are classified as group (A) simulations. On the other hand, simulations of group (B) are performed with the reacting zone covering the entire length of the reactor, *i.e.* without a flow recycling zone, as depicted in Figure 4.

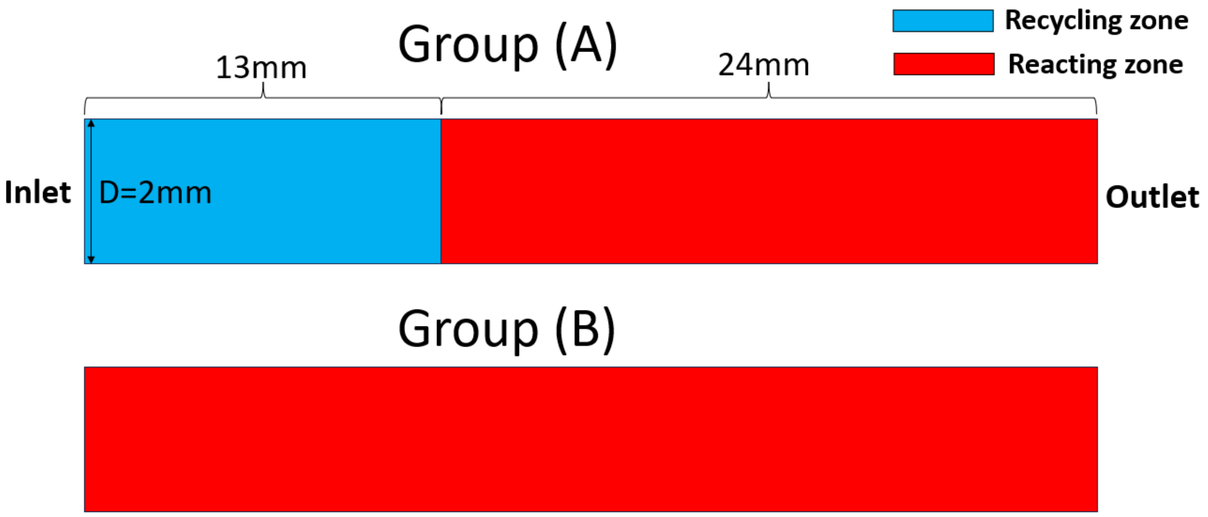

Figure 4. A scheme describing the two cases examined in the laminar flow simulations. The upper scheme shows the dimensions of the different sections of the reactor when it features flow recycling (Group (A)), while the bottom scheme shows the reactor after the omission of the recycling zone and the extension of the reactive zone towards its inlet section (Group (B)).

Moreover, following the analysis of the reactor under fully laminar conditions, VGs are introduced downstream of the inlet section. These are referred to as the simulations of group (C). In these simulations, two different configurations of VGs are investigated. The first configuration comprises three-squared obstacles arranged in a spanwise row (Figure 5-i), while the second one consists of a single vertical rectangular obstacle (Figure 5-ii).

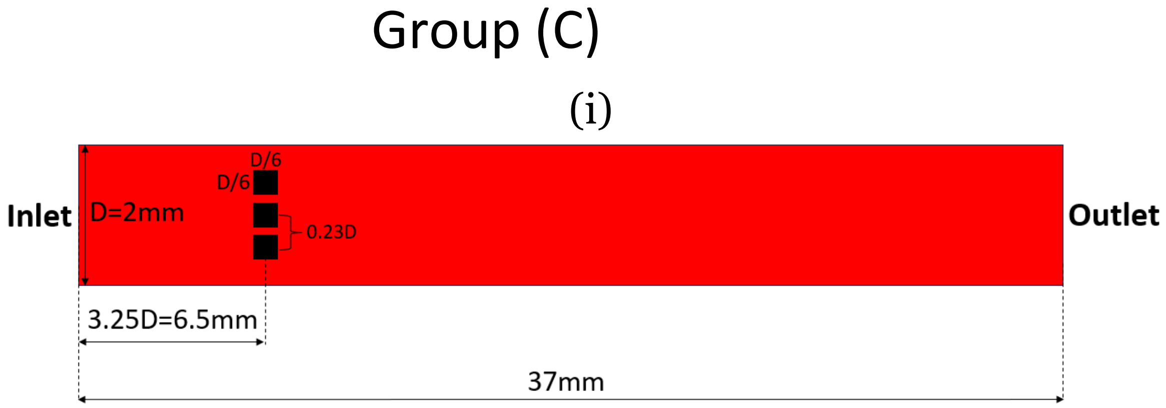

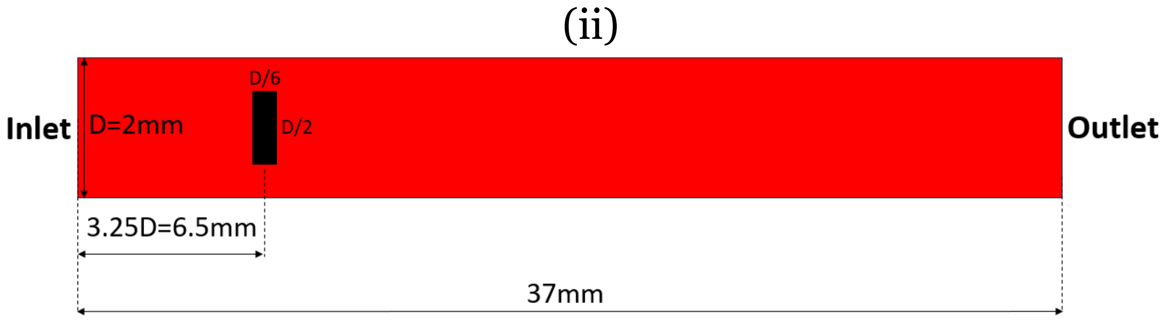

Figure 5. A scheme describing the geometry of the reactor after installing vortex generators (VGs). The first configuration has the form of three square-shaped obstacles aligned in a spanwise row (i), while the second is a vertical rectangular obstacle (ii). These simulations are classified under group (C).

The encountered CFD problem in the current catalytic reactor pertains to the category of subsonic, compressible, reactive flows as specified in section 2.1. Therefore, to achieve unique, non-singular solutions to the discretized system of equations, proper BCs have been set to velocity and pressure at every boundary patch of the computational domain.

The addressed cases are bi-dimensional along the x-z plane, where positive x points vertically downwards and positive z is oriented from left to right, *i.e.* along the direction of the flow. Hence, empty BCs have been assigned to all boundary patches present in the plane perpendicular to y. Patches normal to the y-axis have zero contribution in 2D flows along the x-z plane. In general, for all cases, the boundary of the channel-type reactor is at least composed of an inlet and an outlet (along the z-normal direction) and the upper and lower walls (along the x-normal direction).

In the initial simulations, in which a recycling zone is included in the channel, the walls are divided into two groups. Starting from the inlet, the top and bottom wall segments along the first 13mm are the recycling walls, where no chemical reactions occur. From the interface between the recycling and reacting zones until the outlet section, the covered upper and lower wall segments are the catalytic walls, where reactions may occur (Table 4). However, in the proceeding laminar flow simulations, the recycling zone is omitted and a catalyst coating is applied in its place. This enables methanol synthesis reactions to take place along the entirety of the channel. In these cases, the upper and lower wall segments spanning the full length represent a unique boundary group, *i.e.* catalytic walls (Table 5). More precisely, a unified set of BCs is assigned at these walls as no splitting is involved.

Finally, VGs are introduced in the reactor. Also in these situations, the catalyst coating is applied at the walls over the entire length of the reactor. Therefore, they form a single boundary group as in the latest laminar case. Additionally, in these cases, the obstacles created downstream of the inlet contribute to the boundary of the computational domain. For both configurations, the combination of the three square-shaped obstacles and the vertical rectangular obstacle form a single boundary group in their respective cases, *i.e.* vortex generator (Table 6).

Table 4. A summary of the boundary groups present in the cases in which the flow is perfectly laminar and a recycling zone is present.

Group (A) simulations				
Boundary groups	Inlet	Recycling walls	Catalytic walls	Outlet

Table 5. A summary of the boundary groups present in the cases in which the flow is perfectly laminar and the catalyst coating is applied over the entire length of the reactor.

Group (B) simulations			
Boundary groups	Inlet	Catalytic walls	Outlet

Table 6. A summary of the boundary groups present in the cases featuring vortex generators.

Group (C) simulations				
Boundary groups	Inlet	Catalytic walls	Vortex generator	Outlet

The BCs for velocity and pressure have been chosen to ensure optimal coupling, which guarantees non-singular solutions. Velocity and pressure fields are correlated by the momentum equation and hence, assigning incompatible BCs leads to under-determined or over-determined systems of equations. Therefore, the BCs along the computational domain have been set accordingly.

For instance, in group (A) simulations, a mapped BC for velocity is set at the inlet of the channel. An initial fixed value of velocity is assigned at the inlet and then corrected by mapping to it the average velocity at the interface between the recycling and reacting zones, at every timestep. This allows for a faster attainment of a fully-developed laminar velocity profile. For the remaining simulation cases, in which the recycling zone is removed, no mapping is necessary to correct the inlet velocity. Therefore, a uniform, non-zero fixed-value (non-homogeneous Dirichlet) for velocity is assigned at the inlet. In addition to that, in group (C) simulations, no-slip BCs are set at the vortex-generating obstacles, *i.e.* the velocity of the fluid layers in contact with the obstacles is zero (homogeneous Dirichlet). In all simulated cases, at all walls and at the outlet section of the reactor, no-slip and inlet-outlet BCs are chosen, respectively.

Concerning the pressure field, the zero-gradient (homogeneous Neumann) is applied at the inlet and all solid walls, while a fixed value of 5MPa is set at the outlet section. This value corresponds to typical pressure conditions present in real-world reactors. Such pressure ranges are convenient for the catalyst activity and consequently, methanol synthesis [67]. In the simulations of group (C), the only additional pressure BC, with respect to groups (A) and (B), is the assignment of zero-gradient BCs at the borders of the obstacles.

The temperature BCs in the two-dimensional channel are chosen such that a finite temperature difference between the catalytic walls and the flowing mixture of species triggers a heat exchange. First, for group (A) simulation cases, the recycling walls are assigned a zero-gradient BC. The presence of this region is solely for allowing the flow to develop completely before enter the reacting zone. Therefore, no heat transfer occurs between these walls and the fluid mixture. In all cases, fixed-value BCs are set at each, the inlet section and the catalytic walls, such that the temperature at the walls is always 20°C higher. This causes a heat transfer from the catalytic walls to the fluid. Isothermal conditions are maintained at the catalytic walls and several temperatures are tested in the range 200-250°C, which is within the operating temperature range of the catalyst. The inlet temperature (T_{inlet}) is changed accordingly to maintain the 20°C difference discussed above. In addition to that, the outlet section of the channel features zero-gradient BCs in all cases. Finally, for simulations belonging to group (C), the temperature BCs implemented at the obstacle edges are of a zero-gradient type.

The BCs pertaining to the chemical species are selected to guarantee a catalytic synthesis of methanol under stoichiometric conditions. All species, reactants and products, have fixed-value BCs at the inlet and zero-gradient at the outlet. Concerning the reactants, CO_2 and H_2 are initialized at the inlet section with mass fractions of 0.88 and 0.12, respectively, *i.e.* Y_{CO_2}=0.88 and Y_{H_2}=0.12. Such initialization ensures that the number of moles of H_2 (n_{H_2}) is three times that of CO_2 (n_{CO_2}), *i.e.* $\frac{n_{H_2}}{n_{CO_2}} = 3$. This leads to a stoichiometric methanol hydrogenation (Eq. 11). For the products' mass fractions (Y_{CH_3OH}, Y_{CO} and Y_{H_2O}), they are all assigned homogeneous Dirichlet BCs at the inlet. At any solid wall, recycling or catalytic, the BC imposed for every chemical species is zero-gradient. Ultimately, for the cases falling under group (C), all species feature zero-gradient BCs at the sides of the vortex generators. Table 7 provides a summary of all the implemented BCs in this thesis.

Table 7. Summary of the boundary conditions implemented in simulation groups (A), (B) and (C).

Boundary conditions of group (A)				
	Inlet	**Recycling walls**	**Catalytic walls**	**Outlet**
U	Mapped	No-slip	No-slip	Zero-gradient
T	Fixed value	Zero-gradient	Fixed value	Zero-gradient
p	Zero-gradient	Zero-gradient	Zero-gradient	Fixed value (5 MPa)
Y_{CO_2}	Fixed value (0.88)	Zero-gradient	Zero-gradient	Zero-gradient
Y_{H_2}	Fixed value (0.12)	Zero-gradient	Zero-gradient	Zero-gradient
Y_{CH_3OH}, Y_{CO}, Y_{H_2O}	Fixed value (0)	Zero-gradient	Zero-gradient	Zero-gradient

Boundary conditions of group (B)			
	Inlet	**Catalytic walls**	**Outlet**
U	Fixed value	No-slip	Zero-gradient
T	Fixed value	Fixed value	Zero-gradient
p	Zero-gradient	Zero-gradient	Fixed value (5 MPa)
Y_{CO_2}	Fixed value (0.88)	Zero-gradient	Zero-gradient
Y_{H_2}	Fixed value (0.12)	Zero-gradient	Zero-gradient

Y_{CH_3OH}, Y_{CO}, Y_{H_2O}	Fixed value (0)	Zero-gradient	Zero-gradient

Boundary conditions of group (C)				
	Inlet	**Vortex generators**	**Catalytic walls**	**Outlet**
U	Fixed value	No-slip	No-slip	Zero-gradient
T	Fixed value	Zero-gradient	Fixed value	Zero-gradient
p	Zero-gradient	Zero-gradient	Zero-gradient	Fixed value (5 MPa)
Y_{CO_2}	Fixed value (0.88)	Zero-gradient	Zero-gradient	Zero-gradient
Y_{H_2}	Fixed value (0.12)	Zero-gradient	Zero-gradient	Zero-gradient
Y_{CH_3OH}, Y_{CO}, Y_{H_2O}	Fixed value (0)	Zero-gradient	Zero-gradient	Zero-gradient

3.3 Calculation of inlet flow velocities and required simulation run-times

The run-time needed to complete four channel passes is chosen in all of the simulated cases. The simulations performed in this thesis are velocity-controlled, *i.e.* the flow is driven by setting a uniform velocity profile at the inlet section. Depending on the chosen bulk flow velocity, the corresponding simulation is run for the time needed by the reactive fluid mixture to travel the length of the channel four times. In the present work, the catalytic synthesis of methanol is examined under four different bulk *Re*, *i.e.* *Re*=100, *Re*=200, *Re*=550 and *Re*=1100.

In the given reactor segment, the relation between *Re* and the bulk flow velocity (U) can be expressed as

$$Re = \frac{U_{inlet} \times h}{\nu}, \tag{20}$$

where h and ν are the half-width of the channel and the kinematic viscosity of the chemical species mixture, respectively. Thus, in the present 2D rectangular channel, the width is 2mm, *i.e.* h=1mm and the flowing fluid mixture is characterized by $\nu = 1.4896\times10^{-6} m^2/s$. This value of ν has been determined using Cantera for a gas mixture composed of Y_{CO_2}=0.88 and Y_{H_2}=0.12, at T=230°C and p=5MPa. Hence, U_{inlet} can be easily determined based on the chosen *Re*.

Concerning the simulation run-time ($t_{simulation}$), it is calculated using the basic displacement formula, *i.e.* $t=d/U$, where t, d and U correspond to time, distance and velocity, respectively. Simulating the synthesis for a time equivalent to four passes, the required run-time in each case is calculated as $t_{\text{simulation}} = \frac{4L}{U_{\text{inlet}}}$, where L is the streamwise dimension of the channel (37mm).

Table 8. A summary of the inlet velocities corresponding to the different tested Reynolds numbers and the simulation run-times equivalent to four pass-times.

	Re=100	Re=200	Re=550	Re=1100
U_{inlet} [m/s]	0.149	0.298	0.819	1.639
$t_{\mathrm{simulation}}$ [s]	1	0.5	0.182	0.091

3.4 Mesh-related aspects

In this subsection, the methodology adopted for mesh generation is elaborated for each case and the corresponding mesh characteristics are reported. Subsequently, a mesh convergence study is conducted.

3.4.1 Mesh generation and characteristics

As depicted in section 3.1, the flow in the present 2D reactor is directed from left (inlet) to right (outlet), along the positive *z*-direction, in all studied cases (Figure 1). For simulations pertaining to group (A), the mesh is generated using the standard blockMesh utility in OpenFOAM. It is made up of two blocks, where one corresponds to the recycling zone and the other to the reacting zone. The blocks are combined and attached using mergeMesh and stitchMesh utilities. The mesh consists of 26048 cells of the hexahedral type, with 64 cells along the wall-normal direction and 407 cells along the direction of the flow. A grading factor of 12.5 is chosen over the vertical dimension, from the middle to the upper and lower walls along the entire length of the channel. This grading factor is defined as the width of each cell located at the walls of the reactor is 12.5 times smaller than that of its central cells. Moreover, the maximum cell aspect ratio, *i.e.* the ratio of the length to the width, is 13.466. Referring to this specific context, this value is found at the smallest cells of the present computational domain, in particular, the ones placed at the walls. Additionally, the mesh is characterized by a perfectly orthogonal arrangement of cells. Namely, the degree of non-orthogonality is zero all over the computational grid. Proceeding to simulations of group (B), the only difference is that only one block is needed in this case. Otherwise, all the above-mentioned mesh characteristics are maintained. The mesh still consists of 26048 cells, with 64 cells located along the wall-normal direction, zero non-orthogonality degree, same maximum cell aspect ratio and most importantly, same refinement topology, *i.e.* grading factor (Figure 6).

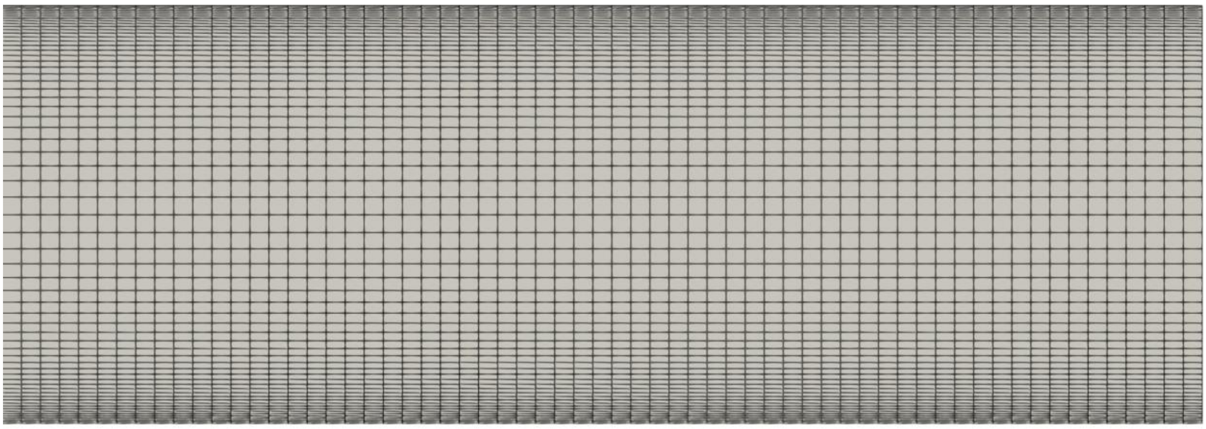

Figure 6. An OpenFOAM schematic describing the mesh used in the laminar flow simulations.

On the other hand, concerning the cases which belong to group (C), a different mesh generation procedure has been followed. Starting from the mesh represented in (Figure 6), for generating vortices in the flow, obstacles are required inside the reactor. This has been achieved by creating hexahedral obstacles at 6.5mm downstream of the channel's inlet section (Figure 5). Since two different configurations of VGs are tested, a mesh is generated for each case, having a different obstacle placement to correctly resemble the particular VG. Computer-Aided Design (CAD) tools have been utilized to create the obstacles' geometries. Then, they have been imported in OpenFOAM as STL files and incorporated in the mesh by the snappyHexMesh utility.

For the case in which the VG is in the form of three squared obstacles aligned in a spanwise row (Figure 7), three vertically-aligned identical squared elements have been created. The side of each square (d) is one-sixth of the duct width (D), *i.e.* $d=D/6$. The general mesh grading factor is maintained at 12.5 between the middle of the channel and the catalytic walls. Also, the number of cells along the width of the channel remains 64. However, two additional refinement techniques have been implemented in the settings of snappyHexMesh dictionary. First, a grade 4 refinement has been done at the edges of the obstacles using the refinementSurfaces sub-dictionary. More precisely, the cells at the borders of the vortex-generating elements have become $2^4=16$ times greater and the refinement has been done gradually along three layers of cells. This incremental refinement of the grid at this region is needed to maintain a convenient cell aspect ratio, which in turn, diminishes interpolation errors and maintains stability. The second refinement has been done using the refReg sub-dictionary. A refinement region, of type "searchableBox", has been created around the obstacles. The level of refinement has been set to 1, which implies that the cells enclosed by the refinement box are doubled. The box covers the whole width of the duct and a length equal to $5d$. Specifically, the refinement starts at $1d$ upstream the VG until $3d$ downstream of it (Figure 7). These supplementary refinements have increased the number of cells to a total of 32484. The maximum cell aspect ratio is 13.466 in this case. Furthermore, after the inclusion of the obstacles, the mesh is no longer perfectly orthogonal. Indeed, a certain degree of non-orthogonality started to appear around the edges and corners of the obstacles. A maximum mesh non-orthogonality degree of 44.207° and an average of 3.579° have been recorded.

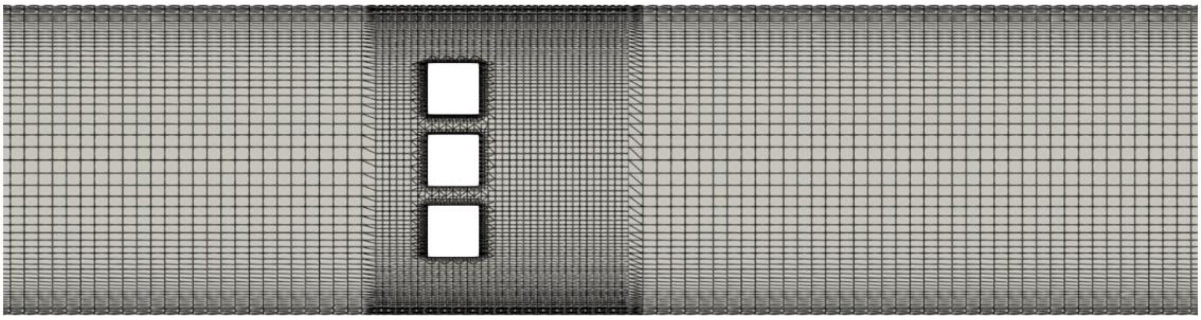

Figure 7. An OpenFOAM schematic showing the mesh characteristics and refinement around the vortex generators in the case in which they are aligned in a spanwise row.

The mesh in the case where a single rectangular obstacle has been installed for generating vortices features the exact same properties as that of the square-shaped obstacles. In essence, the only difference is that instead of three squared obstacles, a vertical rectangular obstacle is created (Figure 8). The dimensions of the rectangular obstacle are the result of placing the previous three squared obstacles on top of each other, with no gaps in between. Precisely, the rectangular element has a length of $D/6$ and a width of $D/2$ as depicted in (Figure 5-ii). The corresponding computational grid consists of 31696 cells, with a maximum cell aspect ratio of 13.478. As far as non-orthogonality is concerned, the maximum is 42.531°, while the average is 2.666°. As a matter of fact, the degree of mesh non-orthogonality exhibited in group (C) simulations is considered relatively low. Therefore, no severe inaccuracies are expected to result from that. Table 9 presents a summary of the mesh properties employed in the simulations conducted for groups (A), (B) and (C).

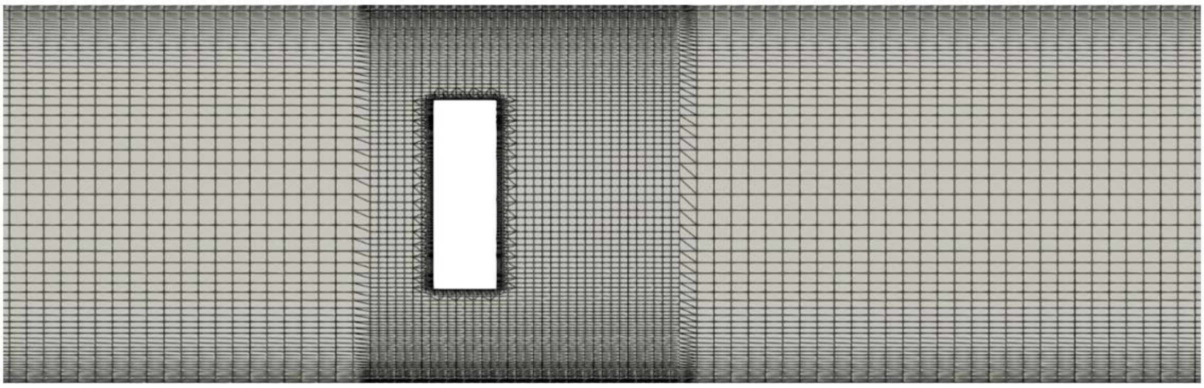

Figure 8. An OpenFOAM schematic showing the mesh characteristics and the refinement around the vortex generator in the case in which it is in the form of a vertical rectangular obstacle.

Table 9. A summary of the main mesh characteristics in each of the performed simulations

Mesh case	Total number of cells	Maximum cell aspect ratio	Average non-orthogonality degree	Maximum non-orthogonality degree
Laminar	26048	13.466	0	0
Squared obstacles	32484	13.466	3.579°	44.207°

Rectangular obstacle	31696	13.478	2.666°	42.531°

The motive behind adopting a mesh refinement and consequently, improving the computational resolution close to the catalytic walls is that these regions embrace the most significant physical phenomena of the entire duct-type reactor (Figure 6). First, in a chemical context, methanol reactions begin only once the fluid mixture is in-contact with these catalytic walls. Therefore, mesh densification is necessary to accurately monitor the progress of these chemical reactions. Another reason to adopt such a refinement is that the velocity field and each of the species' mass fraction field have their steepest gradients there. From the point of view of velocity, the implementation of the no-slip BC at the upper and lower walls has led to quite steep velocity gradients in these locations. In simpler terms, velocity sharply drops to zero once the fluid touches the walls. Concerning the chemical species, since only surface reactions are accounted for, their corresponding mass fraction gradients are significantly high around the two walls. The reactants display steeply decreasing profiles due to being consumed in the reactions. On the contrary, the formation of new products leads to rapid increases in their mass fractions. Furthermore, the most significant temperature gradients are localized in the reacting zone, specifically, at the upper and lower interfaces between the catalytic walls and the fluid. This is attributed to the starting temperature difference of 20°C between them. As a result, placing an increased number of cells in these parts of the channel is necessary in order to correctly track the conductive and convective heat transfer phenomena. Finally, enhancing the computational grid quality near the walls of the rectangular channel permits a highly-accurate visualization of the boundary layer growth of the different present fields. Essentially, in all cases, the velocity boundary layer starts forming as soon as the reactive fluid mixture enters the reactor. On the other hand, species and temperature boundary layers start to develop only at the catalyst-coated walls. Namely, in the laminar cases that don't feature flow recycling, all boundary layers initiate at the inlet of the duct and continue developing along the axial direction until the outlet section. All the above-mentioned considerations justify the necessity of adopting a high-quality mesh next to the walls.

A special treatment of these sections is crucial in all simulation cases. For the cases in which the flow characteristics in the channel are perfectly laminar, the refinement settings discussed above are adequate. On the other hand, when flow mixing is induced with the introduction of VGs (Figure 7 and Figure 8), additional refinements are required. Indeed, a local refinement just at the edges of the obstacles is necessary due to the implementation of no-slip BCs. Moreover, increasing the number of cells along the full width of the duct in the local area in which the VG is located is also crucial. This region features the pivotal fluid dynamic phenomena in the reactor. The interaction between the fluid mixture and the existing obstacles, along with the subsequent flow over them, gives rise to unsteady flow conditions. This includes back-flow, cross-flow and most importantly, the formation of vortex structures. Therefore, a dense mesh is used to properly capture the vortices and ensure highly-accurate results. It is also important to highlight that insufficient levels of computational accuracy could lead to major instabilities in regions involving steep gradients, which might cause simulation blow-ups in extreme cases.

3.4.2 Solver settings and mesh convergence study

As mentioned in section 2.4, the PIMPLE algorithm has been chosen for coupling the velocity and pressure fields. This algorithm is convenient for both, cases in which steady-state is achieved, *e.g.* the initial laminar flow simulations and for time-dependent, unsteady flows, *e.g.* simulations featuring VGs. In all of the studied cases, the PIMPLE settings have been implemented in OpenFOAM such that the number of inner correctors is three. This implies that the pressure equation and consequently, the momentum corrector are solved three times per timestep. Moreover, the number of outer correctors has also been set to three. This allows looping over the whole system of equations and solving it three times during the single timestep. Controlling the solution of the momentum predictor has also been enabled. Concerning non-orthogonality correction, it is only required in the cases where the mesh features some non-orthogonality. Therefore, a single corrector loop has been added to account for non-orthogonality in the cases where vortex-generating obstacles are present. On the contrary, the mesh of the initial laminar simulations is perfectly orthogonal. Thus, it does not require any type of non-orthogonality correction.

At this stage, a mesh convergence study is carried out to determine the mesh characteristics that offer the best compromise between computational accuracy and cost. The mesh validation is performed on the reactor configuration that features a recycling zone and a reacting zone. In the tested case, the flow characteristics in the reactor pertain to the laminar regime. The bottom threshold operating temperature of the catalyst, *i.e.* 200°C, is set at the catalytic walls. At this temperature, the catalyst's activity and correspondingly, the reactions dictating methanol synthesis occur at their lowest rates. Since the involved chemistry is the bottleneck of the current study, conducting simulations at reduced reaction rates allows for the utilization of larger timesteps. The inlet temperature of the duct is set at 180°C. In this way, a starting temperature difference of 20°C is maintained between the entering fluid mixture and the walls at which reactions take place. The flow in the channel is characterized by Re=1100. Throughout all cases, this value of Re is the highest that has been simulated. According to laminar solutions of boundary layer equations [68], this value of Re results in the formation of the thinnest boundary layers among all simulations. Therefore, the goal is to validate a mesh of adequate quality, capable of effectively capturing even the thinnest boundary layers.

For this purpose, three meshes of different sizes have been proposed. The type of cells used in each mesh is hexahedral. All three meshes are perfectly orthogonal. The first mesh, *i.e.* the densest, is composed of 98304 cells, with 128 cells along the wall-normal direction and 768 along the axis of the duct. It has a maximum cell aspect ratio of 13.776. This mesh is referred to as M128 (Figure 9-A). The second mesh consists of almost quarter the number of cells of the previous one, *i.e.* 26048 cells. The cell division is made such that 64 cells are placed along the width of the channel and 407 cells along the streamwise direction. The corresponding maximum cell aspect ratio is 13.466. This mesh is referred to as M64 (Figure 9-B). Finally, the third mesh, M32, has the coarsest computational grid. It is made up of 13024 cells, such that it shares the same number of streamwise cells as M64, but along the spanwise direction, only 32 cells are present (Figure 9-C), which is half that of M64. M32 is characterized with a maximum cell aspect ratio of 6.844.

Table 10. A summary of the characteristics of M128, M64 and M32.

Mesh	Total number of cells	Maximum cell aspect ratio
M128	98304	13.776
M64	26048	13.466
M32	13024	6.844

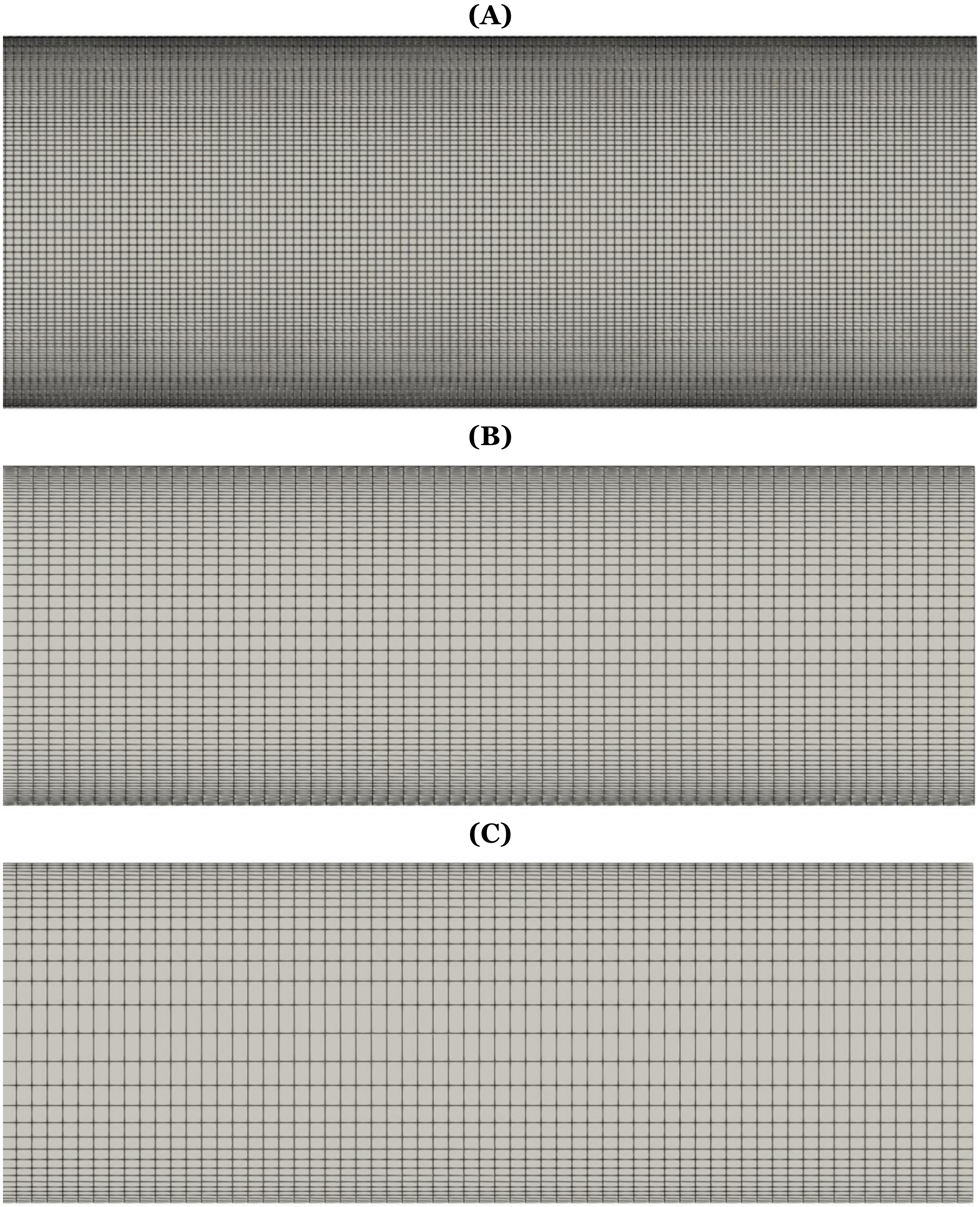

Figure 9. OpenFOAM schematics showing each of the three meshes tested in the mesh convergence study. M128 (top), M64 (middle) and M32 (bottom).

After generating the meshes shown in Figure 9, a comparison between their findings is performed. Essentially, the instantaneous boundary layer trends exhibited by their various fields, at the same positions in the duct, are compared. First, the streamwise component of the velocity field (U_z) displayed by each mesh is compared at the interface between the recycling and reacting zones. On the other hand, concerning the temperature and all chemical species' fields, the outlet of the channel is taken as the reference point.

First, exploring the trend of U_z exhibited by each of the three meshes, it can clearly be noticed that M32 features a notable offset around the middle of the duct, coupled with some slight deviations close to the upper and lower walls with respect to M128. On the other hand, the velocity field displayed by M64 is almost coincident with that of the M128 case (Figure 10). Hence, some inaccuracies arise from reducing the mesh resolution to M32 since the boundary layer contributions are no longer precisely tracked.

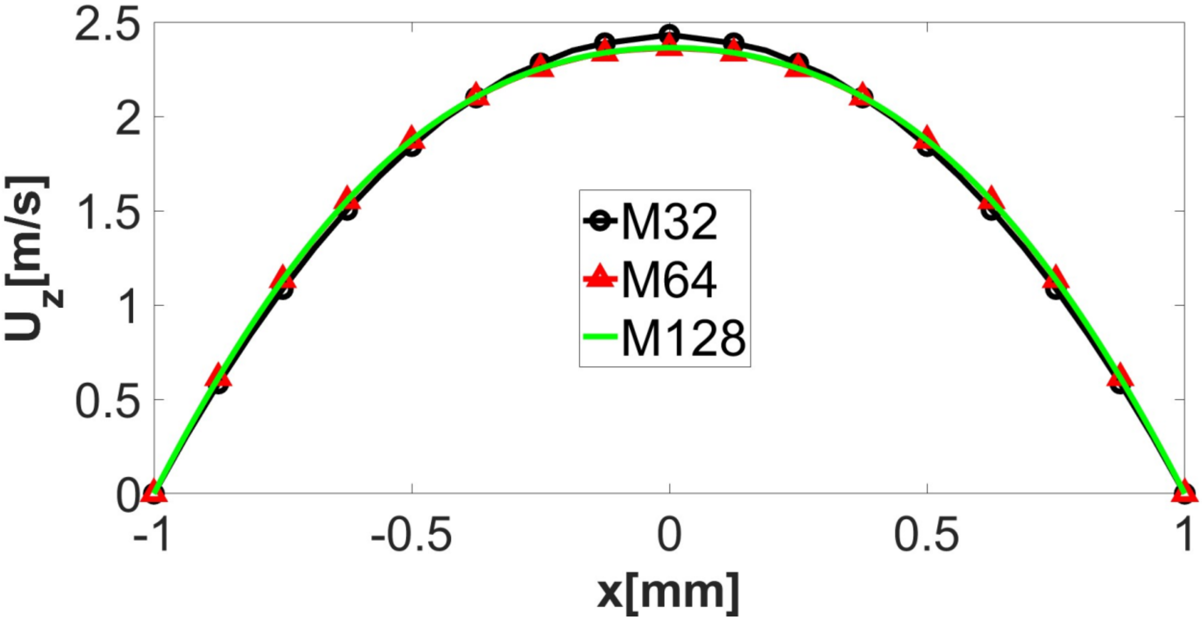

Figure 10. The instantaneous streamwise velocity component (Uz) along the wall-normal direction at the interface between the recycling and reacting zones of the reactor for all 3 meshes.

Moreover, concerning the temperature field, the differences among the three meshes are less apparent with respect to the streamwise velocity field. Both M32 and M64 perfectly match M128 near the axis of the reactor. However, moving towards the walls of the channel, M64 shows slightly smaller deviations from M128 as compared to M32 (Figure 11). In addition to that, throughout the course of the simulation, M32 has shown some instabilities and offsets in the temperature field, with the maximum temperature being several degrees higher than that set at the catalytic walls. On the other hand, M128 and M64 have both exhibited stable temperature fields that converge perfectly to the assigned temperature range, at almost every single timestep. This serves as an indication that M32 is too coarse to be used in the analysis.

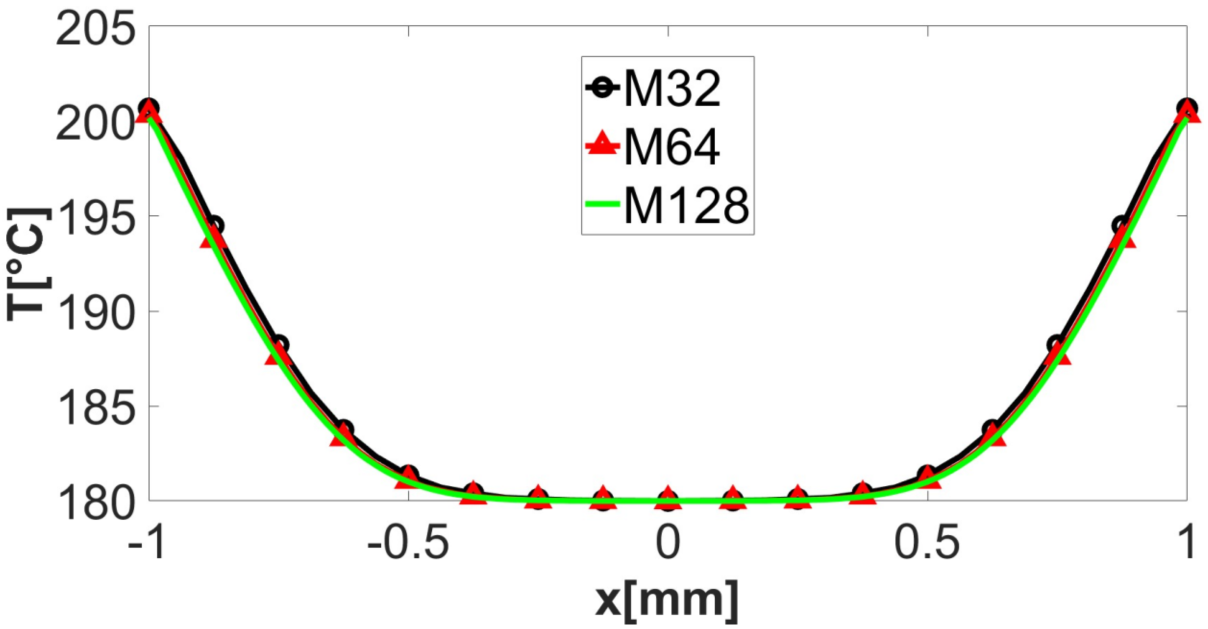

Figure 11. The instantaneous temperature field along the wall-normal direction of the reactor's outlet for all 3 meshes.

Furthermore, from the chemical species point of view, the outcomes are very similar to that of the temperature field. For example, checking the mass fraction of the reactants (CO_2 and H_2) for each of the three meshes, it is realized that in the region close to the center line of the channel, the three curves are perfectly overlapping. However, progressing towards the catalytic walls, M32 starts showing some offsets, with M64 and M128 maintaining a nearly-perfect match (Figure 12).

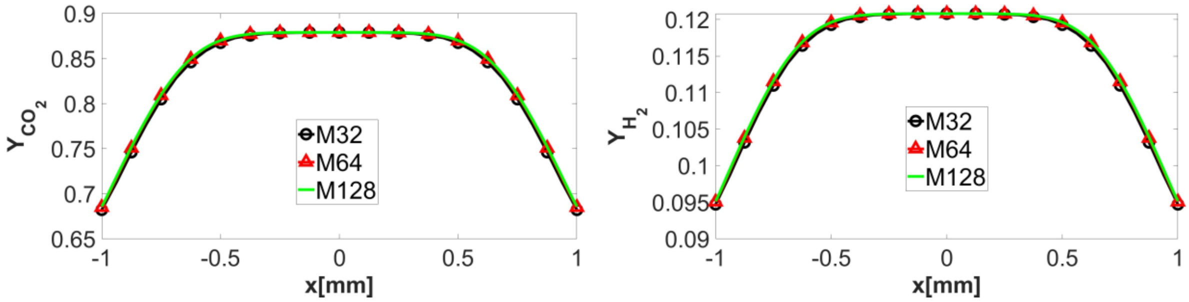

Figure 12. The instantaneous mass fractions of H_2 and CO_2 along the wall-normal direction of the reactor's outlet for all three meshes.

Regarding the formed chemical species (CH_3OH, CO and H_2O), overall, the outcomes are quite similar to the comparisons made over the preceding fields. As a matter of fact, in all three meshes, the mass fractions of the products are perfectly overlapping in the region surrounding the middle of the 2D reactor segment. However, near the catalyst-coated walls, deviations start to arise. For both, CH_3OH and H_2O, the differences are marginal between the three meshes. Nevertheless, the greatest offsets are reported by M32, while M64 and M128 almost share the same results (Figure 13). However, the discrepancies between the outcomes of M32 with respect to those of M64 and M128 become more apparent when addressing the mass fraction of carbon monoxide (Y_{CO}). Indeed, M64 and M128 almost display perfectly identical trends, while notable offsets are presented by M32.

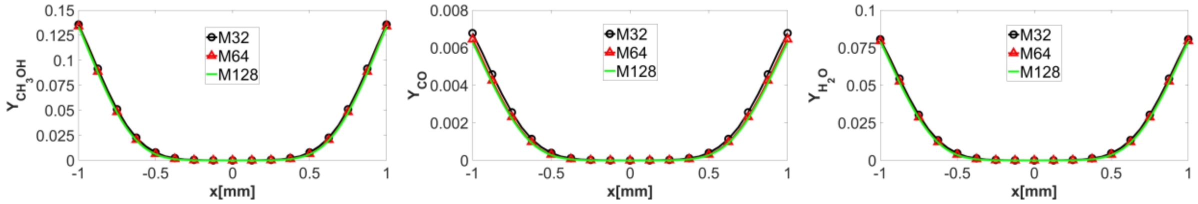

Figure 13. The instantaneous mass fractions of methanol, CO and H_2O along the wall-normal direction of the reactor's outlet for all three meshes.

In conclusion, this mesh convergence study reveals that coarsening the mesh from M128 to M64 maintains nearly equivalent computational accuracy at a number of cells which is almost four times fewer. In addition, adopting M64 instead of M128 permits setting a timestep (Δt) which is three times greater. Overall, this significant reduction in the number of cells and the increase in the value of the used Δt leads to saving a computational power in-excess of 995 CPU-hours, as further elaborated in Appendix.

On the other hand, although a further reduction in the mesh density to M32 doesn't result in catastrophic consequences, it starts hindering the computational precision. Therefore, M64 is confirmed as a valid mesh, which offers an optimal compromise between computational resolution and cost. Henceforth, this is the mesh employed in all laminar flow simulations. Concerning the cases in which VGs are placed inside the channel, their corresponding meshes are generated starting from M64, by creating the obstacles and performing some supplementary refinements around them, as described in section 3.4.1.

4 Results and discussion

After validating a relatively coarse mesh (M64), it is possible to conduct the 2D simulations in a highly efficient fashion. The goal is to study the effect of different thermo-fluid dynamic conditions on the performance of the reactor, *i.e.* on the methanol yield. In this section, the findings of the different set of simulations are presented and thoroughly analysed. For each of groups (A), (B) and (C), the analysis starts by presenting the trends of the fields of interest throughout the reactor. Afterwards, these fields are plotted along the width of the channel at the outlet section. Finally, the averaged values of the fields are computed at the reactor segment's discharge and the conversion efficiency of the reactor is analysed in each case.

4.1 Laminar simulations with a flow recycling zone (Group (A))

Initially, the catalytic synthesis of methanol is simulated in a 2D channel composed of a recycling zone and a reacting zone, as depicted in (Figure 4-A). The role of the recycling zone is only to allow the flow to fully develop by the time it enters the reacting zone. Reactions solely take place in the reacting zone. In these simulations, the reactor is tested under isothermal conditions at the catalytic walls in the operating temperature range of the catalyst (200-250°C), at 10°C steps. At every temperature, flow conditions corresponding to four different *Re*, *i.e.* *Re*=100, *Re*=200, *Re*=550 and *Re*=1100, are simulated. The goal of performing the group (A) simulations is to understand the effect of the bulk flow velocity (*U*) and the temperature (*T*) on the methanol yield. Consequently, the aim is to identify the most optimal combination of *T* and *Re*, at which the reactor achieves its best performance.

4.1.1 Instantaneous boundary layers and trends of different fields

The distribution of the streamwise velocity component (U_z) along the channel, exhibited by the reacting mixture of species, is presented in Figure 14, for each *Re*. The negative velocity gradient can clearly be observed as the fluid approaches the walls, which is expected after the imposition of no-slip BCs. Moving from the upper and lower walls, the velocity increases until achieving its maximum value in the middle of the channel.

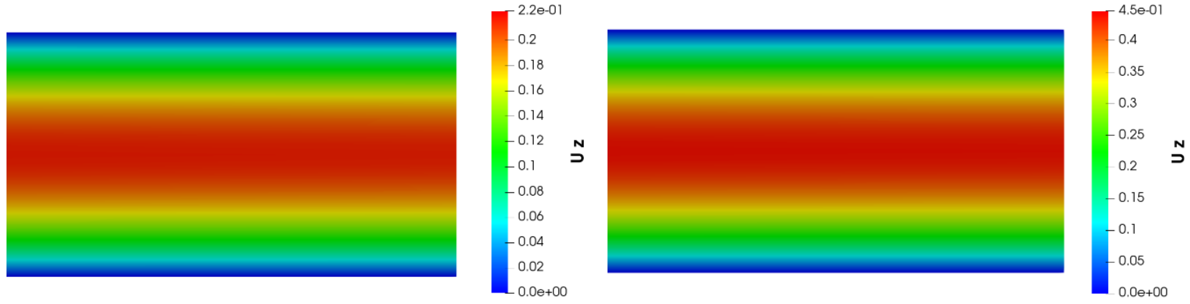
(A) *Re*=100 **(B) *Re*=200**

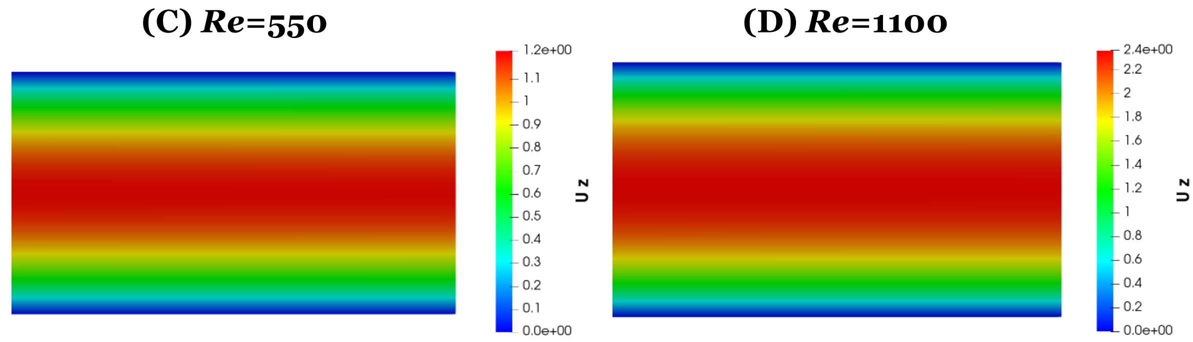

Figure 14. Velocity distribution of the flowing mixture along the 2D channel at *Re*=100 (A), *Re*=200 (B), *Re*=550 (C) and *Re*=1100 (D).

Plotting U_z over the wall-normal direction of the channel, at the interface separating the recycling and reacting zones, yields fully-developed, parabolic, laminar velocity profiles for each of the tested values of *Re* (Figure 15). This demonstrates that the species mixture achieves a completely-developed flow by the time it enters the reacting zone.

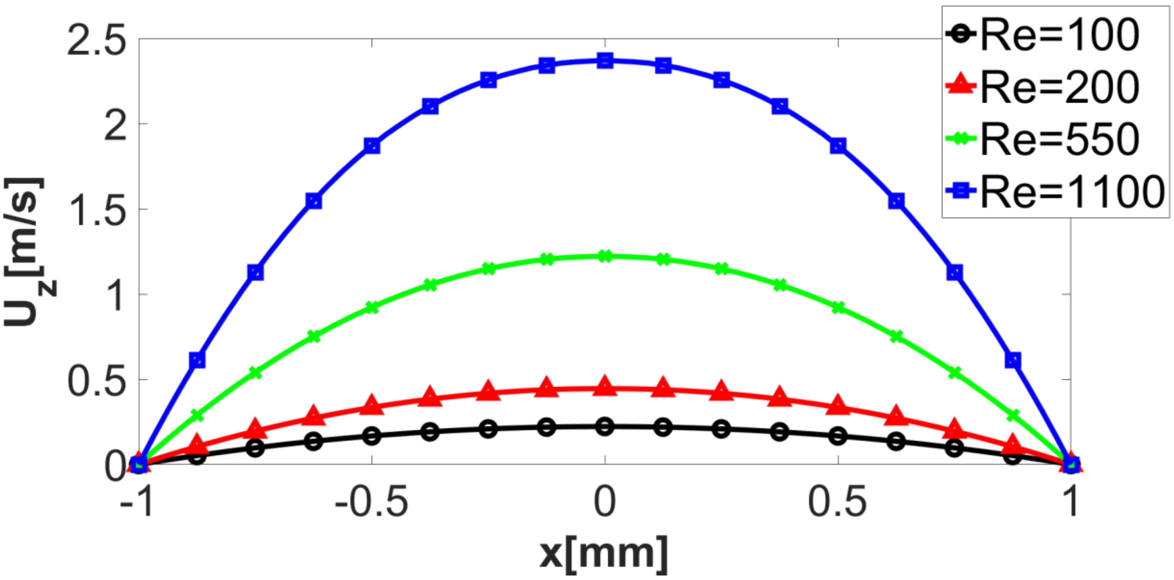

Figure 15. Streamwise velocity profiles along the wall-normal direction of the channel, at the interface between the recycling and reacting zones, for *Re*=100, *Re*=200, *Re*=550 and *Re*=1100.

Next, thermal (temperature) and chemical species (reactants and products) boundary layers are presented for every simulation of the parameter sweep. At every catalytic wall temperature (T_w), the boundary layers obtained by the four examined *Re* are plotted. It is important to remember that the temperature of the catalytic walls is selected to consistently exceed the inlet temperature of the reactor by 20°C, as stated in section 3.2. Moreover, the BCs are set such that no heat transfer occurs between the recycling walls and the fluid. Therefore, a 20°C temperature difference between the reactive mixture and the catalytic walls is maintained at the onset of the reacting zone. Thus, heat transfer phenomena only take place throughout the reacting zone.

Starting from T_w=200°C, before precisely comparing the fields of interest at the four distinct *Re*, the trends exhibited by the various fields at *Re*=550 are presented. The motive behind showing these trends is to roughly describe the boundary layer formation and development for temperature and the present chemical species. The physics involved in this case is the same as that of all other cases, with the only differences being the magnitudes and boundary layer widths. Therefore, these trends are thoroughly representative of the whole methanol synthesis process.

Referring to Figure 16, the thermal boundary layer forms as soon as the fluid mixture enters the reacting zone and engages with its catalytic walls. This boundary layer is a result of the conductive heat transfer between the walls and the stationary fluid layers in direct contact with them and the convective heat transfer phenomena occurring internally among the moving fluid particles themselves. This is attributed to the finite temperature difference (20°C) between the solid walls and the fluid entering the reacting zone. Another factor which contributes to the heat transfer inside the channel is the exothermicity of the reactions producing methanol (Eqs. 10-11). Namely, the formation of methanol from the hydrogenation of either, CO or CO_2, results in an additional heat release in the reactor. The boundary layer initiates at the walls just downstream the interface separating the recycling and reacting zones. From this point onwards, it continues developing until the outlet section of the reactor. Furthermore, as can be expected from such a channel heat transfer situation, *i.e.* from the top and bottom walls to a fluid travelling at a low *Re*, the least influenced regions of the fluid are the farthest from the catalytic walls. In fact, a negative temperature gradient can be visualized from the walls to the bulk of the channel. Accordingly, the fluid layers around the middle of the channel are unaffected by the heat exchange in this case. These fluid layers represent the so-called free-stream region.

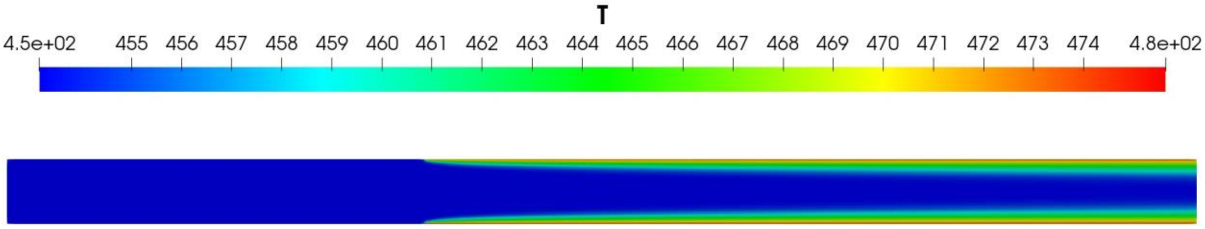

Figure 16. The temperature boundary layer trend along the methanol reactor at T_w=200°C and *Re*=550.

Referring to the boundary layers exhibited by the reacting chemical species (Figure 17), *i.e.* Y_{CO_2} and Y_{H_2}, it can clearly be noticed that their maximum mass fractions are just upstream the reacting zone. This is due to the absence of a catalyst along the recycling walls. For this reason, no chemical reactions occur at that region of the channel, as previously explained. As soon as the reactants cross the reacting zone and interact with the catalyst at the upper and lower walls, the methanol synthesis reactions commence. As a consequence, the consumption of these reactants starts as they begin transforming into their corresponding products. Since only surface reactions are modelled, the greatest consumption of the reactants is at the catalytic walls and thus, their lowest mass fractions. At this stage, the reactants' boundary layers form at the onset of the reacting zone. The width of these boundary layers keeps on increasing as the fluid mixture progresses along the streamwise direction, until reaching its maximum at the reactor's outlet. A negative mass fraction gradient is exhibited from the middle of the duct towards each of the two walls along the entire length of the reactive zone. This gradient triggers the molecular diffusion of species from regions of high concentration to regions of lower concentration. As a result, reactants, at more central widths, are driven towards the catalytic walls and the reactions are enhanced. In reality, unreacted reactants, *i.e.* these discharged at the outlet, are recycled and introduced again at the inlet section.

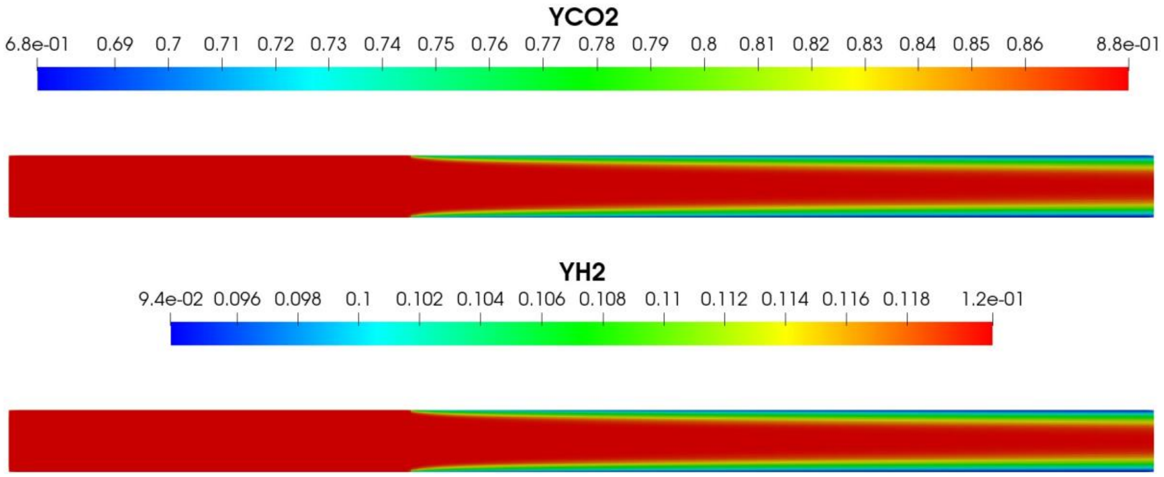

Figure 17. Boundary layer trends of the reactants, CO_2 (top) and H_2 (bottom), along the methanol reactor at T_w=200°C and *Re*=550.

The behaviour of the products' boundary layers (Figure 18) is exactly inversely correlated to that of the reactants. Unlike in the reactants' boundary layers, where a decreasing mass fraction trend is displayed along the length of the reacting zone, the products' boundary layers exhibit an increasing mass fraction trend, indicating the formation of new species. Moreover, the mass fraction gradients from the middle of the channel towards both walls of the reacting zone, are positive in this case.

Once the reactants enter the reacting zone and get in-touch with the catalyst coated on the upper and lower walls, the instantaneous diffusion of the reactants into the catalyst leads to the instantaneous formation of CH_3OH and the other by-products, *i.e.* CO and H_2O, at these walls. The primary and secondary methanol by-products, CO and H_2O, respectively, result from the RWGS reaction (Eq. 12). Similar to the cases of temperature and reactants, the products boundary layers form at the beginning of the reacting zone and continue to develop until reaching the outlet section of the reactor. In this particular context, the positive mass fraction gradients trigger a mass diffusion along the channel's width, from the walls to the central regions. This mass diffusion enhances the synthesis as it increases the methanol yield. It should be noted that in this thesis, methanol produced from CO hydrogenation is also taken into account (Eq. 10). Therefore, Y_{CO} at the outlet is considered as an unreacted reactant, which is recycled and sent back to the inlet, in real industrial settings.

Due to the unity Lewis number assumption, the rates of molecular and heat diffusion in this system are identical (Eq. 9). This has led to indistinguishable behaviours between the temperature and the chemical species' boundary layers.

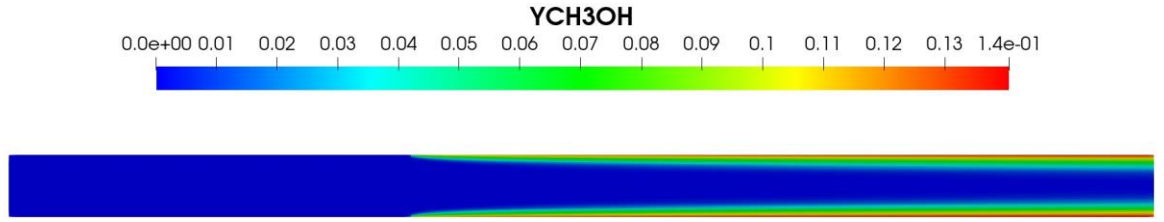

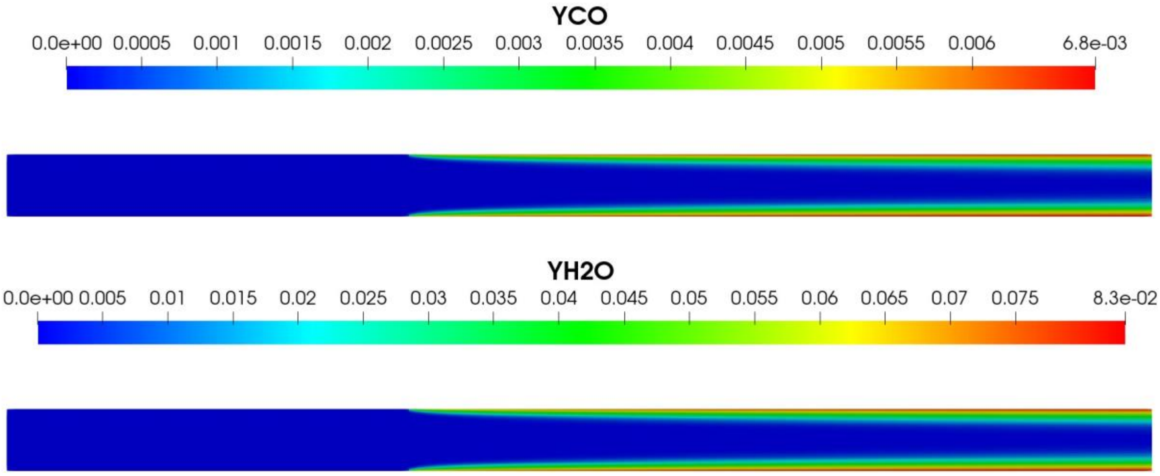

Figure 18. Boundary layer trends of the products, CH_3OH (top), CO (middle) and H_2O (bottom), along the methanol reactor at T_w=200°C and *Re*=550.

At this stage, the results of the different simulations are systematically compared. Simulating at the functional temperature range of the catalyst (200-250°C), the profiles of the temperature and all chemical species concentrations are displayed, along wall-normal direction of the reactor's outlet. Starting from T_w=200°C and progressing towards T_w=250°C using 10°C steps, these profiles are plotted at *Re*=100, *Re*=200, *Re*=550 and *Re*=1100, for each of the above-mentioned temperatures.

Starting with the temperature field, the effect of *Re* on the thermal boundary layer is identical in all of the performed simulations, regardless of the temperature imposed on the catalytic walls (Figure 19). The higher the *Re*, the lower the temperature profile recorded along the outlet of the channel. This is mainly attributed to the heat transfer residence time, *i.e.* the time available for heat transfer and diffusion to occur. The highest residence time is present when the fluid is flowing at its lowest bulk velocity (*Re*=100). As *Re* increases, the residence time decreases, which translates into a lower amount of time for heat diffusion to occur within the system.

When the reactive species mixture travels at the two lowest bulk velocities (*Re*=100 and *Re*=200), their corresponding wall-normal temperature distributions over the outlet section show that the entire width of the channel is influenced by the wall heat transfer, in both cases. In alternative phrasing, all fluid layers along the cross-section of the reactor's outlet are affected by the heat exchange. This can be deduced from the temperature differences between the fluid and the catalytic walls. Indeed, even at the farthest positions from the walls, *i.e.* around the middle of the channel, the temperature difference with respect to the walls is less than 20°C, for both *Re* values. This is more apparent when *Re*=100 as the greater residence time has led to a more effective heat transfer.

On the other hand, elaborating on the findings of *Re*=550 and *Re*=1100, it is evident that their temperature boundary layers feature lower widths, as compared to *Re*=100 and *Re*=200. Moreover, for both *Re* values, the wall heat transfer does not impact the full width of the channel, with free-stream regions observed around the center. This indicates that such relatively fast flow conditions don't allow for an effective heat exchange to take place. Nevertheless, having a greater time for heat diffusion to occur, the temperature profile exhibited at *Re*=550 is higher than that of *Re*=1100. All in all, in each of the simulated cases, *Re* dictates the temperature trend along the width of the channel, regardless of the temperature imposed on the catalytic walls.

It is significant to highlight that the thermal diffusivity of the system is assumed to be constant over this narrow temperature range (200-250°C). Therefore, at each specific *Re*, increasing T_w while maintaining a finite temperature difference (20°C) with the fluid, the only alteration in the curves' behaviors is an upward shift.

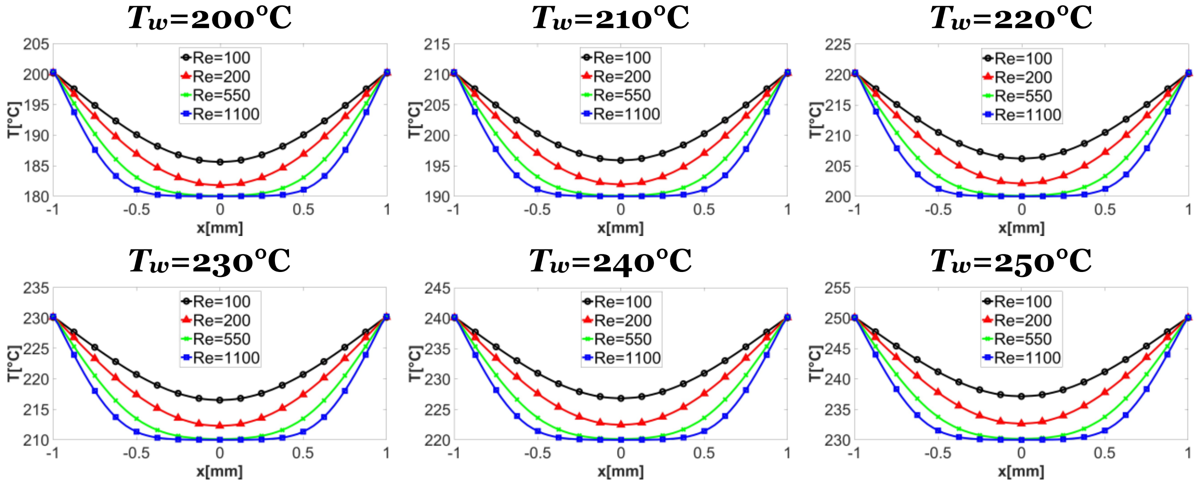

Figure 19. The instantaneous temperature boundary layers along the wall-normal direction of the reactor's outlet for the catalytic-wall temperature range 200-250°C, at *Re*=100, *Re*=200, *Re*=550 and *Re*=1100.

In relation to the chemical species involved in the catalytic methanol synthesis, a similar analogy could be applied with respect to the temperature field. When the mixture flows at low *Re*, an increased time would be available for the reactants to engage with the catalytic material and transform into products. Additionally, a greater period of time would be available for the diffusion phenomena and mixing to occur in-between the catalytic walls and the central regions of the channel. This time is known as the reaction residence time. Hence, as *Re* decreases, the residence time increases, as in the heat transfer case. This increase in the residence time leads to a more effective diffusion-mediated mixing between the species present in the channel, which enhances the methanol reactions.

As a result**,** regardless of the temperature imposed at the catalytic walls, *Re*=100 leads to the highest mass fractions of reacted reactants, *i.e.* lowest profiles of Y_{CO_2} and Y_{H_2}. On the other hand, due to having the lowest reaction residence time at *Re*=1100, the highest mass fraction profiles of the reactants are recorded, indicating the highest concentration of unreacted reactants (Figure 20). Moreover, as for the thermal boundary layers' discussion (Figure 19), reactants along the entire width of the outlet are exposed to chemical reactions at *Re*=100 and *Re*=200, while for *Re*=550 and *Re*=1100, a free-stream region is observed in the central regions of the channel. This is deduced by comparing the reactants' mass fractions around the middle of the outlet cross-section to their composition at the inlet section, for all the examined *Re*. Accordingly, for *Re*=100 and *Re*=200, $Y_{CO_2}<0.88$ and $Y_{H_2}<0.12$ at any point along the outlet, while for *Re*=550 and *Re*=1100, Y_{CO_2} and Y_{H_2} are equal to 0.88 and 0.12, respectively, around the middle. This confirms that the central region of the channel is not involved in the synthesis when the mixture flows at *Re*=550 and *Re*=1100.

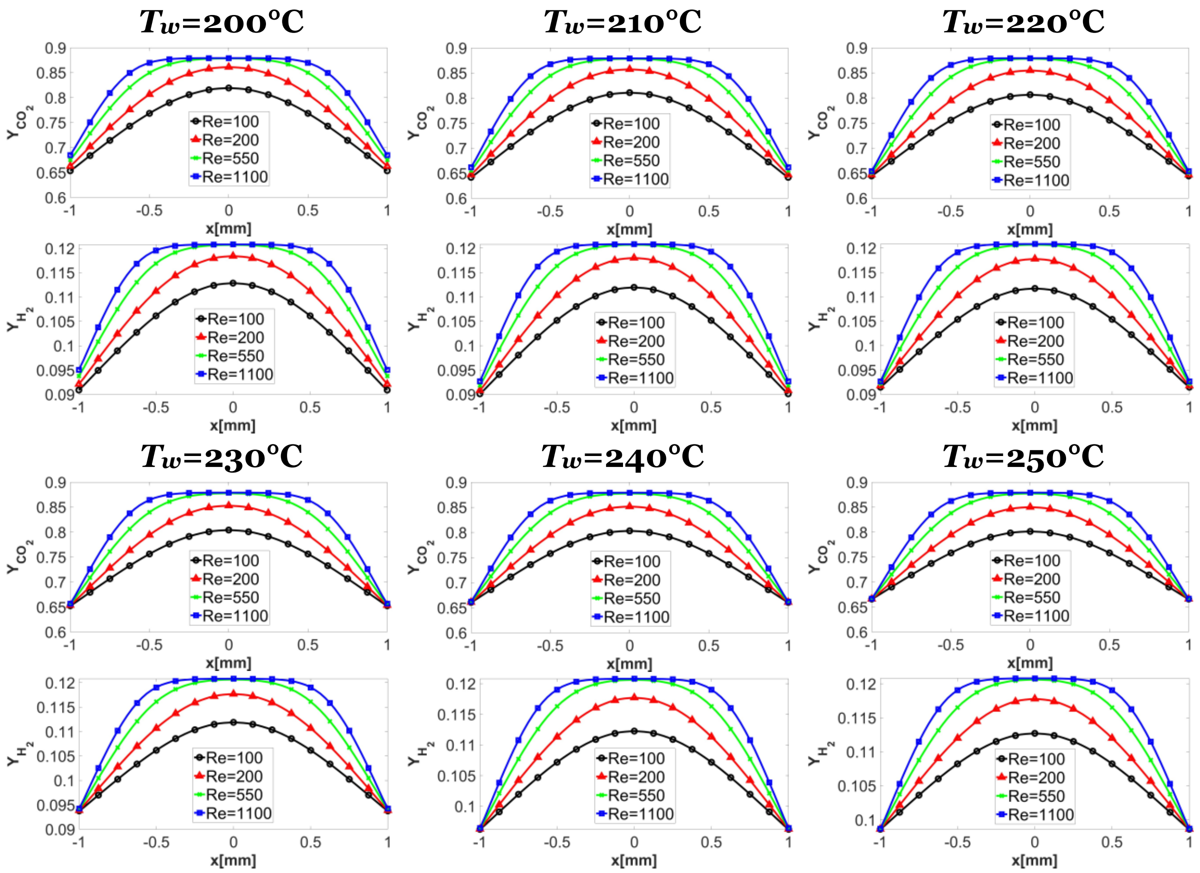

Figure 20. The reactants' (CO_2 and H_2) instantaneous boundary layers along the wall-normal direction of the reactor's outlet for the catalytic-wall temperature range 200-250°C, at *Re*=100, *Re*=200, *Re*=550 and *Re*=1100.

The products' profiles at the outlet section of the reactor are inversely correlated to these of the reactants. More specifically, the decrease in the concentration of the reactants is translated into an increase in products. Therefore, for all simulation temperatures, the conversion of reactants into products is enhanced as *Re* decreases, which causes an increase in the yielded products' mass fractions (Figure 21, Figure 22). This is a direct consequence of having a higher residence time, which results in a more effective diffusion-mediated mixing. Correspondingly, as expected, a product yield is found over the full spanwise dimension of the channel when the mixture flows at the two lowest bulk velocities, *i.e. Re*=100 and *Re*=200. On the contrary, the intermediate part of the channel remains undisturbed for *Re*=550 and *Re*=1100, indicating insufficient time for proper diffusion to take place among the present species.

However, the temperature conditions in the catalytic channel significantly influence the type of products obtained. In a thermodynamic context, methanol synthesis favours low temperatures [69]. Yet, operating at reduced temperatures hinders the activity of the catalyst. On the other hand, working at elevated temperatures favours the RWGS reaction. This arises from the endothermic nature of such a reaction (Eq. 12). Hence, due to the above-mentioned considerations, the aim is to determine the temperature range that ensures the best compromise and hence, the greatest methanol yield.

Referring to Figure 21**,** it is quite evident that the highest methanol yield is obtained for a catalytic wall temperature ranging in-between 200°C and 220°C. From this point onwards, the successive increase of temperature by 10°C steps, until reaching 250°C, keeps on diminishing the yielded Y_{CH_3OH}. On the other hand, concerning the RWGS products, *e.g*. CO, starting from 200°C, the higher the temperature imposed on the catalytic walls, the higher the produced Y_{CO} (Figure 22). Consequently, the maximum CO profile is attained at 250°C.

In conclusion, the thermo-fluid dynamic conditions yielding the highest methanol concentrations are *Re*=100 and 200°C ≤ T_w ≤ 220°C. In the following sections, the methanol yield and performance of the reactor are quantified.

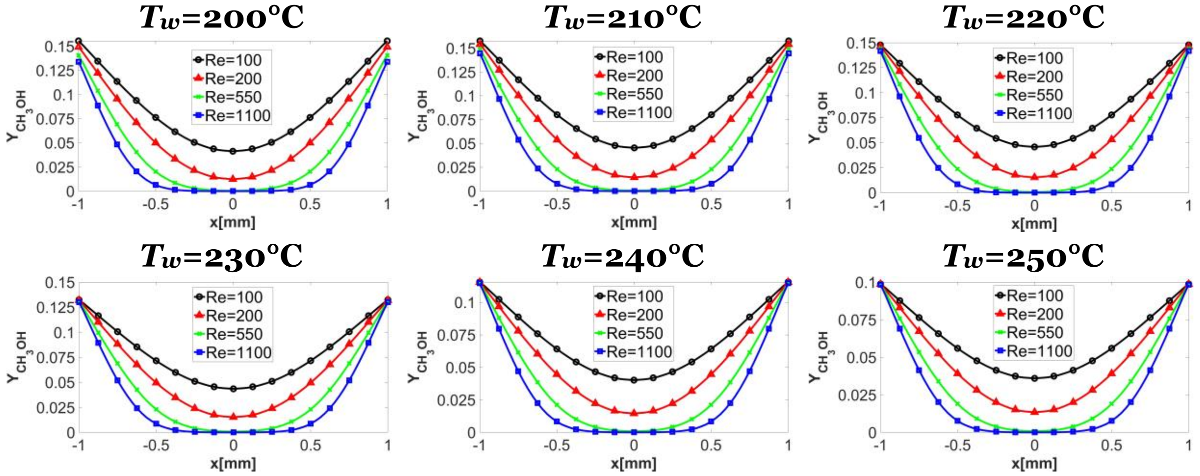

Figure 21. Instantaneous methanol boundary layers along the wall-normal direction of the reactor's outlet for the catalytic-wall temperature range 200-250°C, at *Re*=100, *Re*=200, *Re*=550 and *Re*=1100.

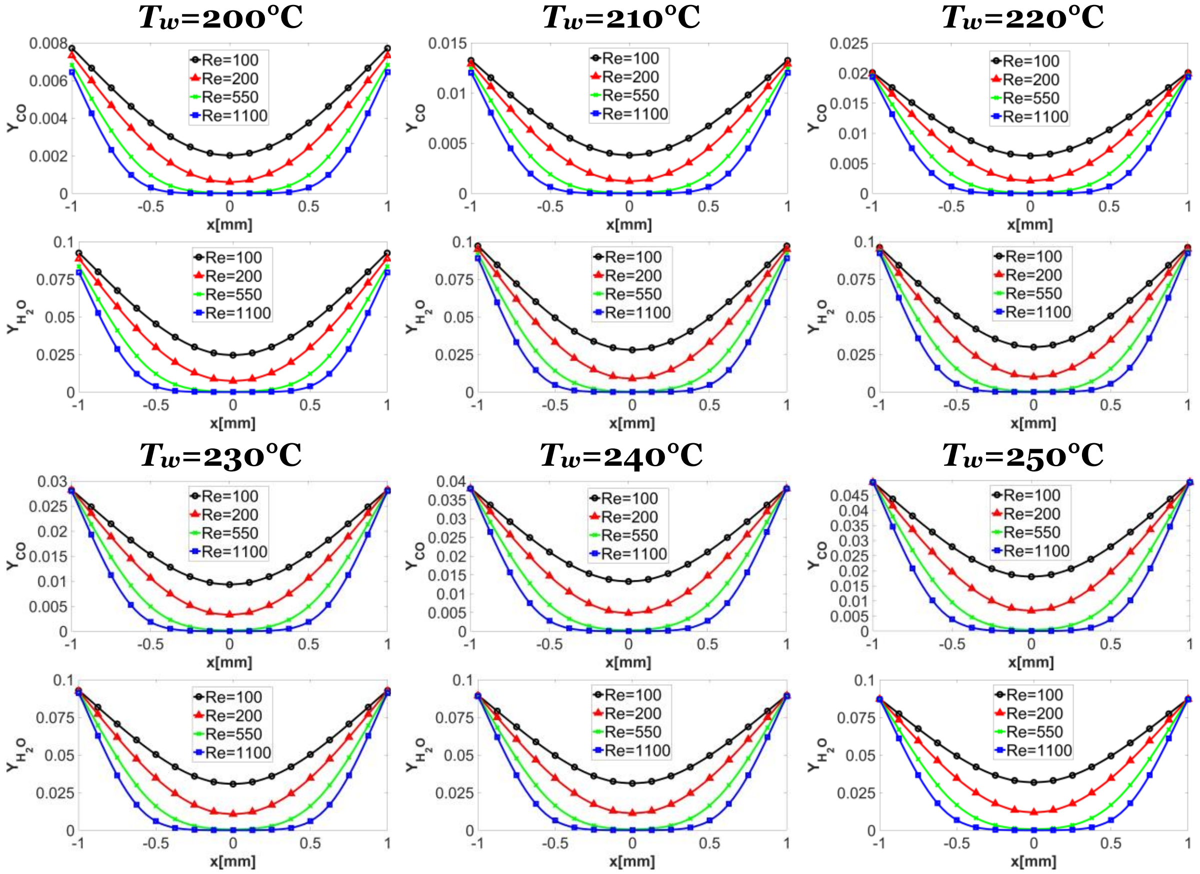

Figure 22. The instantaneous boundary layers of methanol's by-products (CO and H_2O) along the wall-normal direction of the reactor's outlet for the catalytic-wall temperature range 200-250°C, at *Re*=100, *Re*=200, *Re*=550 and *Re*=1100.

4.1.2 Averaged mass fractions at the reactor's outlet

Here, a quantitative analysis of the channel catalytic methanol synthesis is provided. For this purpose, two predefined post-processing utilities in OpenFOAM, *i.e.* patchFlowRate and patchAverage, are utilized at the reactor's outlet section. The former calculates the total flow rate discharged from the reactor by summing the individual flow rates at every face of the outlet section. On the other hand, the latter computes the spatial average of a specified field along the cross-section of the outlet. This spatial averaging technique is executed by taking the value of a certain field at every cell of the channel's outlet and weighing it by the cell volume. For instance, with a mesh grading factor of 12.5 between the channel's central axis and the walls, central cells contribute significantly more (12.5 times) to the spatial average than these near the walls. In the adopted 2D model, the weighing is done with respect to the cell area. Moreover, at the discharge of the channel, time-averaging is also applied. To elaborate further, at each cell belonging to the outlet section, the average value of the field over all the simulation timesteps is determined. Indeed, the spatial average is computed for each time-averaged chemical species' mass fraction. This term is known as spatiotemporal average.

First, an estimation of the yielded methanol mass flow rate at the outlet ($\dot{m}_{CH_3OH,o}$) is presented for each case of the parameter sweep. An approximation that guarantees a commendable level of accuracy can be provided as

$$\dot{m}_{CH_3OH,o} \cong \dot{m}_o \times Y_{CH_3OH,o}, \tag{21}$$

where $\dot{m}_o$ is the total mass flow rate discharged from the reactor and $Y_{\mathrm{CH_3OH,o}}$ is the spatiotemporal average of the methanol mass fraction at the outlet section. As would be expected for a compressible flow at a constant pressure, as T increases, ρ decreases. Thus, lower values of $\dot{m}_o$ are recorded at higher T (Table 11).

Table 11. Computation of the total mass flow rates discharged from the reactor for the catalytic-wall temperature range 200-250°C, at *Re*=100, *Re*=200, *Re*=550 and *Re*=1100.

	***Re*=100**	***Re*=200**	***Re*=550**	***Re*=1100**
$\dot{m}_{o,200°C}$ **[kg/s]**	9.896e-6	1.979e-5	5.441e-5	0.000109
$\dot{m}_{o,210°C}$ **[kg/s]**	9.682e-6	1.936e-5	5.325e-5	0.000106
$\dot{m}_{o,220°C}$ **[kg/s]**	9.477e-6	1.895e-5	5.212e-5	0.000104
$\dot{m}_{o,230°C}$ **[kg/s]**	9.283e-6	1.856e-5	5.103e-5	0.000102
$\dot{m}_{o,240°C}$ **[kg/s]**	9.093e-6	1.819e-5	5.001e-5	0.0001
$\dot{m}_{o,250°C}$ **[kg/s]**	8.912e-6	1.782e-5	4.9e-5	9.803e-5

Based on the analysis conducted in section 4.1.1, in accordance with expectations, the lower the *Re*, the greater $Y_{\mathrm{CH_3OH,o}}$. Among all simulations, the highest $Y_{\mathrm{CH_3OH,o}}$ corresponds to the case in which *Re*=100 and T_w=210°C (Table 12). The data recorded in Table 12 are plotted (Figure 23).

Table 12. Computation of the spatiotemporal averages of the methanol mass fractions yielded at the outlet of the reactor, for the catalytic-wall temperature range 200-250°C, at *Re*=100, *Re*=200, *Re*=550 and *Re*=1100.

	***Re*=100**	***Re*=200**	***Re*=550**	***Re*=1100**
$Y_{\mathrm{CH_3OH,o,200°C}}$	0.0830	0.0615	0.0409	0.031
$Y_{\mathrm{CH_3OH,o,210°C}}$	**0.0864**	0.0647	0.0437	0.0334
$Y_{\mathrm{CH_3OH,o,220°C}}$	0.0833	0.0631	0.0433	0.0335
$Y_{\mathrm{CH_3OH,o,230°C}}$	0.0764	0.0584	0.0406	0.0318
$Y_{\mathrm{CH_3OH,o,240°C}}$	0.0685	0.0519	0.0368	0.0291
$Y_{\mathrm{CH_3OH,o,250°C}}$	0.0602	0.0461	0.0327	0.0261

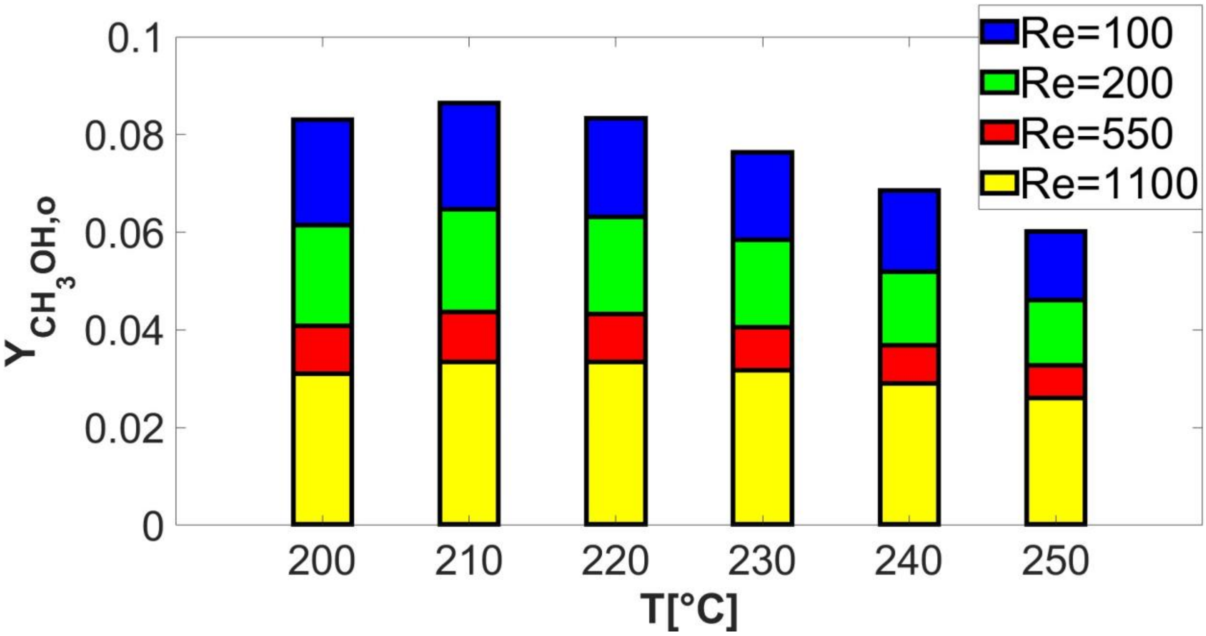

Figure 23. Bar graph showing a summary of the spatiotemporal averages of the methanol mass fractions yielded at the outlet of the reactor, for the catalytic-wall temperature range 200-250°C, at *Re*=100, *Re*=200, *Re*=550 and *Re*=1100.

For all *Re*, the greatest methanol production rates are observed at T_w=210°C (Table 13). Apparently, this represents the most optimal temperature condition for methanol formation. Comparing the yielded methanol mass flow rates at different *Re*, it is anticipated to have greater values at higher *Re* due to the higher total mass flow rate, *i.e.* greater amount of species introduced in the channel. However, a greater $\dot{m}_{\mathrm{CH_3OH,o}}$ does not necessarily imply a better reactor performance. The effectiveness and efficiency of the reactor in converting the reactants into methanol is investigated in section 4.1.3.

Table 13. Computation of the spatiotemporal averages of the methanol mass flow rates produced by the reactor, for the catalytic-wall temperature range 200-250°C, at *Re*=100, *Re*=200, *Re*=550 and *Re*=1100.

$\dot{m}_{CH_3OH,o}$**[kg/s]**	***Re*=100**	***Re*=200**	***Re*=550**	***Re*=1100**
$\dot{m}_{CH_3OH,o,200°C}$	8.21e-07	1.22e-06	2.23e-06	3.38e-06
$\dot{m}_{CH_3OH,o,210°C}$	**8.37e-07**	**1.25e-06**	**2.33e-06**	**3.54e-06**
$\dot{m}_{CH_3OH,o,220°C}$	7.89e-07	1.20e-06	2.26e-06	3.48e-06
$\dot{m}_{CH_3OH,o,230°C}$	7.09e-07	1.08e-06	2.07e-06	3.24e-06
$\dot{m}_{CH_3OH,o,240°C}$	6.23e-07	9.44e-07	1.84e-06	2.91e-06
$\dot{m}_{CH_3OH,o,250°C}$	5.37e-07	8.22e-07	1.60e-06	2.56e-06

Concerning the reactants, as *Re* decreases, the greater reaction residence time expectedly leads to a decrease in both, $Y_{CO_2,o}$ and $Y_{H_2,o}$ (Table 14). However, both averaged mass fractions exhibit a non-monotonic relation with temperature, in general. At higher temperatures, although the catalyst activity increases, the two reactions yielding methanol (Eqs. 9 and 10) become less favoured, from a thermodynamic point of view. On the contrary, such temperature conditions enhance the endothermic RWGS reaction (Eq.12). These are the major causes to such a fluctuating trend. Although the reactants, in all the examined cases, achieve their minimum averaged mass fractions at T_w=220°C, the most optimal temperature for the catalytic synthesis of methanol remains T_w=210°C as it consistently results in the highest produced methanol mass flux (Table 13). The averaged mass fractions of CO_2 and H_2 at the outlet of the channel are plotted in Figure 24.

Table 14. Computation of the spatiotemporal averages of the mass fractions of CO_2 (top) and H_2 (bottom) at the outlet of the reactor, for the catalytic-wall temperature range 200-250°C, at *Re*=100, *Re*=200, *Re*=550 and *Re*=1100.

	***Re*=100**	***Re*=200**	***Re*=550**	***Re*=1100**
$Y_{CO_2,o,200°C}$	0.756	0.786	0.816	0.83
$Y_{CO_2,o,210°C}$	0.746	0.778	0.809	0.825
$Y_{CO_2,o,220°C}$	0.744	0.776	0.807	0.822
$Y_{CO_2,o,230°C}$	0.746	0.777	0.807	0.822
$Y_{CO_2,o,240°C}$	0.748	0.781	0.807	0.822
$Y_{CO_2,o,250°C}$	0.749	0.779	0.808	0.822

	***Re*=100**	***Re*=200**	***Re*=550**	***Re*=1100**
$Y_{H_2,o,200°C}$	0.105	0.109	0.113	0.115
$Y_{H_2,o,210°C}$	0.104	0.108	0.112	0.114
$Y_{H_2,o,220°C}$	0.104	0.108	0.112	0.114
$Y_{H_2,o,230°C}$	0.105	0.109	0.113	0.114
$Y_{H_2,o,240°C}$	0.106	0.11	0.113	0.115
$Y_{H_2,o,250°C}$	0.108	0.111	0.114	0.115

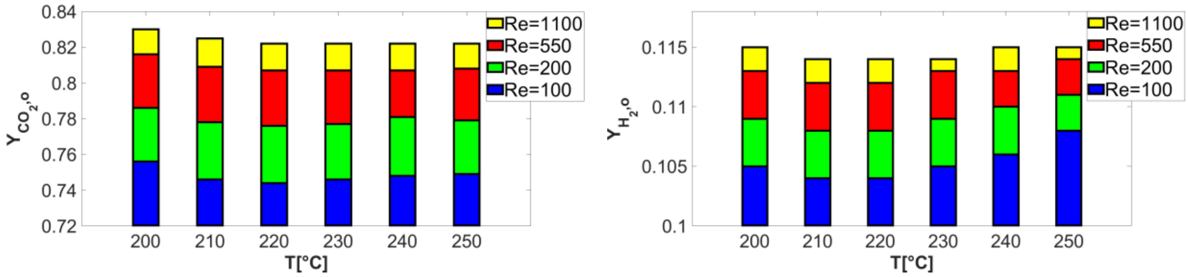

Figure 24. Bar graphs showing a summary of the spatiotemporal averages of the unreacted mass fractions of CO_2 (left) and H_2 (right) at the outlet of the reactor, for the catalytic-wall temperature range 200-250°C, at *Re*=100, *Re*=200, *Re*=550 and *Re*=1100.

Regarding the primary by-product of methanol (CO), the results of Table 15 clearly demonstrate the direct proportionality between $Y_{CO,o}$ and both, the decrease in *Re* and the increase in the catalytic wall temperature. The overall enhancement of the reactions at T_w=220°C, with respect to T_w=210°C, results in an increased concentration of CO, albeit at the cost of a diminished $\dot{m}_{CH_3OH,o}$. As a result, a temperature setting of 220°C at the catalytic walls is deemed less advantageous in comparison to 210°C. The tabulated values of $Y_{CO,o}$ are presented in a bar graph shown in Figure 25.

Table 15. Computation of the spatiotemporal averages of the CO mass fractions yielded at the outlet of the reactor, for the catalytic-wall temperature range 200-250°C, at *Re*=100, *Re*=200, *Re*=550 and *Re*=1100.

	***Re*=100**	***Re*=200**	***Re*=550**	***Re*=1100**
$Y_{CO,o,200°C}$	0.00574	0.00493	0.00433	0.0041
$Y_{CO,o,210°C}$	0.00877	0.0072	0.00581	0.00519
$Y_{CO,o,220°C}$	0.0127	0.0102	0.00781	0.0067
$Y_{CO,o,230°C}$	0.0174	0.0138	0.0103	0.00854
$Y_{CO,o,240°C}$	0.0233	0.0171	0.0132	0.0107
$Y_{CO,o,250°C}$	0.03	0.0233	0.0166	0.0133

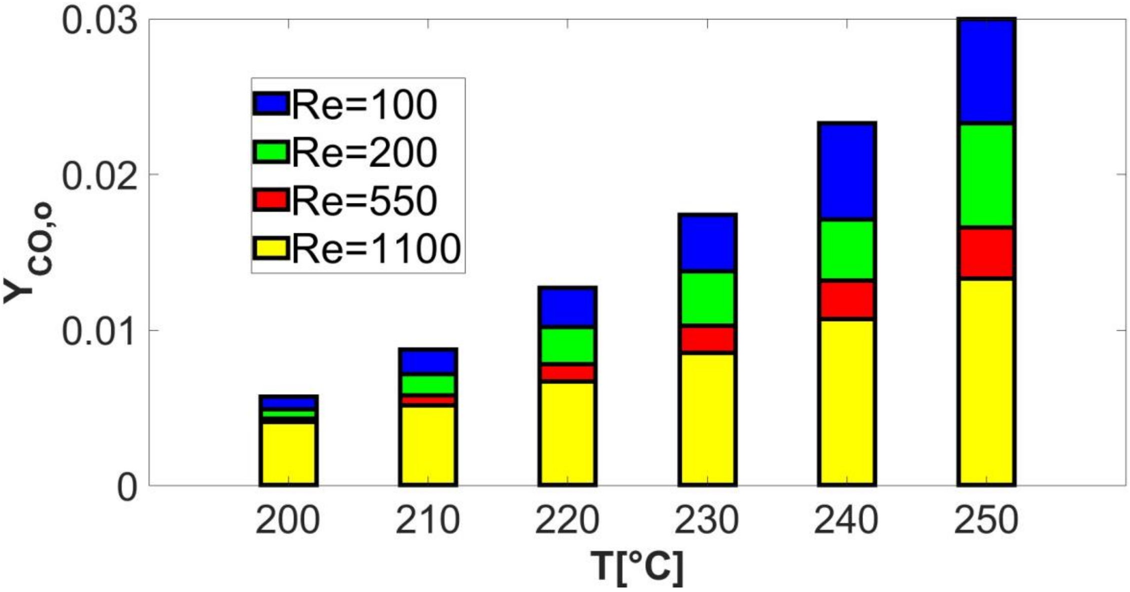

Figure 25. Bar graph showing a summary of the spatiotemporal averages of the CO mass fractions yielded at the outlet of the reactor, for the catalytic-wall temperature range 200-250°C, at *Re*=100, *Re*=200, *Re*=550 and *Re*=1100.

4.1.3 Conversion efficiency analysis

In order to assess the performance of the present channel-type methanol reactor, its conversion efficiency is evaluated in each of the investigated scenarios. The efficiency serves as a quantitative measure of the reactor's effectiveness, *i.e.* its ability to convert the reactants flowing through its catalyst-coated channel into products, in particular, methanol. The two parameters representative of the reactor's conversion efficiency are the CO_2 conversion ($\mathbf{X}_{\mathbf{CO_2}}$) and the methanol yield ($\mathbf{Y}_{\mathbf{CH_3OH}}$) [55]. It is important to note that $\mathbf{Y}_{\mathbf{CH_3OH}}$ is not the same as $Y_{\mathrm{CH_3OH}}$, which stands for the methanol mass fraction.

By definition, $\mathbf{X}_{\mathbf{CO_2}}$ is expressed as

$$\mathbf{X}_{\mathbf{CO_2}} = \frac{Y_{\mathrm{CO_2,i}} - Y_{\mathrm{CO_2,o}}}{Y_{\mathrm{CO_2,i}}}\,, \tag{22}$$

where $Y_{\mathrm{CO_2,i}}$ is the CO_2 mass fraction initialized at the inlet of the reactor (0.88). The values presented in Table 14 are utilized for $Y_{\mathrm{CO_2,o}}$. This parameter represents the proportion of CO_2 that undergoes a reaction, out of the total amount introduced at the inlet.

On the other hand, $\mathbf{Y}_{\mathbf{CH_3OH}}$ is characterized by the formula

$$\mathbf{Y}_{\mathbf{CH_3OH}} = \frac{Y_{\mathrm{CH_3OH,o}} MW_{\mathrm{CO_2}}}{Y_{\mathrm{CO_2,i}} MW_{\mathrm{CH_3OH}}}\,, \tag{23}$$

where $MW_{\mathrm{CO_2}}$ and $MW_{\mathrm{CH_3OH}}$ are the molecular weights of CO_2 (44.01 g/mol) and CH_3OH (32.04 g/mol), respectively. In Table 12, $Y_{\mathrm{CH_3OH,o}}$ is calculated for each of the conducted simulations. Coupling Eq. (23) with the chemical identity $n = \frac{m}{MW}$, $\mathbf{Y}_{\mathbf{CH_3OH}}$ can be reasonably approximated as

$$\mathbf{Y}_{\mathbf{CH_3OH}} \cong \frac{n_{\mathrm{CH_3OH,o}}}{n_{\mathrm{CO_2,i}}}\,, \tag{24}$$

where $n_{\mathrm{CH_3OH,o}}$ is the produced number of moles of methanol at the outlet section and $n_{\mathrm{CO_2,i}}$ is the introduced number of moles of CO_2 at the channel's inlet. Thus, $\mathbf{Y}_{\mathbf{CH_3OH}}$ reflects the proportion of CO_2 that undergoes conversion into methanol during the synthesis process.

Referring to Table 16, it is evident that $\mathbf{X}_{\mathbf{CO_2}}$ enhances with the decrease in the mixture's bulk flow velocity (*Re*). The observed outcome is a consequence of the extended reaction residence time in such instances, which augments the chemical reactions by enhancing the mass transfer-driven mixing between the species. Concerning the influence of the catalytic wall temperature, the observed findings are equivalent to these of the averaged reactants' mass fractions in section 4.1.2. Indeed, the relation is highly non-monotonic between T and $\mathbf{X}_{\mathbf{CO_2}}$. In addition, for every *Re*, the maximum $\mathbf{X}_{\mathbf{CO_2}}$ is recorded in the case in which $Y_{\mathrm{CO_2,o}}$ attains its minimum value, *i.e.* at T_w=220°C. In Figure 26, the obtained $\mathbf{X}_{\mathbf{CO_2}}$ values for the different simulated scenarios are illustrated in a bar chart. However, exhibiting a greater CO_2 conversion doesn't necessarily imply a better performance. As discussed earlier, this improvement in the chemical reactions could lead to an increase in the RWGS products at the expense of methanol. Instead, the optimal performance is achieved when the highest quantity of CO_2 is transformed into CH_3OH. This aspect can be addressed by employing the second conversion efficiency parameter, *i.e.* $\mathbf{Y_{CH_3OH}}$.

Table 16. Computation of the CO_2 conversion parameter for the catalytic-wall temperature range 200-250°C, at *Re*=100, *Re*=200, *Re*=550 and *Re*=1100.

	***Re*=100**	***Re*=200**	***Re*=550**	***Re*=1100**
$X_{CO_2,200°C}$	14.09%	10.68%	7.27%	5.68%
$X_{CO_2,210°C}$	15.23%	11.59%	8.07%	6.25%
$X_{CO_2,220°C}$	15.45%	11.82%	8.30%	6.59%
$X_{CO_2,230°C}$	15.23%	11.70%	8.30%	6.59%
$X_{CO_2,240°C}$	15.00%	11.25%	8.30%	6.59%
$X_{CO_2,250°C}$	14.89%	11.48%	8.18%	6.59%

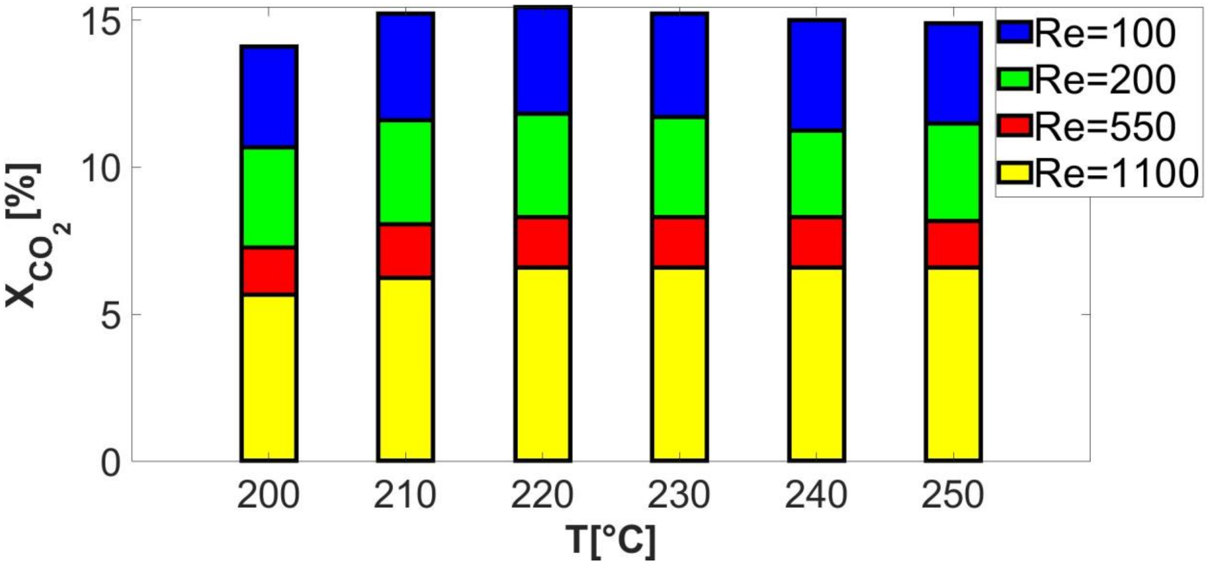

Figure 26. Bar graph showing a summary of the CO_2 conversion parameter values for the catalytic-wall temperature range 200-250°C, at *Re*=100, *Re*=200, *Re*=550 and *Re*=1100.

According to the conducted $\mathbf{Y_{CH_3OH}}$ computations (Table 17), the highest-efficiency performance of the channel-type methanol reactor is witnessed at *Re*=100 and T_w=210°C, in which $\mathbf{Y_{CH_3OH}}$=13.49% and $\mathbf{X_{CO_2}}$=15.23%. For *Re*=100, *Re*=200 and *Re*=550, the greatest methanol yield is recorded at T_w=210°C, although the CO_2 conversion is not the highest. This confirms that the overall reaction enhancement at higher temperatures yields an increased formation of methanol's by-products, albeit at the expense of a decrease in methanol production. This is mainly attributed to the presence of a thermal medium which is more suitable for the RWGS reactions as compared to the methanol hydrogenation ones, as elaborated in previous sections. The only exception to the above-mentioned findings is observed at *Re*=1100, where a marginally higher $\mathbf{Y_{CH_3OH}}$ is attained at T_w=220°C with respect to T_w=210°C. Nonetheless, a temperature setting of T_w=210°C is considered the most desirable for catalytic methanol synthesis under low-*Re*, laminar flow conditions. The bar graph in Figure 27 depicts the methanol yields obtained in each scenario examined during the parameter sweep.

Table 17. Computation of the methanol yield parameter for the catalytic-wall temperature range 200-250°C, at *Re*=100, *Re*=200, *Re*=550 and *Re*=1100.

	***Re*=100**	***Re*=200**	***Re*=550**	***Re*=1100**
$Y_{CH3OH,200^{\circ}C}$	12.96%	9.60%	6.38%	4.84%
$Y_{CH3OH,210^{\circ}C}$	13.49%	10.10%	6.82%	5.21%
$Y_{CH3OH,220^{\circ}C}$	13.00%	9.85%	6.76%	5.23%
$Y_{CH3OH,230^{\circ}C}$	11.93%	9.12%	6.34%	4.96%
$Y_{CH3OH,240^{\circ}C}$	10.69%	8.10%	5.74%	4.54%
$Y_{CH3OH,250^{\circ}C}$	9.40%	7.20%	5.10%	4.07%

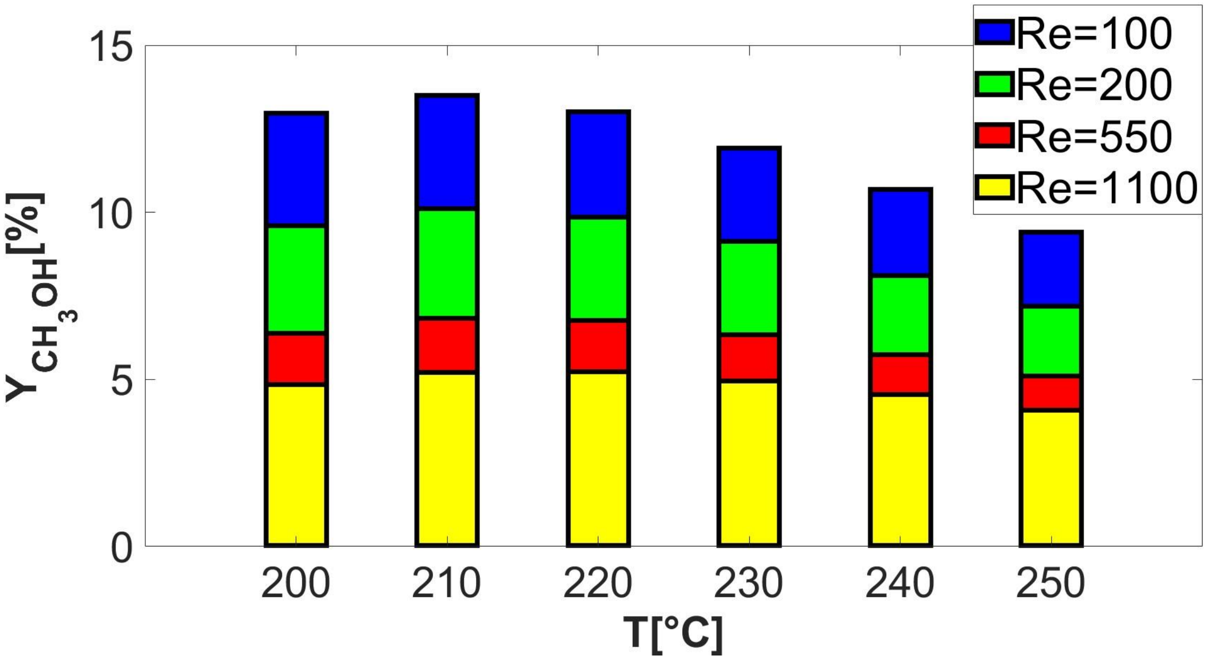

Figure 27. Bar graph showing a summary of the methanol yield parameter values for the catalytic-wall temperature range 200-250°C, at *Re*=100, *Re*=200, *Re*=550 and *Re*=1100.

These are the main results of the simulations of category (A). The temperature and *Re* yielding optimal reactor productivity have been determined. Next, the effect of elongating the reacting zone is studied.

4.2 Laminar simulations without flow recycling (Group (B))

Upon identifying the optimal temperature for methanol synthesis (210°C), where the process exhibits its highest efficiency and output, the impact of extending the length of the reacting zone is investigated. For this purpose, the recycling zone is excluded and the reacting zone is extended towards the inlet section. In alternative phrasing, the catalyst coating covers the entire length of channel's wall segments in these simulations, as depicted in Figure 4. Setting the wall temperature to 210°C, *i.e.* T_w=210°C, this fully-catalytic configuration is simulated at flows corresponding to *Re*=100, *Re*=200, *Re*=550 and *Re*=1100.

4.2.1 Instantaneous boundary layers and trends of different fields

Similar to what has been done for group (A) simulations, the temperature and chemical species trends over the whole 2D computational domain are presented. Furthermore, the instantaneous boundary layer profiles of the different fields are plotted along the width of the outlet section.

It has been demonstrated in section 4.1.1 that all reactants exhibit identical behaviors, which are inversely correlated with these of the products. Therefore, in addition to the temperature trend, only the mass fraction distributions of the main reactant and product, *i.e.* CO_2 and CH_3OH, respectively, are shown. This is done for the case in which the channel features a reactive mixture flowing at *Re*=200. Solely providing the above-mentioned trends is sufficient for thoroughly representing the phenomena occurring in the reactor.

In general, the physics involved in the channel is exactly the same as in group (A) simulations. The only difference in this case is that the boundary layers form just downstream of the inlet section, upon the impingement of the reactive species on the adjacent walls. Initiating at the inlet, the boundary layers pertaining to different fields have the entire length of the channel (37mm) to establish. On the contrary, in the simulation cases featuring flow recycling, the boundary layers start to form just after the interface separating the recycling and reactive zones, *i.e.* 13mm downstream of the inlet section. Accordingly, the boundary layers in the simulations categorized into group (B) have an extra 13mm to develop. As a consequence, a relatively greater boundary layer width is expected to be visualized near the channel's outlet section in these cases.

The channel's temperature trend is presented in Figure 28. As per the previous discussion, an enhanced heat transfer from the walls to the bulk regions is foreseen. Therefore, the temperature differences between the fluid and the upper and lower wall segments near the outlet section are expected to diminish relative to the equivalent group (A) case.

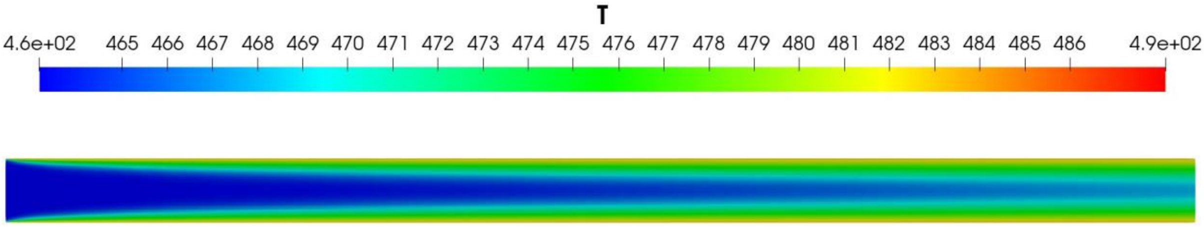

Figure 28. Distribution of the instantaneous temperature field along the whole methanol reactor at T_w=210°C and *Re*=200, when the catalyst coating is applied over the entire length of the walls.

Concerning the chemical species (Figure 29), analogous reasonings could be formulated. Therefore, an enhancement in methanol synthesis is anticipated. Indeed, the extended reacting zone allows for the molecular diffusion-based mixing between the reacted and unreacted species to occur over a greater length in the channel. Therefore, larger boundary layer widths are observed at the reactor's discharge. As a result, compared to the equivalent case featuring flow recycling (T_w=210°C and *Re*=200), it is expected to have a reduced CO_2 concentration at the outlet section, which implies an increased methanol yield.

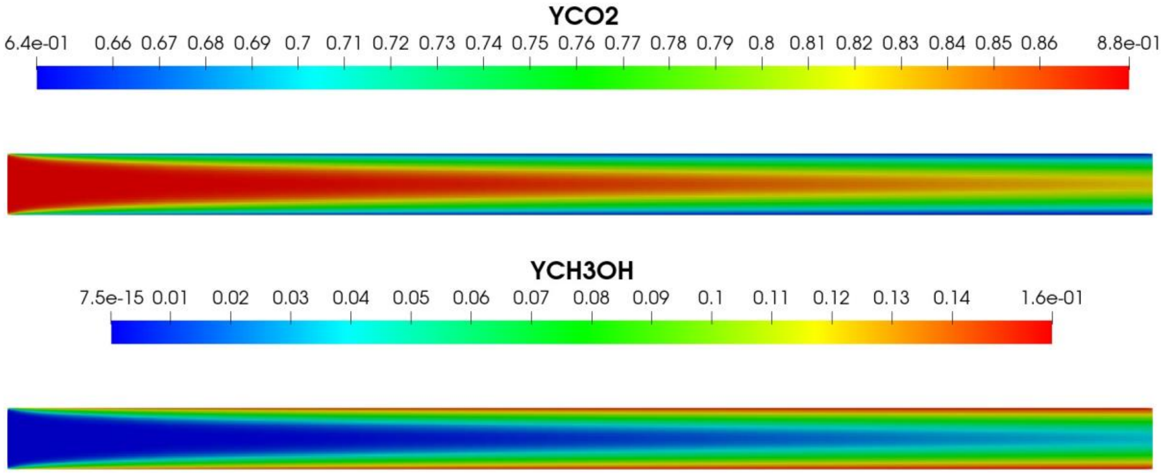

Figure 29. Distributions of the instantaneous mass fractions of CO_2 (top) and CH_3OH (bottom) along the whole methanol reactor at T_w=210°C and *Re*=200, when the catalyst coating is applied over the entire length of the walls.

Referring to the thermal boundary layers plotted at the outlet section (Figure 30), in general, equivalent findings to these of group (A) are observed. Indeed, as the *Re* decreases, the heat transfer residence time increases, leading to an enhanced heat diffusion and consequently, a higher temperature profile. However, the increase in the boundary layer widths, after the extension of the catalyst coating, is apparent. For instance, at *Re*=100 and *Re*=200, temperature differences between walls and center are reduced relative to the cases of group (A). Furthermore, at *Re*=550, the central region is no longer perfectly undisturbed, *i.e.* it experiences a temperature difference lower than 20°C with respect to the walls.

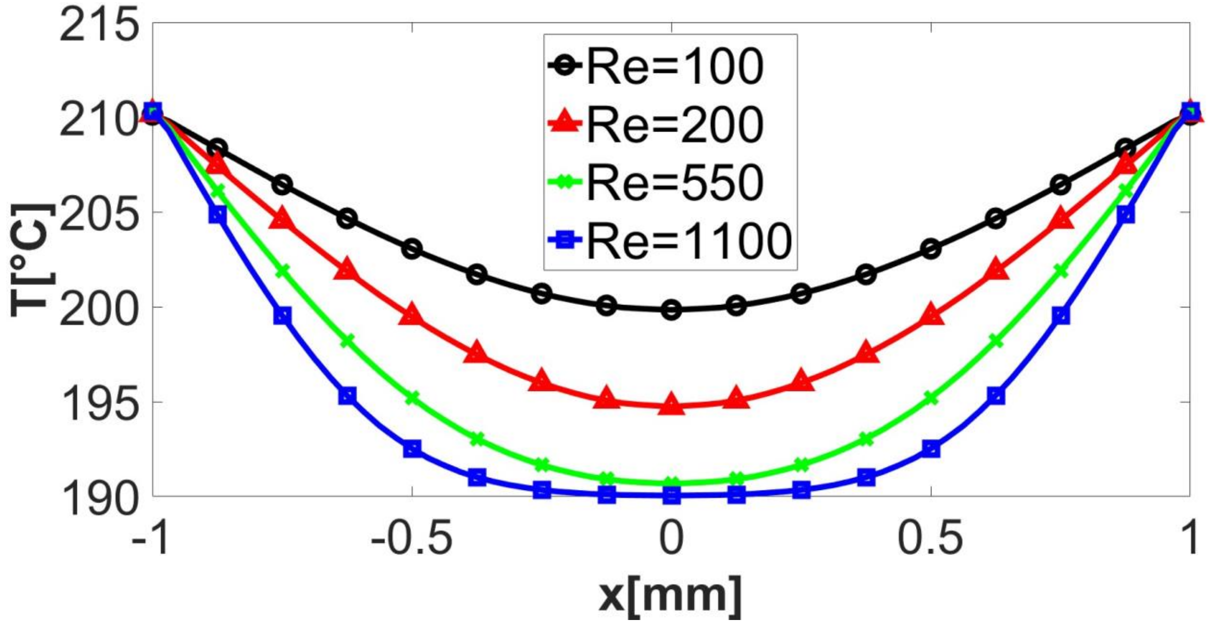

Figure 30. The instantaneous temperature boundary layers along the wall-normal direction of the reactor's outlet at T_w=210°C, for *Re*=100, *Re*=200, *Re*=550 and *Re*=1100, when the catalyst coating is applied over the entire length of the walls.

The effect of elongating the reacting zone on the reactants (Figure 31) and products (Figure 32) is equivalent to its effect on the temperature (Figure 30). Accordingly, lower reactants mass fractions and equivalently, increased products mass fractions are obtained around the middle of the channel, as compared to the previous simulations. Therefore, deploying a catalytic material over the entire length of the channel leads to an overall improvement in the synthesis.

All remaining observations pertaining to the general boundary layer trends are analogous with respect to group (A) simulations. For instance, the lower reaction residence time at higher *Re* hinders diffusion phenomena and mixing between the involved species. This results in higher concentrations of unreacted species and thereby, lower produced mass fractions. Conversely, at reduced bulk flow velocities, the reactive species benefit from an increased interaction time with the catalytic walls, leading to an augmentation in diffusion-mediated mixing. This yields higher products concentrations.

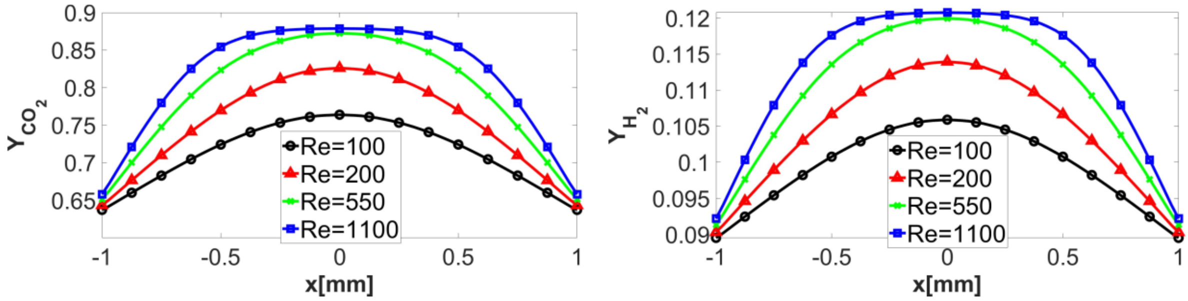

Figure 31. The instantaneous reactants boundary layers along the wall-normal direction of the reactor's outlet at T_w=210°C, for *Re*=100, *Re*=200, *Re*=550 and *Re*=1100, when the catalyst coating is applied over the entire length of the walls.

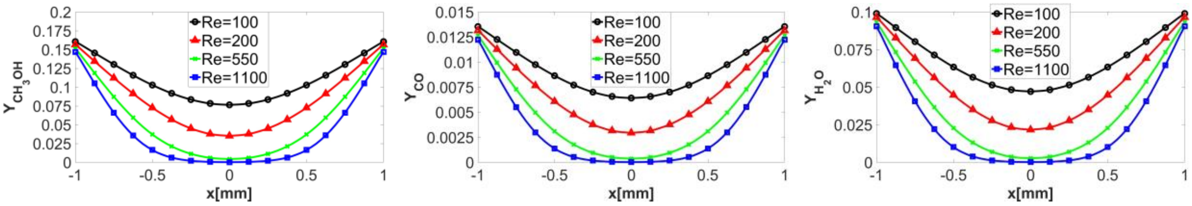

Figure 32. The instantaneous products boundary layers along the wall-normal direction of the reactor's outlet at T_w=210°C, for *Re*=100, *Re*=200, *Re*=550 and *Re*=1100, when the catalyst coating is applied over the entire length of the walls.

4.2.2 Averaged mass fractions at the reactor's outlet and conversion efficiency

First, the spatiotemporal averages of the methanol mass fractions at the outlet of the catalytic channel are calculated for *Re*=100, *Re*=200, *Re*=550 and *Re*=1100, at T_w=210°C. Afterwards, the corresponding produced methanol mass flow rates are determined. Moreover, a computation of the averaged mass fractions of CO_2 at the outlet section is carried out for each of the above-mentioned cases. Finally, utilizing the spatiotemporally-averaged mass fractions of CO_2 and CH_3OH, the conversion efficiency of the reactor in this fully-catalytic configuration is investigated.

The values of $Y_{CH_3OH,o}$ and $\dot{m}_{CH_3OH,o}$ obtained in the different simulation cases are provided in Table 18. In line with expectations, comparing the individual findings to these of group (A) simulations, an enhanced methanol production can be noted. Figure 33 displays the obtained methanol mass fractions at different *Re*.

Table 18. Computation of the spatiotemporal averages of the yielded methanol mass fractions and flow rates at the outlet of the reactor, at T_w=210°C, for *Re*=100, *Re*=200, *Re*=550 and *Re*=1100, when the catalyst coating is applied over the entire length of the walls.

	***Re*=100**	***Re*=200**	***Re*=550**	***Re*=1100**
$\mathbf{Y_{CH_3OH,o,210°C}}$	0.1	0.0738	0.0472	0.0345
$\dot{m}_{\mathbf{CH_3OH,o,210°C}}$**[kg/s]**	9.68e-07	1.43e-06	2.51e-06	3.66e-06

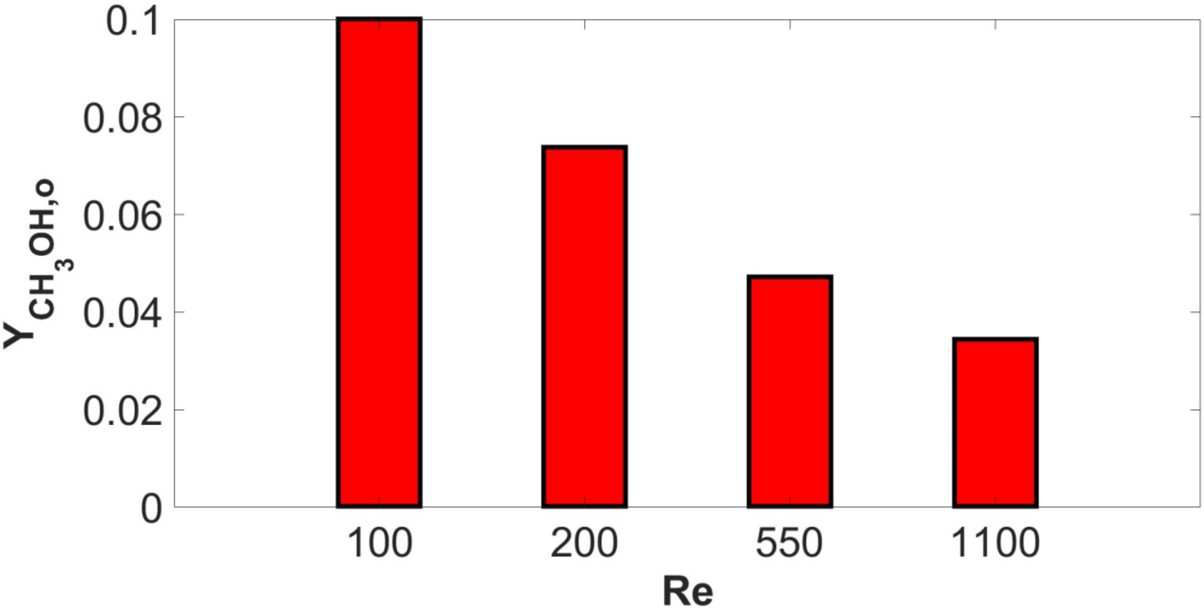

Figure 33. Bar graph showing a summary of the spatiotemporal averages of the methanol mass fractions yielded at the outlet of the reactor, at T_w=210°C, for *Re*=100, *Re*=200, *Re*=550 and *Re*=1100, when the catalyst coating is applied over the entire length of the walls.

In Table 19, the values of $Y_{CO_2,o}$ are presented at T_w=210°C, for *Re*=100, *Re*=200, *Re*=550 and *Re*=1100. As *Re* decreases, a greater mass fraction of CO_2 undergoes a chemical reaction, as explained earlier. Comparing the present CO_2 findings to these of group (A) under identical thermo-fluid dynamic conditions, it is evident that increasing the length of the reacting zone augments the reactions governing the methanol synthesis process. The tabulated values of CO_2 mass fractions are plotted in a bar graph (Figure 34).

Table 19. Computation of the spatiotemporal averages of the unreacted CO_2 mass fractions at the outlet of the reactor, at T_w=210°C, for *Re*=100, *Re*=200, *Re*=550 and *Re*=1100, when the catalyst coating is applied over the entire length of the walls.

	***Re*=100**	***Re*=200**	***Re*=550**	***Re*=1100**
$\mathbf{Y_{CO_2,o,210°C}}$	0.728	0.768	0.807	0.826

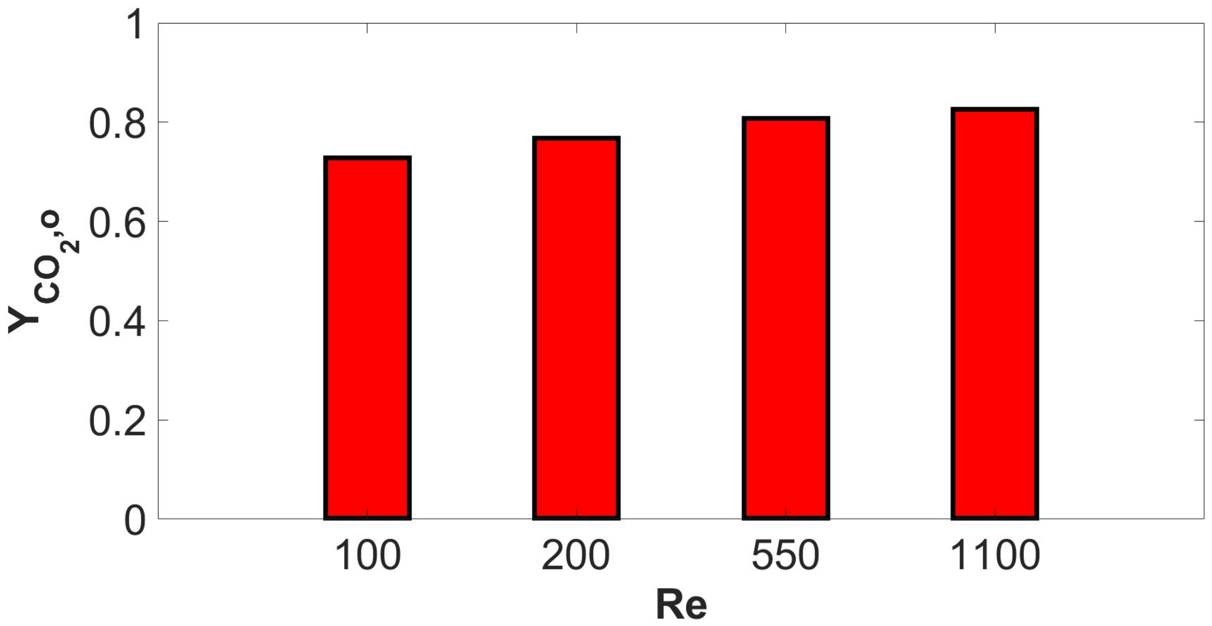

Figure 34. Bar graph showing a summary of the spatiotemporal averages of the unreacted CO_2 mass fractions at the outlet of the reactor, at T_w=210°C, for *Re*=100, *Re*=200, *Re*=550 and *Re*=1100, when the catalyst coating is applied over the entire length of the walls.

At this stage, the conversion efficiency of the reactor is addressed. This would highlight the benefits of increasing the length of the catalyst-coated zone on the overall reactor performance. By utilizing the previously determined values of $Y_{CO_2,o}$ and $Y_{CH_3OH,o}$, the computation of $\mathbf{Y_{CH_3OH}}$ and $\mathbf{X_{CO_2}}$ is performed for each of the examined cases (Table 20).

Apparently, the conversion efficiency increases with the decrease in *Re*. Moreover, group (B) simulations exhibit higher conversion efficiencies with respect to group (A). Therefore, adopting a fully-catalytic configuration enhances the performance of the reactor. The CO_2 conversion and the methanol yield parameters are plotted in Figure 35.

Table 20. Computation of the CO_2 conversion and methanol yield parameters at T_w=210°C, for *Re*=100, *Re*=200, *Re*=550 and *Re*=1100, when the catalyst coating is applied over the entire length of the walls.

	***Re*=100**	***Re*=200**	***Re*=550**	***Re*=1100**
$\mathbf{X_{CO_2,210°C}}$	17.27%	12.73%	8.30%	6.14%
$\mathbf{Y_{CH_3OH,210°C}}$	15.61%	11.52%	7.37%	5.39%

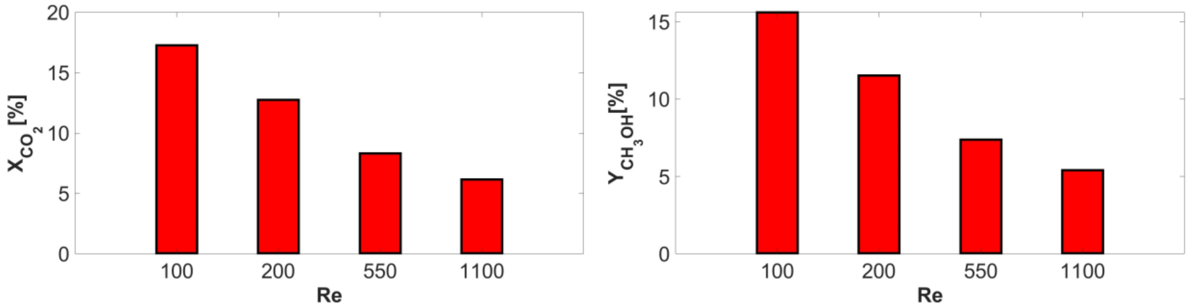

Figure 35. Bar graphs showing a summary of the CO_2 conversion (left) and methanol yield (right) parameters at T_w=210°C, for *Re*=100, *Re*=200, *Re*=550 and *Re*=1100, when the catalyst coating is applied over the entire length of the walls.

4.3 Effect of installing vortex generators (Group (C))

In the previous sections, methanol synthesis has been simulated under a perfectly laminar flow regime. Given these circumstances, the catalytic wall temperature (T_w) and bulk flow velocity (*Re*), which yield the greatest methanol concentration, have been identified. Moreover, two different scenarios (groups (A) and (B)) have been examined in this context.

In this section, the effect of transport-mediated mixing on the methanol yield is investigated. For this purpose, VGs are installed in the channel, downstream of the inlet section, as depicted in Figure 5. It is foreseen that the interaction of the reactive mixture with such vortex-generating elements is capable of inducing a chaotic fluid motion. Correspondingly, the goal is to impose radial mixing between the species involved in the synthesis, in the aim of further enhancing the methanol production. As in group (B) simulations, a fully-catalytic configuration of the channel, with T_w=210°C, is considered.

In the present analysis, two different configurations of VGs are compared under identical working conditions. Throughout the process, the trends of their different fields are presented and the discrepancies relative to the laminar cases are highlighted. Afterwards, a parameter sweep is performed on the more beneficial VG configuration, *i.e.* the one featuring a greater methanol yield. Finally, a conversion efficiency analysis is conducted, in which the reactor's performance is compared to that of the laminar simulations.

4.3.1 Comparison between the rectangular and square-shaped vortex generators

The comparison between the two proposed VGs, *i.e.* three square-shaped obstacles aligned in a spanwise row (Figure 5-i) and a single vertical rectangular obstacle (Figure 5-ii), is performed at T_w=210°C and *Re*=550. Initially, velocity, temperature and the concentrations of CO_2 and methanol throughout the channel are displayed for each case. The differences with respect to the simulations of group (B) are also emphasized. Additionally, the corresponding fluid streamlines are presented. Moreover, the time-averaged methanol trends at the reactor's outlet are plotted. Finally, to draw a robust conclusion, the spatiotemporal averages of the outlet methanol mass fractions are provided.

Monitoring the velocity field, it can clearly be observed that the introduction of VGs has significantly altered the flow characteristics within the channel (Figure 36 and Figure 38). Starting with a laminar profile at the inlet section, it is evident that the flow becomes unstable upon its collision with the obstacles. This is demonstrated by the oscillating velocity profile along the top and bottom walls, exhibited in the presence of each of the two configurations. Therefore, in both cases, the von Kármán instability (or vortex shedding) is triggered [70].

At this point, it is worth noting that the Reynolds number at the obstacle (Re_d) is not the same in both arrangements. Indeed, since the rectangular VG's characteristic dimension (d) is half of the channel's width, its Re_d is equal to half of Re, *i.e.* $Re_d=Re/2$. On the other hand, the side of each squared obstacle is d=D/6, thus, $Re_d=Re/6$. Therefore, simulating at $Re=550$, the Re_d values corresponding to the rectangular and square-shaped VGs are 275 and 91.67, respectively. This higher Re_d in the rectangular-obstacle case leads to an increased vortex-shedding frequency.

Referring to the radial velocity components (U_x) displayed by the two configurations (Figure 37), higher values are noticed just downstream of the VG in the squared-obstacle configuration. However, as the mixture travels further along the streamwise direction, the radial velocities caused by the rectangular VG are higher. Therefore, the squared-obstacle VG appears to induce a better local radial mixing in the channel, *i.e.* in the region of the obstacles, while the rectangular VG seems to result in the better global effect.

Concerning the fluid streamlines (Figure 39), the effect of VGs on inducing cross-flow and mixing is evident. Moreover, the alternating sequence of vortical structures observed at the walls represents a perfect demonstration of the von Kármán mode, exhibited in both situations.

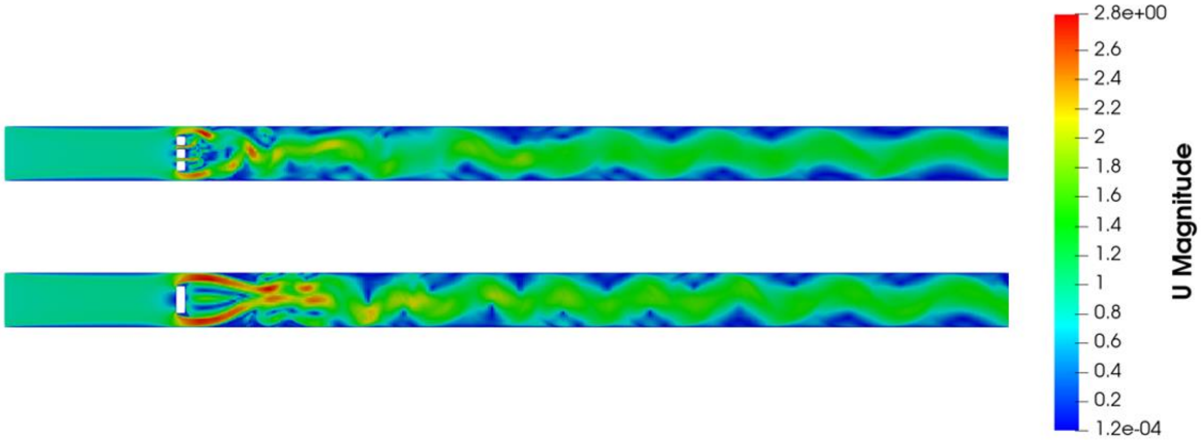

Figure 36. Velocity trend over the channel at T_w=210°C and Re=550 for both configurations of vortex generators (three square-shaped obstacles aligned in a spanwise row (top) and the single vertical rectangular obstacle (bottom)).

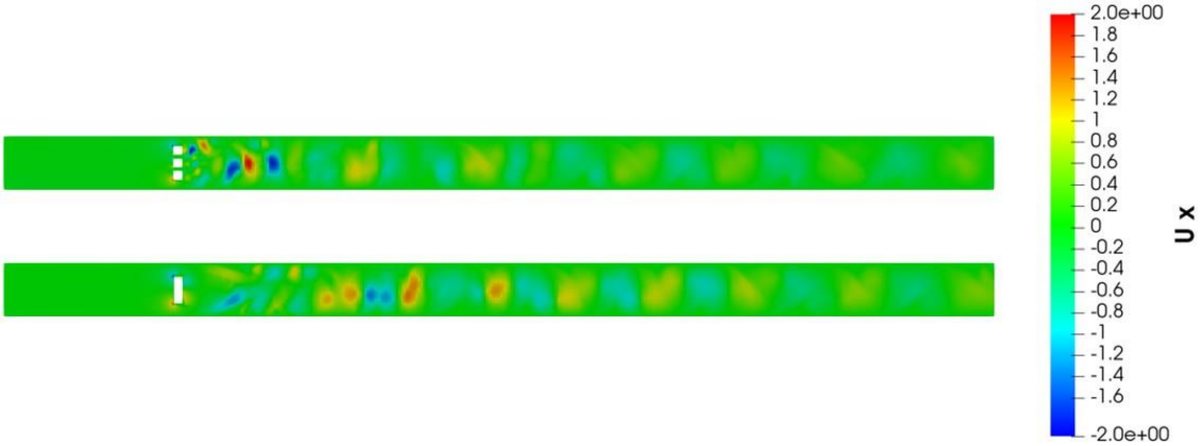

Figure 37. The trend of the radial velocity component (U_x) over the channel at T_w=210°C and *Re*=550 for both configurations of vortex generators (three square-shaped obstacles aligned in a spanwise row (top) and a single vertical rectangular obstacle (bottom)).

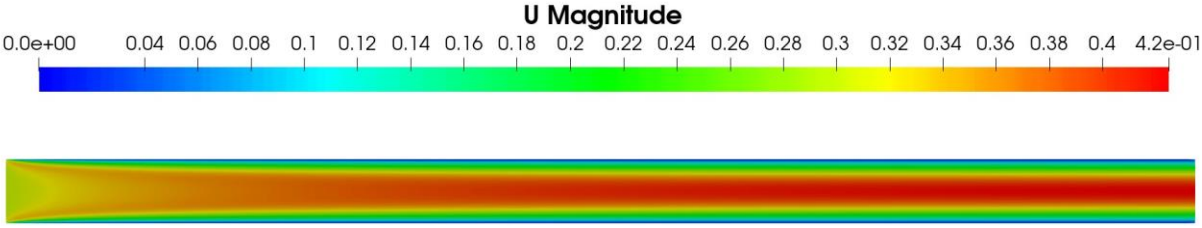

Figure 38. Velocity distribution over the channel at T_w=210°C and *Re*=550 in the laminar, obstacle-free case.

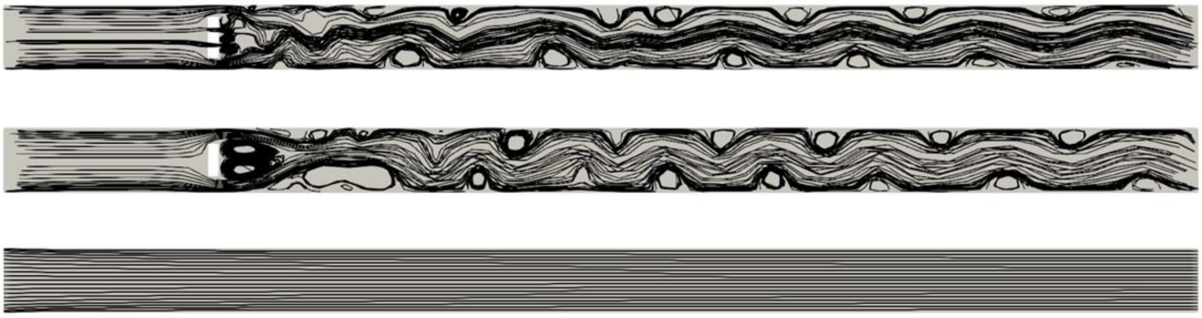

Figure 39. An OpenFOAM schematic representing the fluid streamlines in the presence of vortex generators (three square-shaped obstacles aligned in a spanwise row (top) and single vertical rectangular obstacle (middle)) and in the obstacle-free, laminar case (bottom) at T_w=210°C and *Re*=550.

In the context of heat exchange, the increased mixing of the fluid particles substantially promotes the internal convective heat transfer among them [71]. Comparing the temperature trends upstream and downstream of the VGs (Figure 40), the contribution of mixing can be readily understood. In all three cases, a laminar thermal boundary layer starts to develop at the reactor's inlet. In the absence of VGs (group (B) simulations), the thermal boundary layer continues to increase in width until the discharge. On the other hand, after the introduction of VGs (group (C) simulations), a completely distinct heat transfer behaviour is witnessed. The temperature boundary layer detaches once the flowing mixture strikes the obstacles. This drives the transition from a perfectly streamlined flow to a random, chaotic one.

Subsequently, the fluid entities undergo radial mixing and turning. Thereby, the influence of the wall heat transfer encompasses a greater portion of the fluid in these situations. This can be deduced by comparing the temperature distribution in the central regions of the channel between the simulations of group (C) and these of group (B).

All in all, the above discussion demonstrates the more effective convective heat exchange resulting from the installation of VGs. Moreover, the advantage of inducing mixing in the flow becomes even more notable when the fluid approaches the channel's outlet. In these regions, the temperature discrepancies between the solid walls and the fluid diminish further. Finally, monitoring the temperature trends, the VG in the form of a rectangular element seems to yield a more effective global heat transfer. This can be inferred from the higher overall temperature profile exhibited by its fluid mixture near the outlet of the channel.

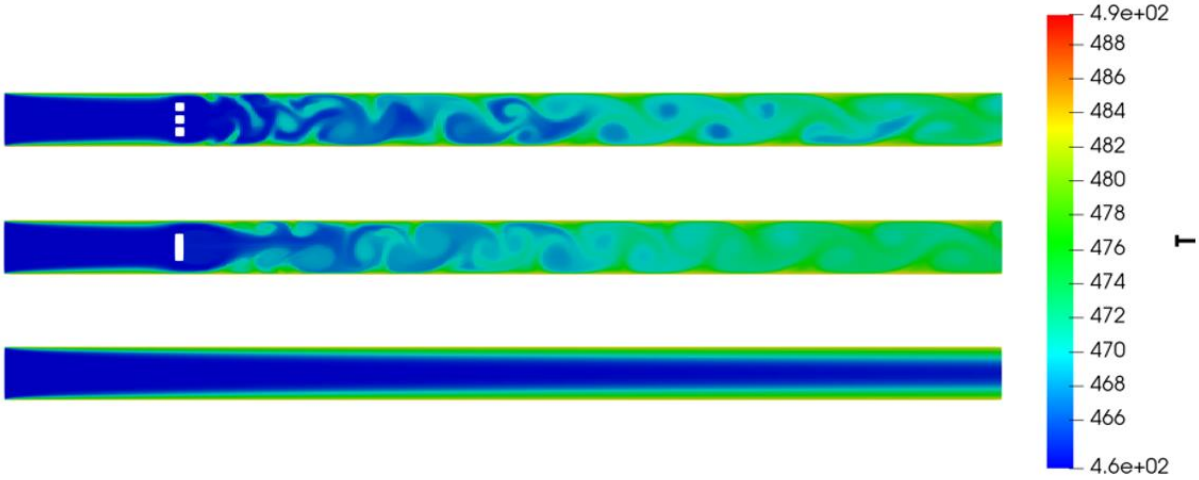

Figure 40. Temperature distribution over the channel at T_w=210°C and *Re*=550 in the presence of vortex generators (three square-shaped obstacles aligned in a spanwise row (top) and a single rectangular obstacle (middle)) and in the laminar obstacle-free case (bottom).

Regarding the involved chemical species, the effect of radial mixing is only investigated on the distributions of CO_2 (Figure 41) and CH_3OH (Figure 42). As previously mentioned, the behaviours of these two species serve as a comprehensive representation of the underlying physics in the catalytic channel.

Under the assumption of a unity Lewis number (Le_k=1), mass and heat diffusion throughout the reactor occur at the same rate. Therefore, the temperature and species fields exhibit identical trends. Accordingly, in each of the present simulation cases, the mass fraction boundary layers initiate at the inlet section with a laminar profile. In the obstacle-free case (group (B)), this boundary layer continues to develop smoothly until the reactor's outlet. Contrarily, the presence of vortex-generating obstacles leads to a boundary layer separation at their locations. This is due to the flow of the reactive fluid mixture over the VGs. Beyond the VGs, the flow continues with an unsteady, fluctuating profile as depicted in Figure 36. As a consequence, radial mixing of the reactive species is induced.

Referring to the mass fraction trends of CO_2 and CH_3OH, the transport-mediated mixing, driven by the VGs, seems to augment the methanol reactions and enhance the yield. Furthermore, in line with the temperature field findings, the rectangular-obstacle layout appears to be more advantageous.

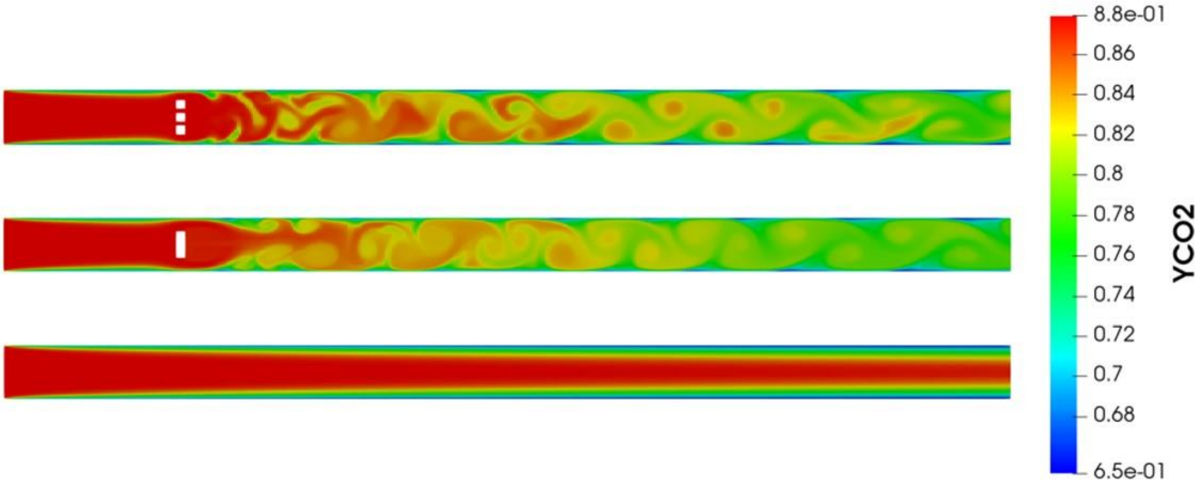

Figure 41. The distribution of the CO_2 mass fraction over the channel at T_w=210°C and *Re*=550 in the presence of vortex generators (three square-shaped obstacles aligned in a spanwise row (top) and a single rectangular obstacle (middle)) and in the laminar obstacle-free case (bottom).

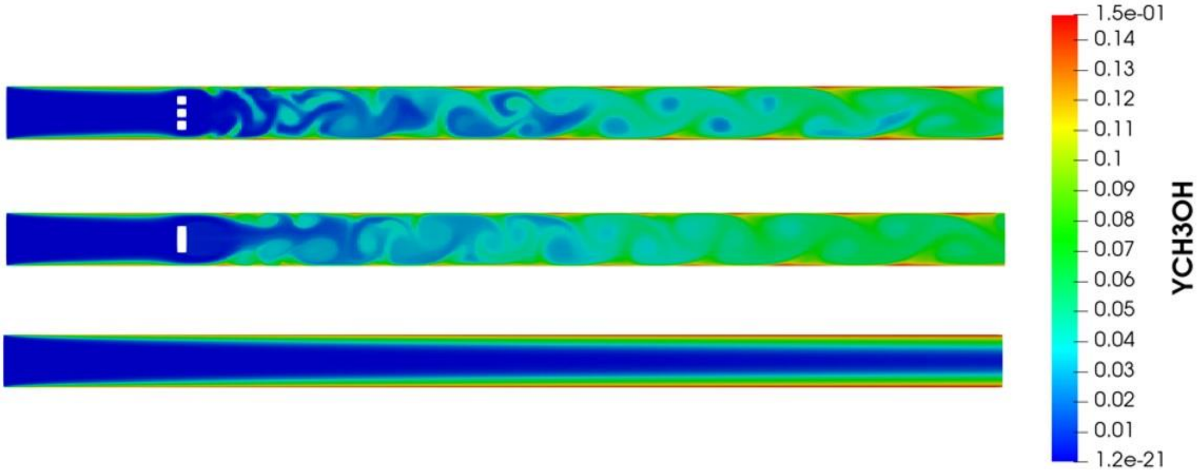

Figure 42. The distribution of the methanol mass fraction over the channel at T_w=210°C and *Re*=550 in the presence of vortex generators (three square-shaped obstacles aligned in a spanwise row (top) and a single rectangular obstacle (middle)) and in the laminar obstacle-free case (bottom).

At this stage, a proper quantitative comparison between simulations of groups (B) and (C) is conducted in order to unambiguously determine the more optimal vortex-generating arrangement. Their time-averaged methanol mass fractions are plotted along the spanwise dimension of the reactor's outlet. For unsteady flows, as in group (C) simulations, time-averaged profiles are more indicative as compared to instantaneous profiles. To elaborate further, in such simulations, since the flow doesn't achieve a steady state, the fields vary continuously between subsequent timesteps. On the contrary, in the simulations of groups (A) and (B), steady state is attained. Hence, both, time-averaged and instantaneous boundary layer trends equivalently depict the governing phenomena in these cases.

With reference to the plots of Figure 43, simulations involving transport-mediated mixing exhibit significantly higher methanol mass fractions in the central areas of the reactor, *i.e.* away from the catalytic walls. On the contrary, in the laminar scenario, the methanol mass fractions obtained in these regions are negligible. However, approaching the walls where reactions take place, different findings are visualized. The higher mass fractions are recorded by the laminar simulation in these locations. This is attributed to having a longer reaction residence time due to the smooth mixture-catalyst engagement. On the other hand, group (C) simulations are characterized by continuously fluctuating fluid motions between the walls, leading to a reduction in the residence time. Nevertheless, their yielded methanol mass fractions around the walls of the channel are still considered relatively high.

Comparing the relative outcomes of group (C) simulations, the rectangular-obstacle configuration exhibits a higher methanol mass fraction trend along the entire width of the outlet section, except at the walls, where curves approximately overlap. This indicates that the global transport-mediated mixing induced by the rectangular VG is more impactful with respect to that of the three squared-obstacles.

To draw a definitive conclusion about the impact of mixing on the methanol yield, the provided methanol mass fraction profiles are spatiotemporally averaged. The tabular entries (Table 21) and their corresponding bar graph (Figure 44) confirm that the installation of VGs, particularly the rectangular obstacle, has enhanced the catalytic synthesis of methanol.

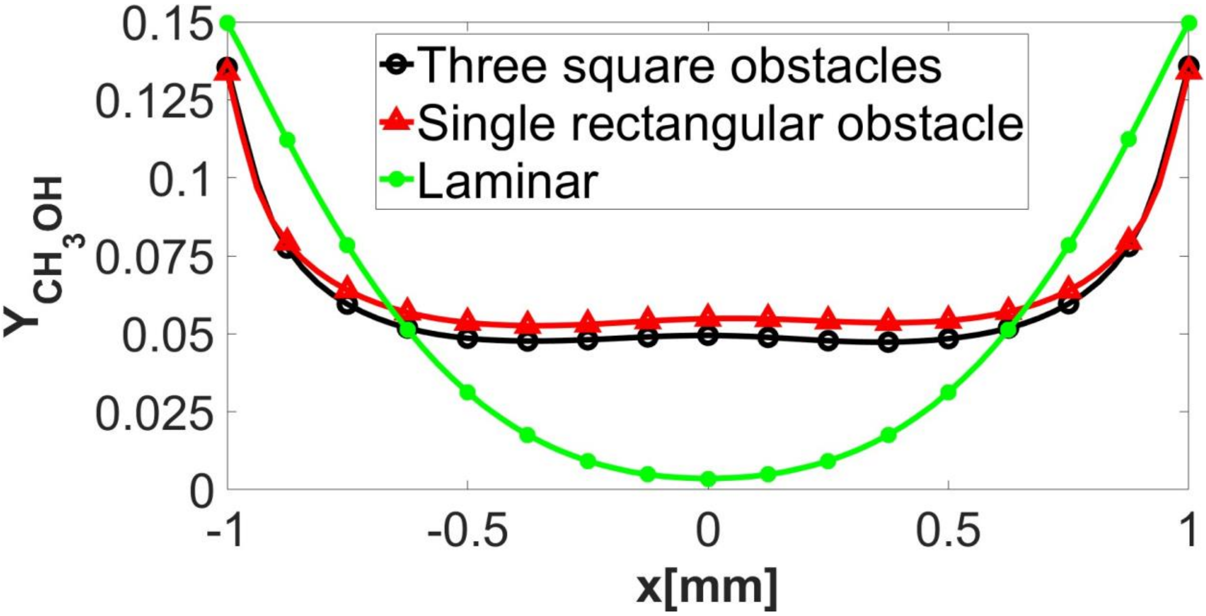

Figure 43. The time-averaged methanol mass fractions at the outlet of the reactor for each of the two vortex generator configurations and the perfectly laminar, obstacle-free case, at T_w=210°C and Re=550.

Table 21. Computation of the spatiotemporal average of the methanol mass fraction at the reactor's outlet for the two cases featuring vortex generators and the laminar, obstacle-free case at T_w=210°C and Re=550.

	Single rectangular obstacle	Three squared obstacles	Laminar
$\boldsymbol{Y_{CH_3OH,o,210°C}}$	**0.0627**	0.0585	0.0472

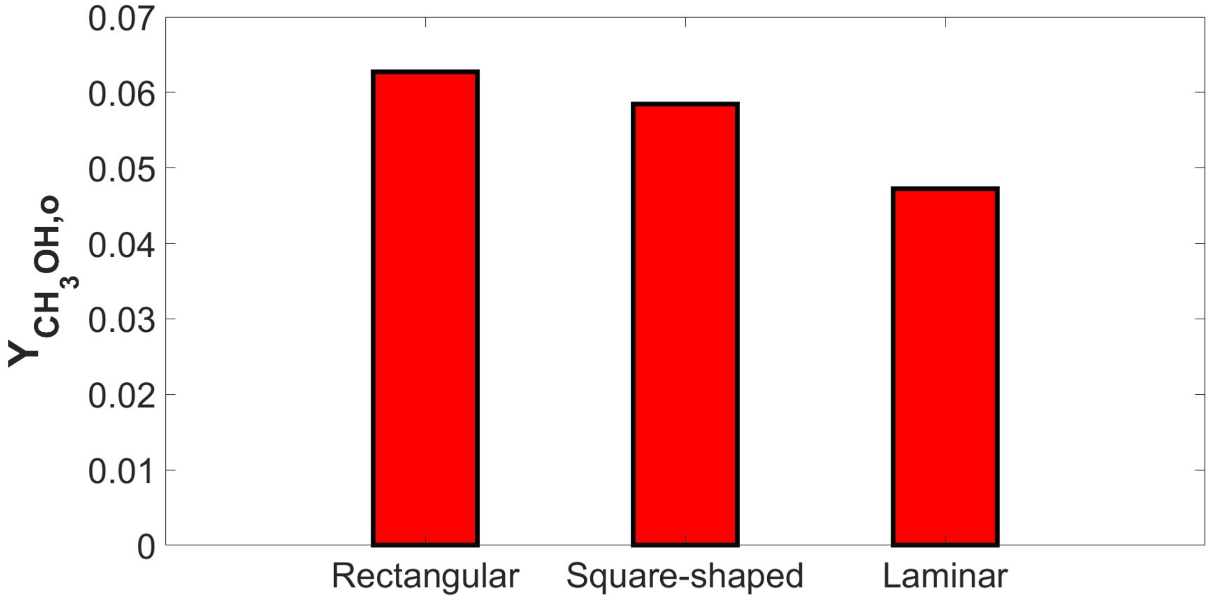

Figure 44. Bar graph illustrating the spatiotemporal averages of the methanol mass fractions at reactor's outlet for the two cases featuring vortex generators and the laminar, obstacle-free case, at T_w=210°C and *Re*=550.

4.3.2 Rectangular vortex generator parameter sweep

After demonstrating that the rectangular-obstacle configuration causes a more effective transport-mediated mixing, it is systematically examined in a parameter sweep. More specifically, maintaining the most favourable isothermal conditions at the walls (T_w=210°C), the synthesis is simulated for *Re*=100, *Re*=200, *Re*=550 and *Re*=1100, as in groups (A) and (B). The velocity and methanol distributions along the channel are presented for each *Re* (Figure 45). In addition to that, the outlet time-averaged mass fractions of the involved chemical species are plotted. A comparison with the time-averaged methanol profiles exhibited by group (B) simulations is also carried out.

At all simulated *Re*, it is apparent that radial mixing of the chemical species has been imposed by the VG. This is indicated by the unsteady, fluctuating flow profiles present downstream of the obstacle. At *Re*=100, a weak von Kármán mode is exhibited, which then starts to dampen as the flowing mixture advances further along the axial direction. Thereby, the flow becomes stable again and reaches the outlet of the channel with a perfectly laminar profile. Moreover, at *Re*=200, a delayed, low-frequency vortex shedding pattern is observed. In this case, the flow does not promptly manifest the von Kármán vortex street upon impinging on the obstacle; instead, it occurs at an extended distance downstream. The flow remains unstable as it approaches the outlet. Increasing *Re*, the vortex-shedding frequency increases, which leads to stronger von Kármán modes as in cases *Re*=550 and *Re*=1100.

Addressing the methanol field, equivalent outcomes to these of section 4.3.1 are attained. Accordingly, laminar methanol boundary layers initiate at the inlet of the reactor, with decreasing widths observed at higher bulk flow velocities. These boundary layers separate as a result of the collision between the fluid and the obstacle. At this stage, the von Kármán instability activates and the flow-induced mixing causes a random methanol formation over the wall-normal direction. The von Kármán instability persists until the outlet of the reactor in all cases, except for *Re*=100. In this particular scenario, the flow retains its laminar state at a certain distance beyond the obstacle. Hereafter, a laminar boundary layer enriched with methanol forms and continues to develop until the catalytic segment's discharge.

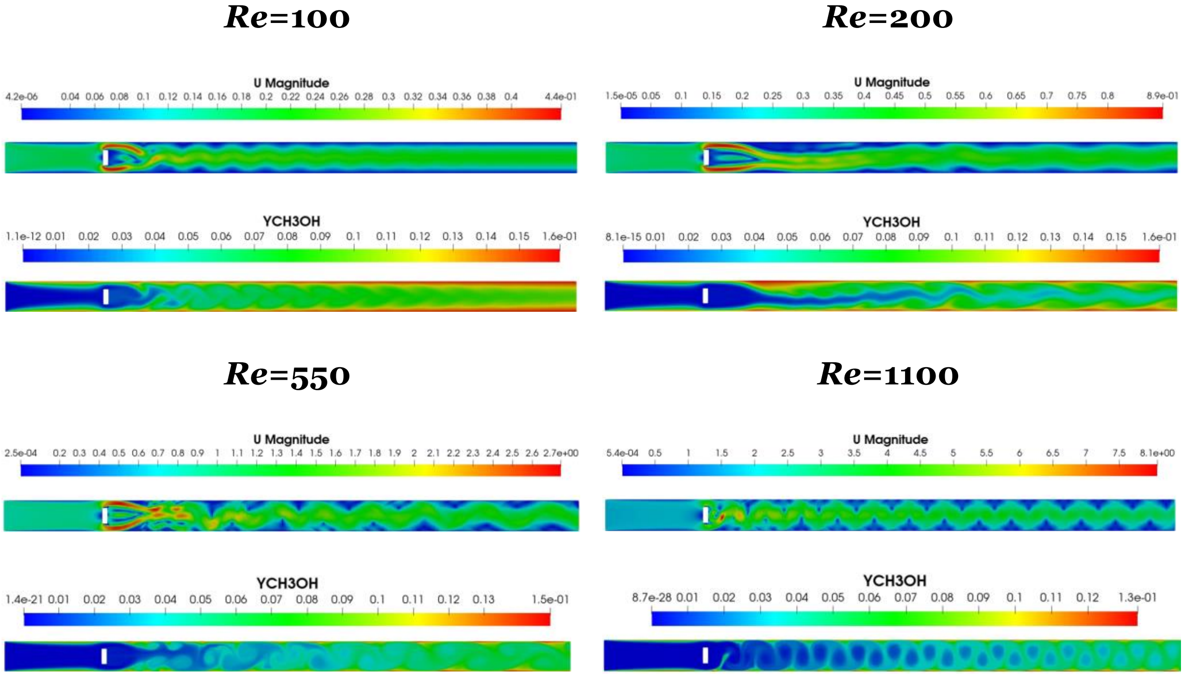

Figure 45. Velocity and methanol distributions in the reactor in the presence of the rectangular vortex generator, at T_w=210°C, for *Re*=100, *Re*=200, *Re*=550 and *Re*=1100.

Presently, the time-averaged mass fraction trends of the reactants and products along the channel's outlet are provided. The general outcome is similar to what has been found in groups (A) and (B). For instance, at *Re*=100, the highest yielded mass fractions (Figure 47) and equivalently, the lowest reactants concentrations (Figure 46), are observed. The increase in *Re* leads to a consistent diminishment in the products' mass fractions. As stated earlier, this is largely attributed to the reduction in the reactions' residence time. Consequently, the highest unreacted concentrations of CO_2 and H_2 are recorded at *Re*=1100. This translates into the lowest produced mass fractions of CH_3OH and its by-products.

Nonetheless, inducing radial mixing in the reactive mixture of species has had a notable influence on the synthesis. Monitoring the mass fraction trends of the species away from the catalytic walls, a notable concentration of methanol is formed, even at the highest bulk flow velocities. However, the disparities in the species mass fractions at the walls between different *Re* are more evident with respect to groups (A) and (B). Increasing *Re*, stronger oscillations in the flow, at an increased frequency, are observed. Therefore, in the simulations of group (C), the increase in the bulk flow velocity causes greater reductions in the reactions' residence time as compared to the initial laminar cases. This results in more noticeable drops in the yielded mass fractions at the channel's walls.

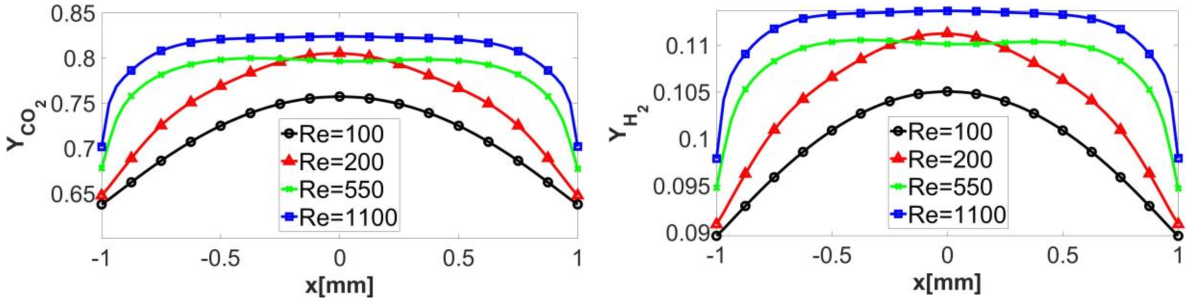

Figure 46. Time-averaged CO_2 and H_2 mass fractions along the wall-normal direction of the reactor's outlet after the introduction of a rectangular vortex generator, at T_w=210°C, for *Re*=100, *Re*=200, *Re*=550 and *Re*=1100.

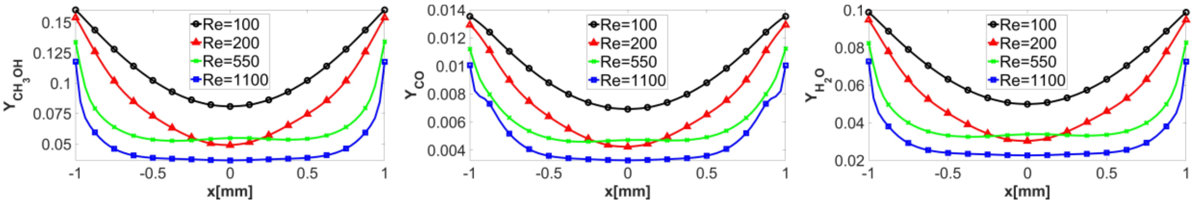

Figure 47. Time-averaged mass fractions of methanol, CO and H_2O along the wall-normal direction of the reactor's outlet after the introduction of the rectangular vortex generator, at T_w=210°C, for *Re*=100, *Re*=200, *Re*=550 and *Re*=1100.

The influence of transport-mediated mixing can be further emphasized by performing an analogy with the corresponding laminar cases (Group (B)). In due course, a comparison plot of the achieved methanol profiles is provided, at every examined *Re* (Figure 48).

At *Re*=100, the installation of a VG yields a higher methanol profile all over the outlet section of the reactor. In this case, despite the flow becoming laminar again upstream of the outlet, the radial mixing induced in the region of the obstacle proves to be advantageous. Furthermore, similar findings are observed at *Re*=200. More precisely, in the central regions of the channel, the methanol trend exhibited by the group (C) simulation is significantly greater. Approaching the upper and lower walls, equivalent mass fraction trends are achieved as the two curves almost coincide. Increasing *Re* to 550 and 1100, greater disparities between the methanol trends are noticed over the full width. Around the central axis of the channel, the methanol yield is substantially larger when the VG is present. Contrastingly, in the laminar, obstacle-free case, a free-stream region is present near the middle of the channel at *Re*=1100, whereas at *Re*=550, the concentration of methanol formed in that area is minimal. However, close to the walls, the laminar simulations exhibit higher mass fractions. As previously discussed, the oscillating flow generated by the VG leads to a reduction in the reaction residence time, causing a lower yield near the walls. These discrepancies increase at higher *Re*. Nevertheless, the methanol yielded at the catalytic walls in the presence of the VG is still considered relatively high.

To sum up, the installation of the VG has induced transport-mediated mixing between the reacted and unreacted species. This has led to the formation of a considerable methanol concentration along the whole outlet cross-section, even at central widths. Albeit, the yield at the locations of the catalytic walls has diminished. In the upcoming section, a quantitative analysis is carried out to address this matter.

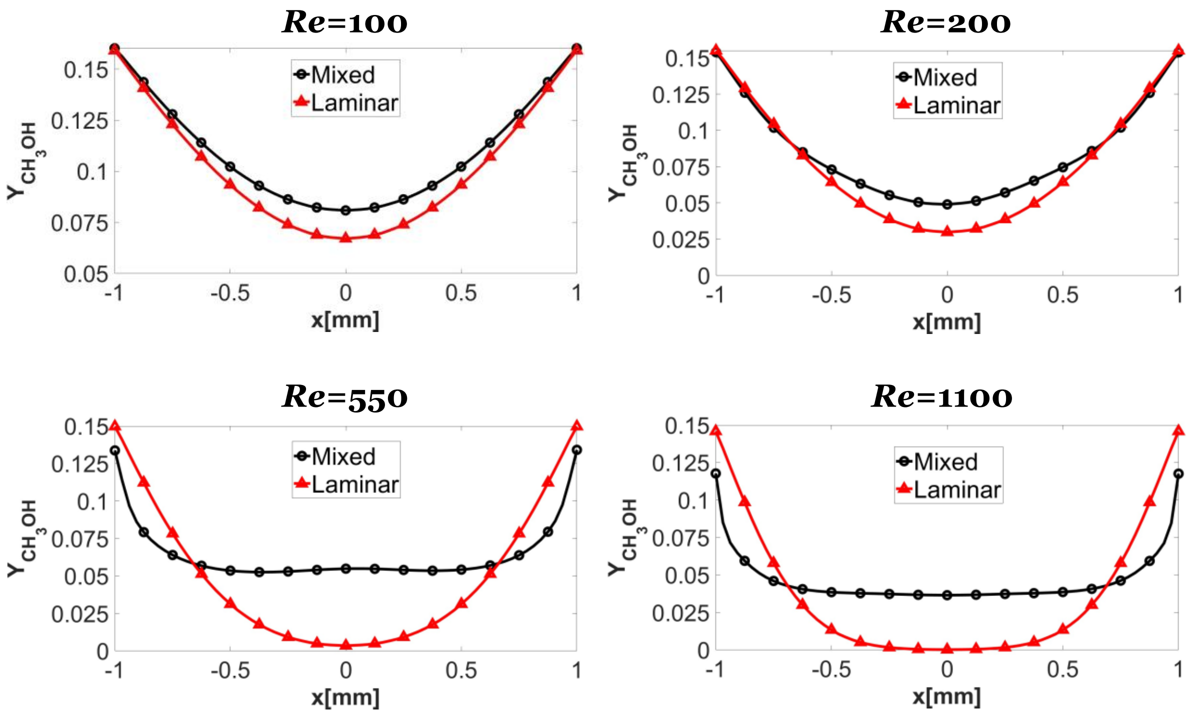

Figure 48. Comparison between the time-averaged methanol mass fraction profiles along the wall-normal direction of the reactor's outlet in the presence of the rectangular vortex generator and in the obstacle-free, laminar case, under the same *Re*, at T_w=210°C.

4.3.3 Averaged mass fractions at the reactor's outlet and conversion efficiency

In the previous section, the contribution of convection-driven mixing on the methanol yield has been qualitatively analysed. Within this passage, the reactor's performance after the introduction of a rectangular vortex-generating obstacle is quantified at all examined *Re*. In this regard, outlet spatiotemporal averages of CO_2 and CH_3OH mass fractions are computed. Subsequently, utilizing these data, the conversion efficiency is investigated.

Referring to Table 22, it is evident that inducing transport-mediated mixing has led to a decrease in the averaged unreacted CO_2 mass fraction at the outlet. This implies an enhancement in the reactions occurring in the catalytic channel with respect to the laminar cases. A comparison between the values recorded by groups (B) and (C) is presented in Figure 49.

Table 22. A comparison of the spatiotemporal averages of the CO_2 mass fractions along the wall-normal direction of the reactor's outlet between the cases featuring a rectangular vortex generator and their corresponding laminar, obstacle-free cases at T_w=210°C, for *Re*=100, *Re*=200, *Re*=550 and *Re*=1100.

	***Re*=100**	***Re*=200**	***Re*=550**	***Re*=1100**
$Y_{CO_2,o,210°C,mixed}$	0.716	0.755	0.784	0.81
$Y_{CO_2,o,210°C,laminar}$	0.728	0.768	0.807	0.826

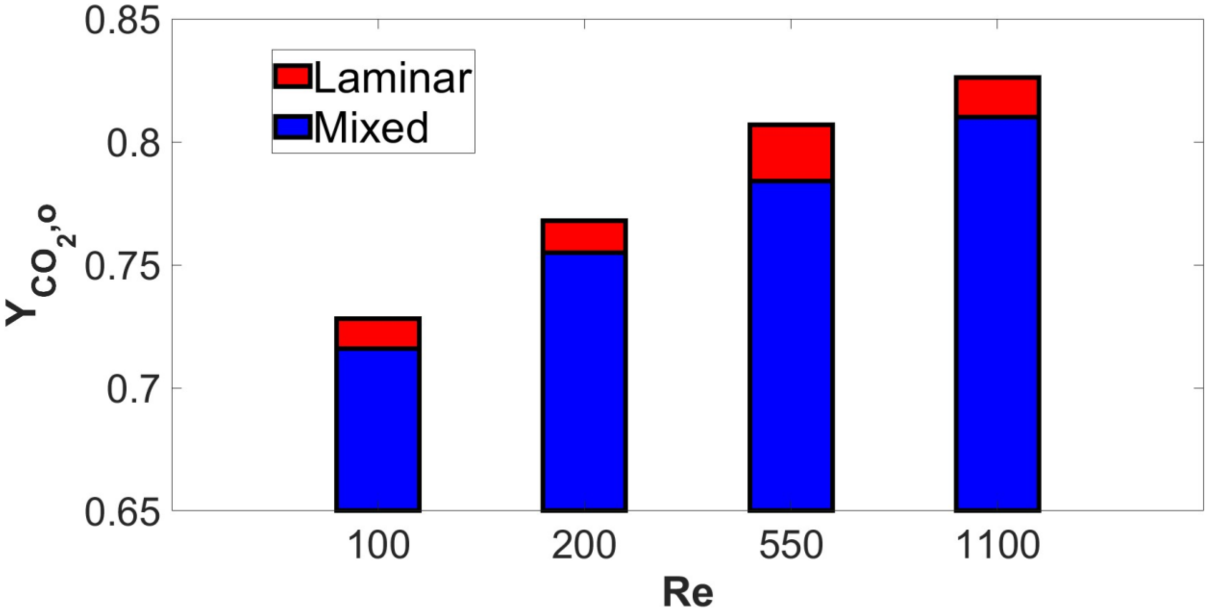

Figure 49. Bar graph comparing the spatiotemporal averages of the CO_2 mass fractions along the wall-normal direction of the reactor's outlet between the cases featuring a rectangular vortex generator and their corresponding laminar, obstacle-free cases at T_w=210°C, for *Re*=100, *Re*=200, *Re*=550 and *Re*=1100.

Presumably, under identical thermo-fluid dynamic conditions, the greater concentration of reacted CO_2 yields an increased methanol formation (Table 23). The outlet averaged methanol mass fractions are plotted (Figure 50). Moreover, the estimates of the corresponding averaged produced methanol mass flow rates are reported (Table 24).

Table 23. A comparison of the spatiotemporal averages of the methanol mass fractions along the wall-normal direction of the reactor's outlet between the cases featuring a rectangular vortex generator and their corresponding laminar, obstacle-free cases at T_w=210°C, for *Re*=100, *Re*=200, *Re*=550 and *Re*=1100.

	***Re*=100**	***Re*=200**	***Re*=550**	***Re*=1100**
$Y_{CH_3OH,o,210°C,mixed}$	0.109	0.0821	0.0627	0.0451
$Y_{CH_3OH,o,210°C,laminar}$	0.1	0.0738	0.0472	0.0345

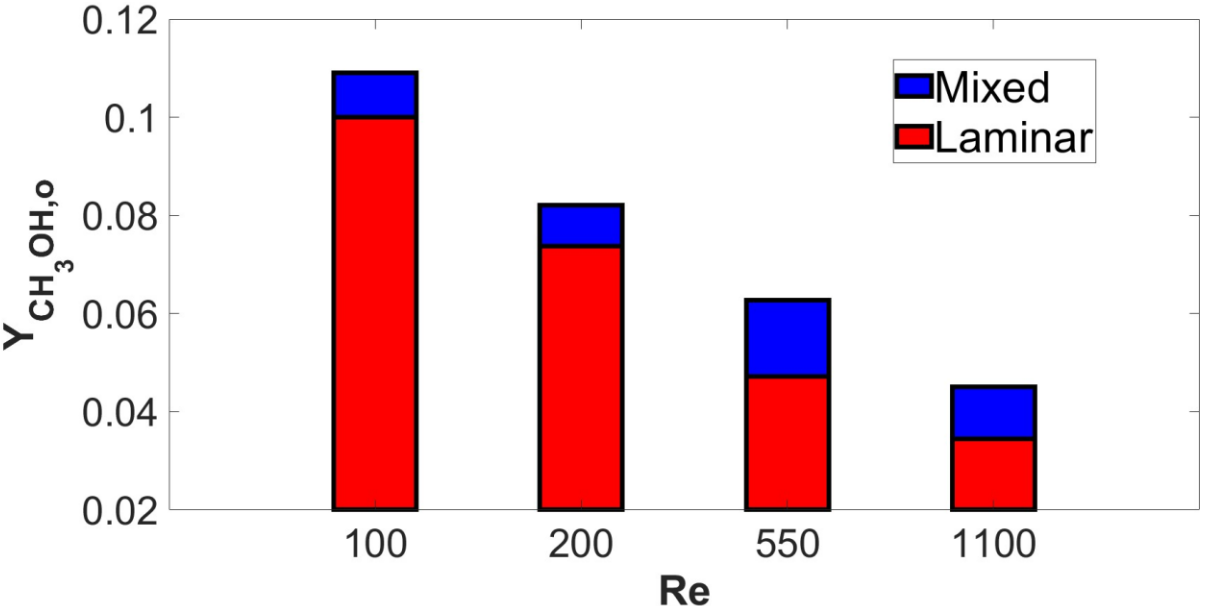

Figure 50. Bar graph comparing the spatiotemporal averages of the methanol mass fractions along the wall-normal direction of the reactor's outlet between the cases featuring a rectangular vortex generator and their corresponding laminar, obstacle-free cases, at T_w=210°C, for *Re*=100, *Re*=200, *Re*=550 and *Re*=1100.

Table 24. A comparison of the estimated spatiotemporal averages of the produced methanol mass flow rates between the cases featuring a rectangular vortex generator and their equivalent laminar, obstacle-free ones, at T_w=210°C, for *Re*=100, *Re*=200, *Re*=550 and *Re*=1100.

	***Re*=100**	***Re*=200**	***Re*=550**	***Re*=1100**
$\dot{m}_{CH_3OH,o,210°C,mixed}$ **[kg/s]**	1.06e-06	1.59e-06	3.34e-06	4.78e-06
$\dot{m}_{CH_3OH,o,210°C,laminar}$ **[kg/s]**	9.68e-07	1.43e-06	2.51e-06	3.66e-06

Finally, after demonstrating that installing a VG in the channel enhances the rate of methanol production, its impact on the conversion efficiency is addressed. For this concern, the values of $\mathbf{X_{CO_2}}$ (Table 25) and $\mathbf{Y_{CH_3OH}}$ (Table 26) are reported for the two investigated scenarios. The tabulated values of $\mathbf{X_{CO_2}}$ and $\mathbf{Y_{CH_3OH}}$ are plotted (Figure 51 and Figure 52, respectively). Comparing individual findings at the same *Re*, it is evident that the cases involving transport-mediated mixing of the reactive species (Group (C)) outperform the parallel-streamlined ones (Group (B)). Indeed, placing a vortex-generating element in the reactor results in a better conversion of reactants into products (Table 25). Thus, it has led to a better reactor performance and consequently, a greater methanol yield (Table 26). In particular, the most notable efficiency improvements, relative to the obstacle-free cases, are observed at *Re*=550, followed by *Re*=1100. In the former case, $\mathbf{X_{CO_2}}$ and $\mathbf{Y_{CH_3OH}}$ have increased by 31.45% and 32.85%, respectively. The latter case features respective increases of 29.48% and 30.73% for $\mathbf{X_{CO_2}}$ and $\mathbf{Y_{CH_3OH}}$.

Table 25. A comparison of the CO_2 conversion parameter of the reactor between the cases featuring a rectangular vortex generator and their equivalent laminar, obstacle-free ones, at T_w=210°C, for *Re*=100, *Re*=200, *Re*=550 and *Re*=1100.

	***Re*=100**	***Re*=200**	***Re*=550**	***Re*=1100**
$X_{CO_2,o,210^{\circ}C,mixed}$	18.64%	14.20%	10.91%	7.95%
$X_{CO_2,o,210^{\circ}C,laminar}$	17.27%	12.73%	8.30%	6.14%

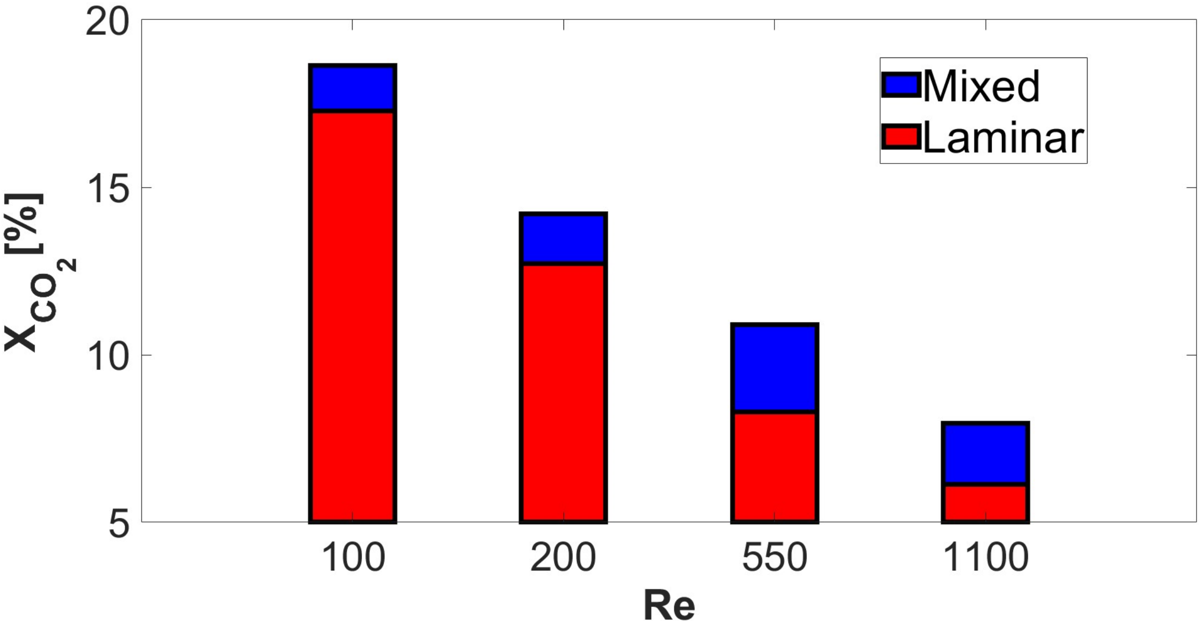

Figure 51. Bar graph comparing the CO_2 conversion parameter of the reactor between the cases featuring a rectangular vortex generator and their equivalent laminar, obstacle-free ones, at T_w=210°C, for *Re*=100, *Re*=200, *Re*=550 and *Re*=1100.

Table 26. A comparison between the methanol yield parameter of the reactor between the cases featuring a rectangular vortex generator and their equivalent laminar, obstacle-free ones, at T_w=210°C, for *Re*=100, *Re*=200, *Re*=550 and *Re*=1100.

	***Re*=100**	***Re*=200**	***Re*=550**	***Re*=1100**
$Y_{CH_3OH,o,210^{\circ}C,mixed}$	17.014%	12.815%	9.787%	7.040%
$Y_{CH_3OH,o,210^{\circ}C,laminar}$	15.609%	11.519%	7.367%	5.385%

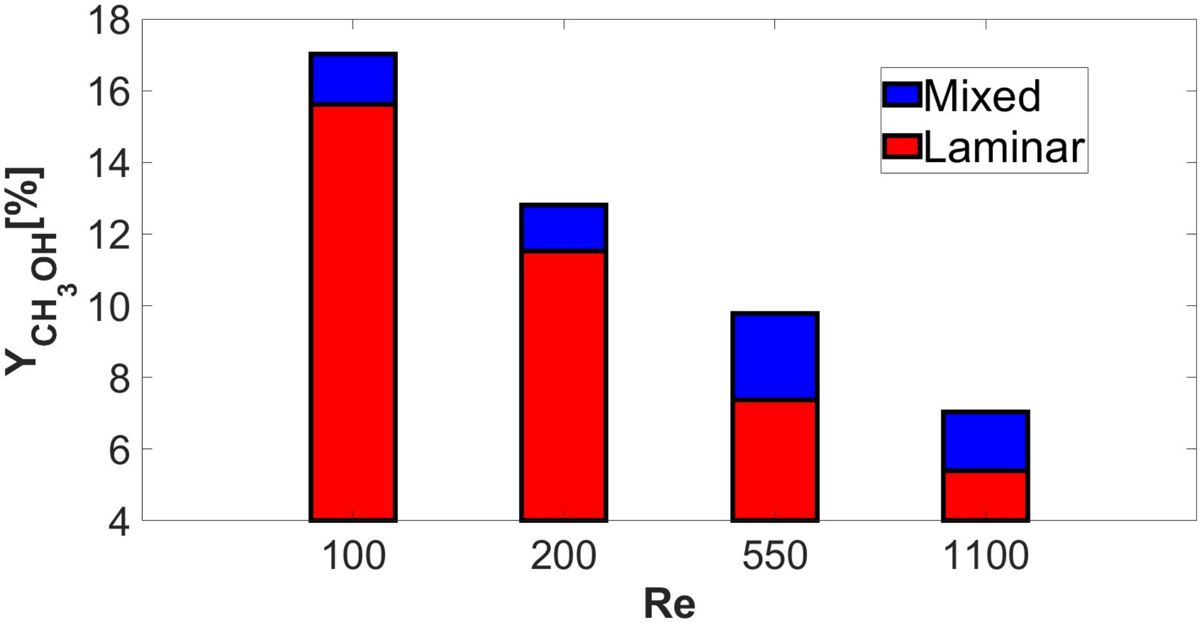

Figure 52. Bar graph comparing the methanol yield parameter of the reactor between the cases featuring a rectangular vortex generator and their equivalent laminar, obstacle-free ones, at T_w=210°C, for *Re*=100, *Re*=200, *Re*=550 and *Re*=1100.

5) Conclusion

In this thesis, the catalytic synthesis of methanol has been studied in a rectangular microchannel reactor using 2D CFD simulations executed on the OpenFOAM software. The reactingFoam solver has been chosen to accomplish this task. The adopted computational domain is of dimensions 37mm×2mm. Methanol is generated from the hydrogenation of either CO_2 or CO, in the presence of a catalytic material, based on copper or zinc oxide, coated on the channel walls. These reactions are known for being exothermic. The third reaction yielding from the synthesis is the RWGS, which is of an endothermic nature. This reaction results in the formation of methanol's by-products, CO and H_2O. The aforementioned reactions, governing the methanol synthesis of the channel, have been modelled on its catalytic walls according to the chemical model based on LHHW kinetics. This permits coupling the reactions with the required set of NS-equations. An isobaric condition of 5 MPa has been set within the reactor to drive the synthesis. Additionally, the density of the applied catalyst is maintained at 278.334 g/cm^3. Moreover, in order to ensure a stoichiometric catalytic synthesis, the inlet mass fractions of CO_2 and H_2 have been set to 0.88 and 0.12, respectively.

In accordance with the previous considerations, the methanol production simulations have been conducted. Namely, three simulation groups ((A),(B) and (C)) have been created, each characterized by particular channel features. Group (A) simulations feature flow recycling prior to the zone which encompasses the chemical reactions. On the other hand, in groups (B) and (C), the solid walls of the reactor are entirely coated with the catalyst. This permits the occurrence of the reactions along the full length of the channel. Groups (A) and (B) feature identical geometries, with the only difference being the reacting zone length. Contrarily, in group (C) simulations, vortex-generating elements are located downstream of the inlet section. Concerning the flow properties, the flowing reactive species maintain parallel streamlines from the inlet to the discharge in simulations pertaining to groups (A) and (B). However, after the introduction of VGs in group (C) cases, the flow profile is significantly altered. More precisely, upon the impingement of the fluid on the obstacles, a downstream transport-mediated mixing is induced. This results in an unsteady flow, which involves the crossing of streamlines and the formation of vortices. In all three groups, the examined bulk flow velocities correspond to Re=100, Re=200, Re=550 and Re=1100.

Before investigating the findings of each simulation set, a mesh convergence study has been executed. Comparing the findings of three different meshes at Re=1100 and T_w=200°C, a total number of 26048 cells proves to guarantee near-optimal computational accuracy. As a consequence, this is the number of cells which constitutes the computational grid adopted for groups (A) and (B). Concerning group (C), an increased accuracy is presumably necessary for precisely capturing the involved physics. Thus, a further refinement of the mesh is implemented in the region surrounding the obstacles, causing an increase in the number of computational cells. Indeed, no explicit mesh convergence study is carried out in this case as it has proved to be extremely expensive and unfeasible on standard academic computational resources. Nevertheless, it is foreseen that utilizing such a high-quality mesh offers a decent level of accuracy.

In simulations of group (A), a parameter sweep is performed over the catalytic wall temperature (T_w) and Re. At each of the above-stated Re, six simulations have been conducted by varying T_w along the functional temperature range of the catalyst (200-

250°C) using 10°C steps. Assuming Le_k=1, the diffusion of species and the diffusion of heat exhibit identical behaviours. At any temperature, the higher the *Re*, the smaller the widths of the boundary layers exhibited at the reactor's outlet. This is due to reductions in reaction and heat transfer residence times. As a result, lower methanol mass fractions are produced and the reactor's performance worsens. On the contrary, at low bulk flow velocities, the high residence time permits effective diffusive mixing and ensures optimal interaction between the reactants and the wall catalyst. As a result, the most effective heat transfer and the greatest yielded methanol mass fraction are observed at *Re*=100. Concerning the temperature effect, the most optimal range is 210°C ≤ T_w ≤ 220°C. Namely, T_w=210°C leads to obtaining the greatest methanol yields. As the temperature increases further, although the catalyst's operativity is enhanced, methanol production is hindered. Since the two reactions yielding methanol are exothermic and favor reduced temperatures, the temperature increase diminishes the methanol yield. Accordingly, the RWGS shift becomes more favorable, which leads to an increased formation of CO. In fact, RWGS is an endothermic reaction which favors higher temperatures.

After demonstrating that T_w=210°C is the ideal temperature for synthesizing methanol, this temperature setting at the catalytic walls is chosen and maintained unchanged in all the remaining simulations. Proceeding to simulations of group (B), exactly the same findings have been attained, as the yielded mass fractions diminish with the increase in *Re*. However, the increase in the wall dimension at which the catalyst is active allows for the boundary layers to develop to a greater width. Thereby, a more effective heat transfer and a higher methanol yield is visualized. Hence, increasing the length of the reactive zone enhances the performance of the reactor.

Finally, the effect of transport-mediated mixing has been thoroughly investigated in simulations falling into category (C). Simulating at *Re*=550, it is evident that the induced mixing in the flow has yielded notable improvements in heat transfer as compared to the laminar simulation cases. Moreover, the installation of VGs has driven an increased amount of reactants into the synthesis, especially around the middle of the channel. Even though the chaotic fluid motion and its corresponding oscillating trend have reduced the residence times, the overall outcome is a methanol throughput increase and hence, a better reactor performance with respect to perfectly laminar flows. Comparing the two proposed arrangements of VGs, *i.e.* the single rectangular obstacle and the three squared obstacles aligned in a spanwise row, the rectangular one exhibits a more beneficial global influence.

After demonstrating the superiority of the rectangular VG over the squared-element configuration, simulations have been performed for *Re*=100, *Re*=200 and *Re*=1100. For all values of *Re*, a notable yield is recorded away from the catalytic walls, *i.e.* middle of the channel, even at *Re*=1100. Comparing the findings to these of group (B), the yielded methanol mass fractions around the middle of the reactor are significantly greater when a VG is present. However, since flow oscillations decrease the residence time, the laminar cases exhibit larger methanol yield profiles around the walls, in general, especially at the relatively high *Re* (*Re*=550 and *Re*=1100). In spite of that, methanol mass fractions recorded by simulations of group (C) around the catalytic walls are considered comparatively high. Overall, the average yields in the presence of a VG are enhanced in every examined situation. Lastly, also when advection-driven mixing is induced, the formed concentration of methanol increases with the decrease in *Re*. As *Re* increases, the flow features increased fluctuations, triggering a greater degree of mixing among the different species. In spite of that, the reaction residence time remains the determining factor in methanol synthesis since its decrease causes a diminishment in the produced mass fractions, regardless of the resultant enhanced mixing.

Regarding potential future work, conducting full 3D simulations, wherein the catalytic material is coated on all four walls of the reactor (duct), would be of high interest. In these cases, employing the optimal temperature and bulk flow velocity determined in the 2D model could demonstrate a notably greater enhancement of the methanol yield. For instance, in the cases featuring VGs, the velocity component in the 3rd dimension, which is omitted from the 2D analysis, might have a remarkable influence on the synthesis. Equivalently, running 3D turbulent simulations could yield significant findings. Additionally, regarding the diffusion phenomena in the microchannel reactor, different modelling approaches could be adopted. Instead of Fick's law, which computes diffusion velocities of species solely based on their mass fraction gradients and diffusion coefficients, alternative diffusion models that account for molecular mass discrepancies could be adopted. Furthermore, another consideration could be that mass and heat diffusion do not behave identically in the system ($Le_k \neq 1$). This would result in distinct diffusion coefficients for the different involved species.

References

[1] "IPCC, 2022: Climate Change 2022: Impacts, Adaptation and Vulnerability. Contribution of Working Group II to the Sixth Assessment Report of the Intergovernmental Panel on Climate Change," Cambridge University Press, Cambridge, UK and New York, NY, USA, 2022.

[2] "Andres RJ, Boden TA, Bréon FM, Ciais P, Davis S, Erickson D, Gregg JS, Jacobson A, Marland G, Miller J, Oda T, Olivier JGJ, Raupach MR, Rayner P, Treanton K.: A synthesis of carbon dioxide emissions from foss".

[3] Abas N, Kalair A, Khan N, "Review of fossil fuels and future energy technologies," *Futures,* vol. 69, pp. 31-49, 2015.

[4] Das AK, Sharma A, "Climate change and the energy sector," *Advancement in Oxygenated Fuels for Sustainable Development,* pp. 1-6, 2023.

[5] Huesemann MH, "The limits of technological solutions to sustainable development," *Clean Technologies and Environmental Policy,* vol. 5, no. 1, pp. 21-34, 2003.

[6] "IEA (2018), World Energy Outlook 2018, IEA, Paris https://www.iea.org/reports/world-energy-outlook-2018, License: CC BY 4.0".

[7] Erickson LE, Brase G, "Paris Agreement on Climate Change," in *Reducing Greenhouse Gas Emissions and Improving Air Quality*, New York, CRC Press, 2019, pp. 11-22.

[8] "Serrano-Sanchez C, Olmeda-Delgado M, and Petrakopoulou F, "Exergy and Economic Evaluation of a Hybrid Power Plant Coupling Coal with Solar Energy," Applied Sciences, vol. 9, no. 5, p. 850, Feb. 2019, doi: 10.3390/app9050850.".

[9] Notton G, Nivet ML, Voyant C, Paoli C, Darras C, Motte F, Fouilloy A, "Intermittent and stochastic character of renewable energy sources: Consequences, cost of intermittence and benefit of forecasting,," *Renewable and Sustainable Energy Reviews,* vol. 87, pp. 96-105, 2018.

[10] Bellotti D, Rivarolo M, Magistri L, Massardo AF, "Feasibility study of methanol production plant from hydrogen and captured carbon dioxide," *Journal of CO2 Utilization,* vol. 21, pp. 132-138, 2017.

[11] Heard BP, Brook BW, Wigley TML, Bradshaw CJA, "Burden of proof: A comprehensive review of the feasibility of 100% renewable-electricity systems," *Renewable and Sustainable Energy Reviews,* vol. 76, pp. 1122-1133, 2017.

[12] Hansen K, Breyer C, Lund H, "Status and perspectives on 100% renewable energy systems," *Energy,* vol. 175, pp. 471-480, 2019.

[13] Zappa W, Junginger M, Broek MVD, "Is a 100% renewable European power system feasible by 2050?," *Applied Energy,* vol. 233–234, pp. 1027-1050, 2019.

[14] "IRENA (2019), Innovation landscape for a renewable-powered future: Solutions to integrate variable renewables. International Renewable Energy Agency, Abu Dhabi.".

[15] Cleary K, "Electrification 101," Resources for the Future, Washington, 2019.

[16] Pereirinha PG, González M, Carrilero I, Anseán D, Alonso J, Viera JC, "Main Trends and Challenges in Road Transportation Electrification," *Transportation Research Procedia,* vol. 33, pp. 235-242, 2018.

[17] Tan D, "Transportation Electrification: Challenges and opportunities," *IEEE Power Electronics Magazine,* vol. 3, no. 2, pp. 50-52, 2016.

[18] Kshirsagar P, Ewanchuk J, Kheraluwala M, "Next Generation of Robust Aviation Electrification - Challenges and Opportunities," in *2021 IEEE International Electron Devices Meeting (IEDM),* San Francisco, CA, USA, 2021.

[19] Schnuelle C, Thoeming J, Wassermann T, Thier P, Gleich AV, Reisemann SG, "Socio-technical-economic assessment of power-to-X: Potentials and limitations for an integration into the German energy system," *Energy Research & Social Science,* vol. 51, pp. 187-197, 2019.

[20] Wulf C, Zapp P, Schreiber A, "Review of Power-to-X Demonstration Projects in Europe," *Frontiers in Energy Research,* vol. 8, 2020.

[21] Schnettler A, Pflug V, Zindel E, Zimmermann G, Olvera OR, Pyc I, Trulley C, "Power-to-X: The crucial business on the way to a carbon-free world," Siemens Energy, Inc, Houston, Texas 77079, USA, 2020.

[22] Aneke M, Wang M, "Energy storage technologies and real life applications – A state of the art review," *Applied Energy,* vol. 179, pp. 350-377, 2016.

[23] Valverde JI, Arévalo LJP, Tsatsaronis G, Morosuk T, "Hydrogen-driven Power-to-X: State of the art and multicriteria evaluation of a study case," *Energy Conversion and Management,* vol. 266, 2022.

[24] Nicita A, Maggio G, Andaloro APF, Squadrito G, "Green hydrogen as feedstock: Financial analysis of a photovoltaic-powered electrolysis plant," *International Journal of Hydrogen Energy,* vol. 45, no. 20, pp. 11395-11408, 2020.

[25] Nemmour A, Ghenai C, Inayat A, "Parametric study and optimization of bio-hydrogen production using steam reforming of glycerol and biodiesel fuel mixtures," *Biomass Conversion and Biorefinery,* vol. 13, no. 10, pp. 8713-8725, 2023.

[26] Schemme S, Samsun RC, Peters R, Stolten D, "Power-to-fuel as a key to sustainable transport systems – An analysis of diesel fuels produced from CO2 and renewable electricity,," *Fuel,* vol. 205, pp. 198-221, 2017.

[27] "International Renewable Energy Agency (IRENA). Innovation outlook. Renewable Mini-Grids; 2021".

[28] Luo X, Wang J, Dooner M, Clarke J, "Overview of current development in electrical energy storage technologies and the application potential in power system operation," *Applied Energy,* vol. 137, pp. 511-536, 2015.

[29] Varone A, Ferrari M, "Power to liquid and power to gas: An option for the German Energiewende," *Renewable and Sustainable Energy Reviews,* vol. 45, pp. 207-218, 2015.

[30] Stančin H, Mikulčić H, Wang X, Duić N, "A review on alternative fuels in future energy system," *Renewable and Sustainable Energy Reviews,* vol. 128, 2020.

[31] Leonzio G, "Methanol Synthesis: Optimal Solution for a Better Efficiency of the Process," *Processes,* vol. 6, no. 3, p. 20, 2018.

[32] Olah GA, Alain G, Prakash GKS, "Chemical Recycling of Carbon Dioxide to Methanol and Dimethyl Ether: From Greenhouse Gas to Renewable, Environmentally Carbon Neutral Fuels and Synthetic Hydrocarbons," *The Journal of Organic Chemistry,* vol. 74, no. 2, pp. 487-498, 2009.

[33] Liu H, Wang Z, Long Y, Xiang S, Wang, Wagnon SW, "Methanol-gasoline Dual-fuel Spark Ignition (DFSI) combustion with dual-injection for engine particle number (PN) reduction and fuel economy improvement," *Energy,* vol. 89, pp. 1010-1017, 2015.

[34] Balki MK, Sayin C, "The effect of compression ratio on the performance, emissions and combustion of an SI (spark ignition) engine fueled with pure ethanol, methanol and unleaded gasoline," *Energy,* vol. 71, pp. 194-201, 2014.

[35] Shamsul NS, Kamarudin SK, Rahman NA, Kofli NT, "An overview on the production of bio-methanol as potential renewable energy," *Renewable and Sustainable Energy Reviews,* vol. 33, pp. 578-588, 2014.

[36] Svanberg M, Ellis J, Lundgren J, Landäl I, "Renewable methanol as a fuel for the shipping industry," *Renewable and Sustainable Energy Reviews,* vol. 94, pp. 1217-1228, 2018.

[37] Bozzano G, Manenti F, "Efficient methanol synthesis: Perspectives, technologies and optimization strategies," *Progress in Energy and Combustion Science,* vol. 56, pp. 71-105, 2016.

[38] Schorn F, Breuer JL, Samsun RC, Schnorbus T, Heuser B, Peters R, Stolten D, "Methanol as a renewable energy carrier: An assessment of production and transportation costs for selected global locations," *Advances in Applied Energy,* vol. 3, 2021.

[39] Tremel A, Wasserscheid P, Baldauf M, Hammer T, "Techno-economic analysis for the synthesis of liquid and gaseous fuels based on hydrogen production via electrolysis," *International Journal of Hydrogen Energy,* vol. 40, no. 35, pp. 11457-11464, 2015.

[40] Bos MJ, Kersten SRA, Brilman DWF, "Wind power to methanol: Renewable methanol production using electricity, electrolysis of water and CO2 air capture," *Applied Energy,* vol. 264, 2020.

[41] Son M, Woo Y, Kwak G, Lee YJ, Park MJ, "CFD modeling of a compact reactor for methanol synthesis: Maximizing productivity with increased thermal controllability," *International Journal of Heat and Mass Transfer,,* vol. 145, 2019.

[42] Sharifianjazi F, Esmaeilkhanian A, Ahmadi E, Moghaddam BR, Salahshour P, "Methane reforming in microchannels: Application to the methanol synthesis," *Chemical Engineering and Processing - Process Intensification,* vol. 185, 2023.

[43] Jamshidi S, Sedaghat MH, Amini A, Rahimpour MR, "CFD simulation and sensitivity analysis of an industrial packed bed methanol synthesis reactor," *Chemical Engineering and Processing - Process Intensification,* vol. 183, 2023.

[44] Arab S, Commenge JM, Portha JF, Falk L, "Methanol synthesis from CO2 and H2 in multi-tubular fixed-bed reactor and multi-tubular reactor filled with monoliths," *Chemical Engineering Research and Design,* vol. 92, no. 11, pp. 2598-2608, 2014.

[45] Petera J, Nowicki L, Ledakowicz S, "New numerical algorithm for solving multidimensional heterogeneous model of the fixed bed reactor," *Chemical Engineering Journal,* vol. 214, pp. 237-246, 2013.

[46] Jannike S, Hugo AJ, "Multicomponent mass diffusion in porous pellets: Effects of flux models on the pellet level and impacts on the reactor level. Application to methanol synthesis," *The Canadian Journal of Chemical Engineering,* vol. 91, no. 1, pp. 66-76, 2011.

[47] Karthik GM, Buwa, Vivek V, "A computational approach for the selection of optimal catalyst shape for solid-catalysed gas-phase reactions," *Reaction Chemistry and Engineering,* vol. 5, no. 1, pp. 163-182, 2020.

[48] Jurtz N, Kraume M, Wehinger GD, "Advances in fixed-bed reactor modeling using particle-resolved computational fluid dynamics (CFD)," *Reviews in Chemical Engineering,* vol. 35, no. 2, pp. 139-190, 2017.

[49] Mirvakili A, Bakhtyari A, Rahimpour MR, "A CFD modeling to investigate the impact of flow mal-distribution on the performance of industrial methanol synthesis reactor," *Applied Thermal Engineering,* vol. 128, pp. 64-78, 2018.

[50] Redondo B, Shah MT, Pareek VK, Utikar PR, Webley PA, Patel J, Lee WJ, Bhatelia T, "Intensified isothermal reactor for methanol synthesis," *Chemical Engineering and Processing - Process Intensification,* vol. 143, 2019.

[51] Izbassarov D, Nyári J, Tekgül B, Laurila E, Kallio T, Aarnio AS, Kaario O, Vuorinen V, "A numerical performance study of a fixed-bed reactor for methanol synthesis by CO2 hydrogenation," *International Journal of Hydrogen Energy,* vol. 46, no. 29, pp. 15635-15648, 2021.

[52] Feng H, Zhang Y, Liu D, Chen R, "Residence time characteristic of Taylor reacting flow in a microchannel reactor," *Chemical Engineering Science,* vol. 253, 2022.

[53] Khan A, Akram S, Kumar R, "Experimental study on enhancement of supersonic twin-jet mixing by vortex generators," *Aerospace Science and Technology,* vol. 96, 2020.

[54] Dogan M, Erzincan S, "Experimental investigation of thermal performance of novel type vortex generator in rectangular channel," *International Communications in Heat and Mass Transfer,* vol. 144, 2023.

[55] Izbassarov D, Nyári J, Laitinen A, Laari A, Aarnio AS, Vuorinen V, "A three-dimensional conjugate heat transfer model for methanol synthesis in a modular millireactor," *Chemical Engineering Science,* vol. 258, 2021.

[56] Poinsot T, Veynante D, "Conservation equations for reacting flows," in *Theoretical and numerical combustion*, Philadelfia, R.T. Edwards, Inc., 2001, pp. 1-24.

[57] Cloney CT, Ripley RC, Pegg MJ, Amyotte PR, "Laminar burning velocity and structure of coal dust flames using a unity Lewis number CFD model," *Combustion and Flame,* vol. 190, pp. 87-102, 2018.

[58] Sauer VM, Rankin DD, "Impinging nonpremixed coflow methane–air flames with unity Lewis number," *Proceedings of the Combustion Institute,* vol. 36, no. 1, pp. 1411-1419, 2017.

[59] Nicoli C, Haldenwang P, Suard S, "Analysis of pulsating spray flames propagating in lean two-phase mixtures with unity Lewis number," *Combustion and Flame,* vol. 143, no. 3, pp. 299-312, 2005.

[60] Kubota T, Hayakawa I, Mabuse H, Mori K, Ushikoshi K, Watanabe T, Saito M, "Kinetic study of methanol synthesis from carbon dioxide and hydrogen," *Applied Organometallic Chemistry,* vol. 15, no. 2, pp. 121-126, 2001.

[61] Kiss AA, Pragt JJ, Vos HJ, Bargeman G, de Groot MT, "Novel efficient process for methanol synthesis by CO2 hydrogenation," *Chemical Engineering Journal,* vol. 284, pp. 260-269, 2016.

[62] Lim HW, Park MJ, Kang SH, Chae HJ, Bae JW, Jun KW, "Modeling of the Kinetics for Methanol Synthesis using Cu/ZnO/Al2O3/ZrO2 Catalyst: Influence of Carbon Dioxide during Hydrogenation," *Industrial & Engineering Chemistry Research,* vol. 48, no. 23, pp. 10448-10455, 2009.

[63] An X, Zuo Y, Zhang Q, Wang J, "Methanol Synthesis from CO2 Hydrogenation with a Cu/Zn/Al/Zr Fibrous Catalyst," *Chinese Journal of Chemical Engineering,* vol. 17, no. 1, pp. 88-94, 2009.

[64] Jasak H, "OpenFOAM: Open source CFD in research and industry," *International Journal of Naval Architecture and Ocean Engineering,* vol. 1, no. 2, pp. 89-94, 2009.

[65] Greenshields C, Weller H, Notes on Computational Fluid Dynamics: General Principles, Reading, UK: CFD Direct Ltd, 2022.

[66] Pérez S, Molino ED, Barrio VL, "Modeling and Testing of a Milli-Structured Reactor for Carbon Dioxide Methanation," *International Journal of Chemical Reactor Engineering,* vol. 11, 2019.

[67] Salkuyeh YK, Ashrafi O, Mostafavi E, Navarri P, "CO2 utilization for methanol production; Part I: Process design and life cycle GHG assessment of different pathways," *Journal of CO2 Utilization,* vol. 50, 2021.

[68] Pope SB, Turbulent Flows, Cambridge: Cambridge University Press, 2000.

[69] Chen F, Liang J, Wang F, Guo X, Gao W, Kugue Y, He Y, Yang G, Reubroycharoen P, Vitidsant T, Tsubaki N, "Improved catalytic activity and stability of Cu/ZnO catalyst by boron oxide modification for low-temperature methanol synthesis," *Chemical Engineering Journal,* vol. 458, 2023.

[70] Griffith MD, Leontini J, Thompson MC, Hourigan K, "Vortex shedding and three-dimensional behaviour of flow past a cylinder confined in a channel," *Journal of Fluids and Structures,* vol. 27, no. 5-6, pp. 855-860, 2011.

[71] Yang X, Wang Z, Niu Y, Miao H, "The effect of two main vortexes generator on heat transfer enhancement in mini rectangular ducts of airborne thermoelectric conversion system," *International Journal of Heat and Mass Transfer,* vol. 213, 2023.

[72] Greenshields C, OpenFOAM v10 User Guide, London, UK: The OpenFOAM Foundation, 2022.

[73] Çelik MB, Özdalyan B, Alkan F, "The use of pure methanol as fuel at high compression ratio in a single cylinder gasoline engine," *Fuel,* vol. 90, no. 4, pp. 1591-1598, 2011.

[74] Zetian M, Volker S, "Taking a Shortcut: Direct Power-to-X Conversion," *Frontiers in Energy Research,* vol. 8, 2020.

Appendix

Computational cost

In all cases, the computational domain is decomposed according to the scotch algorithm to enable parallel running. Such a decomposition algorithm tends to minimize the number of processor boundaries between the decomposed domains. Fewer boundaries imply a reduction in the required communication between the processors and thus, faster computation [72]. Simulations are run in-parallel over 24 processors of the type Intel® Xeon® Gold 6248 @2.50GHz. In general, the used timesteps (Δt) are in the order of 10^{-7} s. Such small chemical timesteps are needed to accurately capture the involved chemistry and maintain a stable temperature field throughout the individual simulations.

First, the computational effort involved in the mesh convergence study is discussed (Table 27). As stated in previous sections, mesh convergence is investigated at Re=1100 and T_w=200°C. In line with anticipated outcomes, at finer meshes, the maximum allowable timestep (Δt_{max}) is smaller. In fact, coarsening the mesh from M128 to M64 allows for the usage of a Δt that is three times greater. Coupled with a remarkable reduction in the number of cells, using M64 instead of M128 makes the simulation about seven times faster. This leads to saving a computational power in excess of 995 CPU-hours.

Table 27. Computational cost of the mesh convergence study.

Mesh case	**Δt_{max} [s]**	**Total required time [h]**	**Required computational power [CPU hours]**
M32	6e-7	3.75	90
M64	3e-7	7.3	175.2
M128	1e-7	48.77	1170.48

Moreover, for the cases in which a recycling zone is present in the channel, Δt_{max}, the total required time and the computational power required to execute their corresponding simulations are displayed (Table 28). At each specific bulk flow velocity, the higher the temperature, the more expensive it is to perform the simulation. This is mainly attributed to the reaction kinetics. To elaborate further, at higher temperatures, the activity of the catalyst and thus, its performance is enhanced. Correspondingly, the rates of the chemical reactions governing the catalytic synthesis of methanol are higher. Therefore, in this context, maintaining stability of the various computed fields necessitates lowering the timesteps. Typically, the cell sizes of the computational grid and the flow velocity highly influence the size of Δt. These three parameters are related by the Courant number (Co), defined as $Co = \frac{U\Delta t}{\Delta x}$, where Δx is the computational grid spacing. Generally, the maximum Co of the simulation serves as a constraint or an indicator that permits the tuning of the simulation timestep. In reactive flows, the chemical kinetics, which are considerably influenced by the temperature, play an important role in dictating the size of Δt. In fact, Co hasn't exceeded 0.01 in any of the performed laminar flow simulations. Moreover, at a given temperature, a unique, predetermined value of Δt has been used at all four *Re*; Δt_{max} drops only when the temperature increases. This confirms that primarily, the temperature at the catalytic walls is the predominant factor setting Δt in these cases. Referring to the required simulation run-times calculated in section 3.3, as foreseen, the simulation involving the highest computational cost is for *Re*=100 and T_w=250°C.

Table 28. A summary of the maximum allowable timesteps (top), in addition to the total required time (middle) and computational power (bottom) needed to perform the laminar flow simulations featuring a flow recycling zone (Group (A)).

Δt_{max} [s] – Group (A) simulations				
	***Re*=100**	***Re*=200**	***Re*=550**	***Re*=1100**
T_w=200°C	3.5e-7	3.5e-7	3.5e-7	3e-7
T_w=210°C	3e-7	3e-7	3e-7	3e-7
T_w=220°C	2.5e-7	2.5e-7	2.5e-7	2.5e-7
T_w=230°C	2e-7	2e-7	2e-7	2e-7
T_w=240°C	1.5e-7	1.5e-7	1.5e-7	1.5e-7
T_w=250°C	1e-7	1e-7	1e-7	1e-7

Total required time [h] – Group (A) simulations				
	***Re*=100**	***Re*=200**	***Re*=550**	***Re*=1100**
T_w=200°C	71.23	35.92	12.639	7.3
T_w=210°C	82.35	40.65	14.8	7.19
T_w=220°C	97	48	17.1	8.37
T_w=230°C	118.54	57.76	20.45	10.22
T_w=240°C	150.42	74.27	26.791	13.3
T_w=250°C	213.129	103.49	37.28	18.84

Computational power [CPU-hours] – Group (A) simulations				
	***Re*=100**	***Re*=200**	***Re*=550**	***Re*=1100**
T_w=200°C	1709.5	862.08	303.34	175.2
T_w=210°C	1976.4	975.6	355.2	172.56
T_w=220°C	2328	1152	410.4	200.88
T_w=230°C	2845	1386.2	490.8	245.28
T_w=240°C	3610.1	1782.5	642.98	319.2
T_w=250°C	5115.1	2483.8	894.72	452.16

Extending the reacting zone to the inlet of the reactor, the corresponding simulations are performed at isothermal conditions of T_w=210°C. In this scenario, the simulation characterized with the smallest timestep pertains to *Re*=1100. Furthermore, at each *Re*, comparing the outcome to the correspondent case featuring flow recycling, a lower Δt_{max} is always observed. This indicates that group (B) simulations are more costly from a computational standpoint. In addition to the fact that reactions occur along the entire streamwise length of the channel, *Re* has had a notable influence on Δt in these situations. The simulation featuring the greatest computational burden is at *Re*=100 due to the relatively extended simulation run-time.

Table 29. Computational cost of the laminar flow simulations in which the catalyst coating is applied along the entire length of the reactor (Group (B))

Simulation case	**Δt_{max} [s]**	**Total required time [h]**	**Required computational power [CPU hours]**
***Re*=100**	2.5e-7	94	2256
***Re*=200**	2e-7	56.18	1348.32
***Re*=550**	1.5e-7	26	624
***Re*=1100**	1e-7	18.64	447.36

Finally, after the introduction of VGs into the catalytic reactor segment, all simulations are again conducted at T_w=210°C. These simulations fall into the category of unsteady flows. As a rule of thumb, the maximum *Co* in unsteady flow simulations is typically constrained to 0.1. This constraint has been reached in the simulations featuring the two highest *Re*, *i.e.* *Re*=550 and *Re*=1100, due to the presence of very small cells in proximity to the obstacles. Consequently, their respective timestep values have been constrained, as evident in Table 30. As a result, among all performed simulations at *Re*=550 and *Re*=1100, the ones belonging to group (C) prove to be the most demanding in terms of computational effort. Concerning *Re*=100 and *Re*=200, the same timesteps as these employed in their equivalent laminar cases have been set.

Table 30. The involved computational cost in the simulations featuring vortex generators (Group (C)). (Rect) refers to the rectangular obstacle, while (Sq) refers to the three squared obstacles.

Simulation case	**Δt_{max} [s]**	**Total required time [h]**	**Required computational power [CPU hours]**
***Re*=100 (Rect)**	2.5e-7	189.83	4555.92
***Re*=200 (Rect)**	2e-7	110.52	2652.48
***Re*=550 (Rect)**	1.3e-7	62.67	1504.08
***Re*=550 (Sq)**	1.3e-7	68.32	1639.68
***Re*=1100 (Rect)**	6.5e-8	57.45	1378.8